



---

# The interaction of graphene quantum dots with human cells

---

INAUGURAL-DISSERTATION

ZUR ERLANGUNG DES DOKTORGRADES DER  
MATHEMATISCH-NATURWISSENSCHAFTLICHEN FAKULTÄT DER  
HEINRICH-HEINE-UNIVERSITÄT DÜSSELDORF

VORGELEGT VON

STEFAN FASBENDER

GEBOREN AM 12. DEZEMBER 1987 IN KREFELD

Düsseldorf, März 2020

aus dem Institut für Experimentelle Physik der kondensierten Materie  
der Heinrich-Heine-Universität Düsseldorf

Gedruckt mit der Genehmigung der  
Mathematisch-Naturwissenschaftlichen Fakultät der  
Heinrich-Heine-Universität Düsseldorf

Berichterstatter

1. Prof. Dr. Thomas HEINZEL
2. Prof. Dr. Rainer HAAS

Tag der mündlichen Prüfung: 25. August 2020

# Abstract

Graphene quantum dots (GQDs) consist of one or a few layers of graphene. They are used in biomedical research not only for drug delivery applications, but also for long term and deep tissue imaging, cancer diagnostics and intracellular sensing. All of these applications require profound knowledge about the effect of GQDs on the cells. This thesis deals with the uptake dynamics of the GQDs into different cells, the intracellular distribution of the GQDs and the transcriptomic response of the cells to GQDs.

First, we established a reliable and reproducible preparation process based on the pyrolysis of citric acid. The as prepared GQDs were characterized by fluorescence spectroscopy, ultraviolet-visible spectrophotometry, X-ray photoelectron spectroscopy, high resolution transmission electron microscopy and Raman spectroscopy.

Then we studied the uptake dynamics of GQDs into primary human blood cells for a period of 36 hours. We observed for all cell types studied an approximately linear time- and concentration-dependent uptake with a significantly greater uptake into monocytes and granulocytes in comparison to lymphocytes. The effect of the GQDs on the viability of the cells was rather low with a measured viability of 90 % after an exposure time of 36 hours.

The next set of experiments concentrated on the intracellular distribution and uptake of GQDs into different breast cancer models. A three times higher uptake into estrogen receptor positive, progesterone receptor positive, HER2 negative MCF-7 cells was observed compared to MDA-MB-231 cells as an example for triple negative breast cancer and MCF-10A cells as a model for non-tumorigenic mammary epithelial cells. It was demonstrated for all three cell types that the GQDs accumulate near the nucleus inside the endolysosomal system. Furthermore, the penetration of GQDs into murine precision-cut mammary tumor slices was studied, where a constant uptake into the depth of the tissue and no increase of apoptotic or necrotic cells was found.

Finally, we examined the effect of GQDs on the transcriptome of primary human CD34<sup>+</sup> hematopoietic stem cells. Only one of the 20 800 recorded gene expressions, namely the selenoprotein W, 1, was changed by the GQDs in direct comparison to

CD34<sup>+</sup> hematopoietic stem cells cultivated without GQDs. Only a meta analysis revealed that the expression of 1171 genes was weakly affected, taking into account the more prominent changes just by the cell culture. Eight corresponding, weakly affected signaling pathways were identified, which include, but are not limited to, the triggering of apoptosis.



# Eidesstattliche Versicherung

Ich versichere an Eides Statt, dass die Dissertation von mir selbständig und ohne unzulässige fremde Hilfe unter Beachtung der „Grundsätze zur Sicherung guter wissenschaftlicher Praxis an der Heinrich-Heine-Universität Düsseldorf“ erstellt worden ist.

---

Düsseldorf, den 11. März 2020



# Contents

<b>Introduction</b>	<b>1</b>
<b>1 Fundamentals</b>	<b>4</b>
1.1 Graphene . . . . .	4
1.2 Graphene quantum dots . . . . .	7
1.2.1 Properties . . . . .	7
1.2.2 Biomedical applications . . . . .	11
1.3 Hematopoiesis . . . . .	14
1.4 <i>In vitro</i> and <i>ex vivo</i> breast cancer models . . . . .	17
<b>2 Experimental techniques</b>	<b>19</b>
2.1 Preparation of graphene quantum dots . . . . .	19
2.2 Analysis of graphene quantum dots . . . . .	23
2.2.1 Fluorescence spectroscopy and ultraviolet-visible spectropho- tometry . . . . .	23
2.2.2 X-ray photoelectron spectroscopy . . . . .	24
2.2.3 Transmission electron microscopy . . . . .	25
2.2.4 Raman spectroscopy . . . . .	27
2.3 Analysis of the cells exposed to graphene quantum dots . . . . .	29
2.3.1 Flow cytometry . . . . .	29
2.3.2 Confocal fluorescence microscopy . . . . .	30
2.3.3 MTT and XTT assay . . . . .	31
2.3.4 Gene expression profiling based on microarray technique . . . . .	32
<b>3 Publications</b>	<b>34</b>
<b>4 Conclusions and Outlook</b>	<b>94</b>
<b>Bibliography</b>	<b>96</b>
<b>Danksagung</b>	<b>106</b>



The following introduction is strongly oriented on the introductions in references [1–3] that form the basis of this thesis.

# Introduction

Nanomaterials are already part of our daily life, often without our knowledge. They are not only ingredients in consumer products like clothes [4], food [5] and cosmetics [6] but also they are used as drug delivery systems and extend the life of patients with acute myeloid leukemia [7]. Since its discovery in 2004 [8] and the corresponding award of the Nobel Prize in Physics 2010, graphene has gained much attention as a novel two-dimensional nanomaterial. For example, the European Union Graphene Flagship project is together with the Human Brain Project one of the largest collaborative research projects that have ever been set up in Europe and spends 1 billion euro to generate technological breakthroughs around graphene and related materials [9]. First graphene containing consumer products are already available in the packaging and sports industry [10,11] due to its superior mechanical [12,13], chemical [14] and electronic [15,16] properties. Graphene quantum dots (GQDs) consist of one or a few layers of graphene with a size of less than 100 nm [17]. Due to quantum confinement and edge effects they emit strong fluorescence [18]. While most reported GQDs have a circular or elliptical shape with a diameter of a few nm [19], there are also a few reports of triangular [20], hexagonal [21] and other polygonal [22] shapes. They are used in research related to organic photovoltaic devices, catalysis, sensors and biomedicine [23]. Especially the field of biomedicine offers interesting opportunities regarding drug delivery [24,25], cancer diagnostics [26], intracellular sensing [27] and long term and deep tissue imaging [28,29] as GQDs enter various human cell types *in vitro* without significant effects on the viability of the cells [30–33]. As far as the exposure of human cells *in vitro* or *in vivo* to GQDs is concerned, their possible side effects on the functionality of these cells remain a question of ongoing research. For instance, *in vivo* studies show that high doses of GQDs disrupt the progression of embryonic development in zebrafish [34]. In mice, intravenously injected larger graphene nanosheets induced Th2 inflammatory responses [35]. *In vitro* studies using fibroblast cell lines show increased expression of p53, Rad51 and OGG1 proteins, indicating DNA damage caused by GQDs of 40 nm diameter [36]. The toxicity of graphene based nanomaterials appears to be mainly related to particle

size, surface functional groups, oxygen content, surface charges and impurities, while the formation of reactive oxygen species (ROS) seems to be the most common underlying mechanism [37].

However, these toxicity studies reported hitherto are no more than a glimpse of the overall, possibly quite complex, responses of the cells to the incubation with GQDs while all suggested biomedical applications require detailed knowledge about the interaction of living cells and GQDs. In this thesis we study the effects of GQDs on the transcriptome of primary human hematopoietic stem cells as well as the uptake dynamics into various human benign and malign cells in detail. It is organized as follows.

Chapter 1 discusses the fundamentals of GQDs and the used cell culture model systems. First, the physical properties of graphene and GQDs are shown before a review of the present literature regarding biomedical applications of GQDs is given. Then the basics of hematopoiesis, including human leukocytes and CD34<sup>+</sup> hematopoietic stem cells are presented. Finally, different *in vitro* and *ex vivo* breast cancer models are introduced.

Chapter 2 deals with the experimental techniques used in this thesis. First, the established process for the preparation of GQDs based on the pyrolysis of citric acid is presented in chapter 2.1. The as prepared GQDs were characterized by fluorescence spectroscopy, ultraviolet-visible spectrophotometry, X-ray photoelectron spectroscopy, high resolution transmission electron microscopy and Raman spectroscopy. These methods are discussed in chapter 2.2. To analyse the cells we used flow cytometry, confocal fluorescence microscopy, XTT and MTT assay and gene expression analysis based on microarray technique, which are presented in chapter 2.3.

Chapter 3 consists of the three publications resulting from this work. The first paper studies in detail the uptake dynamics of GQDs into primary human leukocytes as well as hematopoietic stem cells. Concentration dependent uptake rates for monocytes, granulocytes, CD19<sup>+</sup> B cells, CD56<sup>+</sup> natural killer cells, CD4<sup>+</sup> T cells, CD8<sup>+</sup> T cells and CD34<sup>+</sup> hematopoietic stem cells are measured and the number of incorporated GQDs after an incubation time of 36 hours is estimated. The second paper concentrates on the intracellular distribution and uptake of GQDs into different breast cancer models. The cell line MCF-7 serves as an example for estrogen receptor positive, progesterone receptor positive, HER2 negative breast cancer, the cell line MDA-MB-231 as a model for triple negative breast cancer and

the cell line MCF-10A as an example for non-tumorigenic mammary epithelial cells. They were used *in vitro*, while murine precision-cut mammary tumor slices were studied in a closer to reality *ex vivo* approach. The third paper reports the cellular gene expression and the attributed signaling pathways after incubation of primary human CD34<sup>+</sup> hematopoietic stem cells with a high concentration 500  $\mu\text{g ml}^{-1}$  of GQDs for an exposure time of 36 hours. These cells are particularly susceptible to any kind of cytotoxic effects such as conventional chemotherapy or radiation. They are composed of the most primitive hematopoietic stem cells as well as the more committed progenitor subset, which is responsible for the lifelong production of mature blood cells.

The thesis ends with a conclusion of the main findings and an outlook towards potential future research in chapter 4.

# 1 Fundamentals

This chapter discusses the fundamentals of GQDs and the used cell culture model systems. First the physical properties of graphene and GQDs are shown before a review of the present literature regarding biomedical applications of GQDs is given. Then the basics of hematopoiesis, including human leukocytes and CD34<sup>+</sup> hematopoietic stem cells are presented. Finally, the cell lines MCF-7 as an example for estrogen receptor positive, progesterone receptor positive, HER2 negative breast cancer, MDA-MB-231 as a model for triple negative breast cancer and MCF-10A as an example for non-tumorigenic mammary epithelial cells as well as the *ex vivo* model of MMTV-PyMT precision-cut mammary tumor slices are introduced.

## 1.1 Graphene

Graphene consists of sp<sub>2</sub>-hybridized carbon atoms organized in a two-dimensional hexagonal lattice with two basis atoms, which means it is a single layer of graphite. Due to the Mermin-Wagner-theorem [38] it was thought to be thermodynamically unstable as an infinitely extended 2d-material. Therefore its discovery in 2004 by Novoselov and Geim [8] attracted a lot of attention and was awarded the Nobel Price in Physics in 2010 accordingly.

As all carbon atoms are sp<sub>2</sub>-hybridized, every atom has three  $\sigma$ -bonds with a bond length of 142 pm and a bond angle of 120°. The remaining fourth valence electron out of the p<sub>z</sub> orbital forms a binding  $\pi$ -bond and an antibinding  $\pi^*$ -bond directed out of plane in z-direction. The  $\pi$ -bonds of the carbon atoms are hybridized together and form the  $\pi$ -band and the  $\pi^*$ -band, which are responsible for the outstanding electronic properties of graphene [39]. In general, the bonding structure of graphene can be illustrated as a ring consisting of 6 carbon atoms that has two double bonds, which are not localized. An experimental observation of the graphene honeycomb lattice is shown in Figure 1.1.

The band structure of graphene is already known since 1947 when P.R. Wallace calculated the band structure of a single graphite layer [40]. For that purpose he regarded the honeycomb lattice as two interleaving triangular lattices A and B



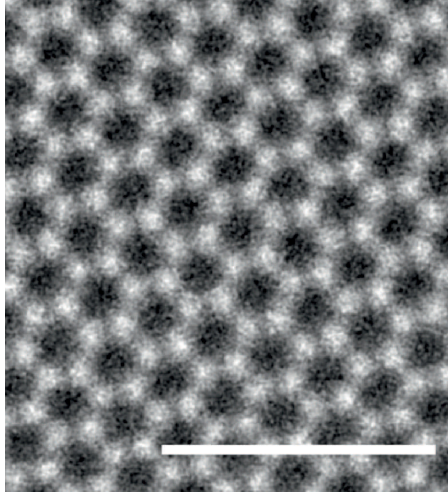


**Figure 1.1:** Scanning transmission electron microscopy image of graphene (taken from [41] under Creative Commons Attribution 4.0 International license). Scale bar 1 nm

(see Figure 1.2 (a)) and used a tight-binding approximation. The tight-binding Hamiltonian can be written as:

$$\mathcal{H}_{\vec{k}} = \begin{pmatrix} \epsilon_A & te^{i\vec{k}\cdot\vec{a}_1} + te^{i\vec{k}\cdot\vec{a}_2} + te^{i\vec{k}\cdot\vec{a}_3} \\ c.c. & \epsilon_B \end{pmatrix} \quad (1.1)$$

with the vectors to the three nearest neighbor atoms  $\vec{a}_1 = a(1, 0)$ ,  $\vec{a}_2 = a(-\frac{1}{2}, \sin[\frac{\pi}{3}])$  and  $\vec{a}_3 = a(-\frac{1}{2}, -\sin[\frac{\pi}{3}])$ , the on-site energies of the carbon atoms on sites A and B  $\epsilon_A = \epsilon_B = 0$ , the nearest neighbor hopping element between A and B sites  $t = 2.7\text{eV}$  and c.c. the complex conjugate of the off-diagonal matrix element [39]. The corresponding eigenvalues are shown in Figure 1.2 (b) as a function of  $\vec{k} = (k_x, k_y)$ .

Near the Dirac points K and K' in Figure 1.2(b) the energy dispersion becomes linear and reads

$$E_{\pm}(k) \approx \pm \hbar v_F |k - K|, \quad (1.2)$$

which can be described by the Dirac equation for massless fermions. This means the effective mass of charge carriers in this region is zero. The corresponding Dirac-Hamiltonian is:

$$\mathcal{H}_K = \hbar v_F \begin{pmatrix} 0 & k_x - ik_y \\ k_x + ik_y & 0 \end{pmatrix} = \hbar v_F \vec{\sigma} \cdot \vec{k} \quad (1.3)$$

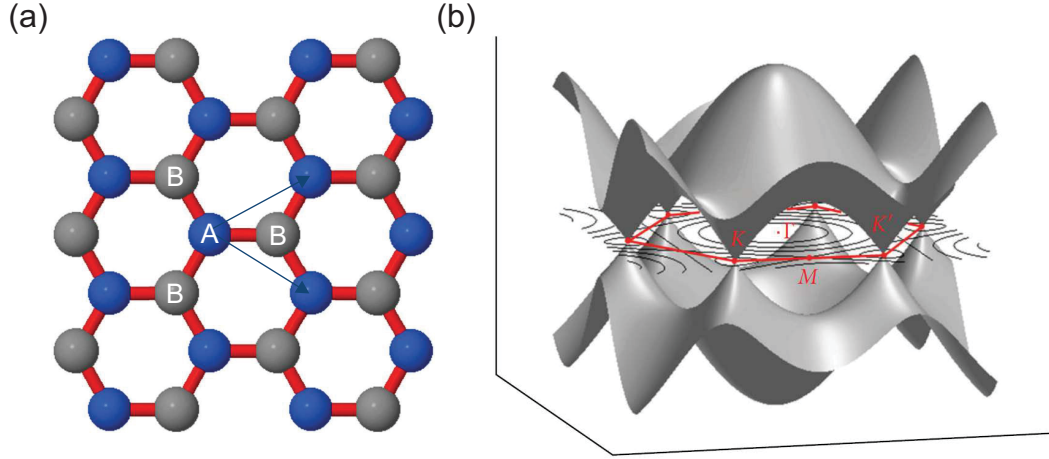


**Figure 1.2:** (a) Triangular sublattices of graphene. Each atom A has 3 nearest neighbor atoms B and vice-versa. (b) First Brillouin zone and band structure of graphene. The vertical axis is energy, while the horizontal axes are momentum space on the graphene lattice ((a) and (b) taken from [39] under Creative Commons Attribution 3.0 Unported license).

with the 2D vector of the Pauli matrices  $\vec{\sigma} = (\sigma_x, \sigma_y)$ , the wavevector  $\vec{k}$  and the Fermi velocity  $v_F \approx 10^6$  m/s. This implies that the band gap vanishes in the K-points and the charge carriers in proximity to those behave like relativistic fermions with an effective speed of light that is the Fermi velocity. The aforementioned leads to outstanding electronic properties like an ultrahigh electron mobility of  $2 \cdot 10^5 \frac{\text{cm}^2}{\text{Vs}}$  [15], the appearance of Klein-tunneling [42] and an anomalous quantum hall effect [43].

## 1.2 Graphene quantum dots

Graphene quantum dots (GQDs) are graphene flakes with functional groups at the edges, that are small enough to provide confinement in all directions to electrons that occupy the  $\pi$ -orbital. Typically, they consist of one or a few layers of graphene with lateral dimensions of just a few nanometers, with some larger GQDs also reported [19]. In the following the most important physical properties and biomedical applications will be introduced.

### 1.2.1 Properties

#### Size dependence of the energy gap

Although infinite graphene has no band gap as pointed out above, GQDs do have an energy gap due to confinement effects. The size dependence of this energy gap is well known for semiconductor quantum dots. For the calculation of the energy gap of semiconductor quantum dots a hard sphere potential is assumed and the resulting Schrödinger equation leads to the following energy eigenvalue in the ground state:

$$E_{1,0} = \frac{\pi^2 \hbar^2}{2m^* r_0^2} \quad (1.4)$$

which gives an energy gap of:

$$\Delta_{QD} = \Delta_{SC} + \frac{\pi^2 \hbar^2}{m^* r_0^2} \quad (1.5)$$

with the effective mass  $m^*$ , the radius of the sphere  $r_0$  and the bandgap of the bulk semiconductor  $\Delta_{SC}$ . This means, the energy gap of a semiconductor quantum dot is larger than the band gap of the bulk semiconductor and the energy gap of the semiconductor quantum dot decreases with increasing size of the quantum dot. As the charge carriers in graphene behave like massless relativistic fermions the Dirac equation must be used instead of the Schrödinger equation for their description. Schnez et al. as well as Tamandani et al. present an analytical approach [44, 45] to that problem, however a complete analytical solution to calculate the band gap for small and realistic GQDs does not exist so far. Instead, numerical simulations based on the tight binding model [46], the Dirac-Weyl model [47] or the density functional theory [48] are applied.

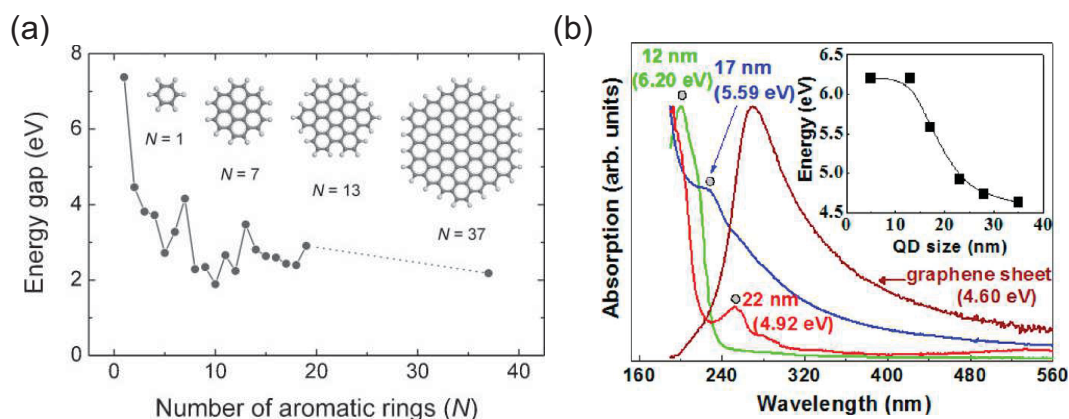


**Figure 1.3:** (a) Density functional calculations of the energy gap of the  $\pi - \pi^*$ -transition as a function of the number of aromatic rings. Reprinted with permission from [49]. ©(2010) WILEY-VCH (b) Absorbance spectra for three typical GQDs with sizes of 12, 17 and 22 nm and a graphene sheet. The inset shows the energy of the absorbance peak as a function of GQD size. Reprinted with permission from [22]. ©(2012) American Chemical Society.

Although no analytical expression for the energy gap exists there is clear theoretical [49, 50] as well as experimental [22, 51] evidence that the energy gap of GQDs decreases with increasing size, which is similar to semiconductor quantum dots. One example for density functional theory calculations regarding the energy gap of the  $\pi - \pi^*$ -transition is shown in Figure 1.3 (a) and experimental observations using optical absorbance measurements of the  $\pi - \pi^*$ -transition are presented in Figure 1.3 (b).

### Edge states

Graphene and also GQDs may occur with two different edge structures, so called armchair and zigzag-edges as illustrated in Figure 1.4 (a). As the wave function of the electrons is much more localized in GQDs with zigzag edges compared to GQDs with armchair edges [47] (see Figure 1.4 (b)), the edge type has a pronounced influence on the energy gap. In general, the energy gap of armchair GQDs is significantly higher than the energy gap of similar sized zigzag GQDs [50].

### Functional groups

Realistic GQDs usually contain functional groups like hydroxyl, carbonyl, carboxyl, hydrazide and amine groups, which leads to an excellent water solubility [29]. The composition of this groups depends on the preparation process and has a

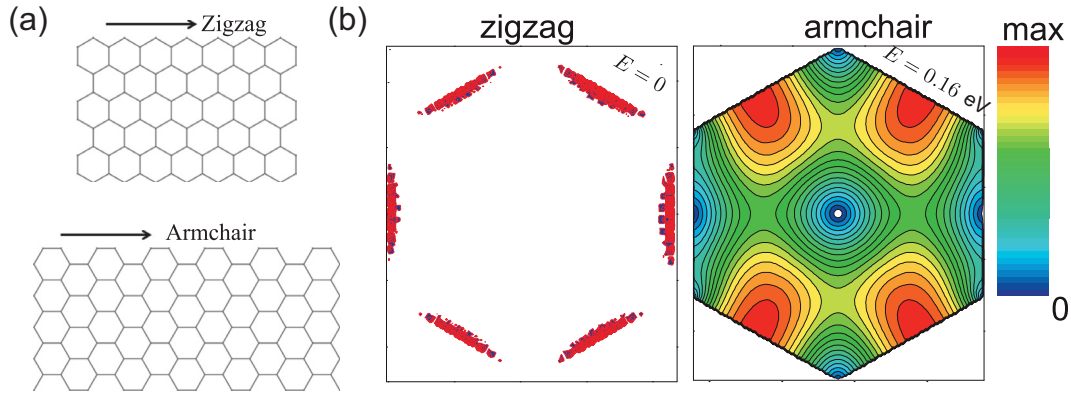


**Figure 1.4:** (a) Zigzag and armchair edge structures of graphene (taken from [52] under Creative Commons Attribution 4.0 International license). (b) Electron probability densities for hexagonal zigzag (left) and armchair (right) GQDs. Reprinted with permission from [47]. ©(2011) APS

pronounced influence on the energy gap. Density functional theory calculations show that orbital hybridization of the GQD carbon core and the functional group reduces the energy gap, while on the other hand charge transfer from the GQD to the functional group enlarges the energy gap [53], which may also lead to pH-sensitivity of the optical properties [54]. The effect of orbital hybridization outstrips the charge transfer effect, therefore functional groups lead to a lower energy gap as compared to hydrogen passivated GQDs as shown in Figure 1.5 (a). Figure 1.5 (b) illustrates that the addition of  $\text{NH}_2$  groups leads to a decrease of the energy gap but the effect saturates by adding the 6th  $\text{NH}_2$  group.

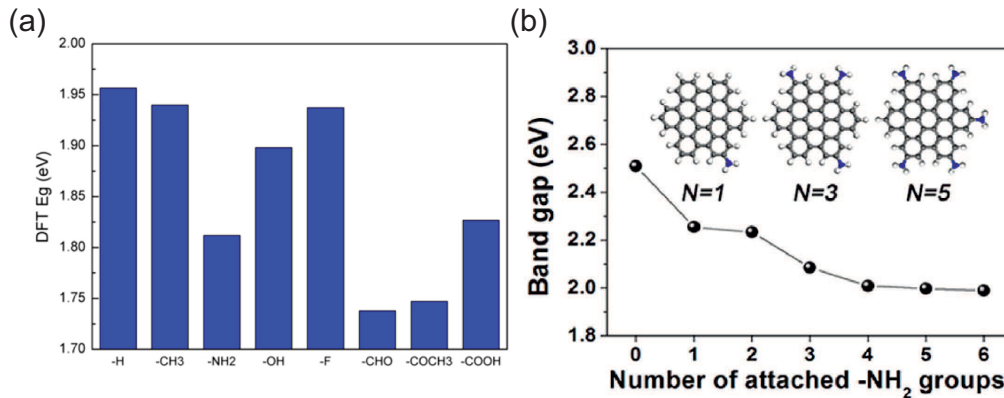


**Figure 1.5:** (a) Density functional theory calculations of the energy gap of edge functionalized GQDs. Reprinted with permission from [53]. ©(2015) American Chemical Society. (b) Energy gap change as a function of the number of attached  $\text{NH}_2$  groups. Reprinted with permission from [54]. ©(2012) American Chemical Society.

## Optical properties

The combination of size, edge states and functional groups may lead to many kinds of different GQDs with varying optical properties [55]. The GQDs used in this work are a typical example for very small GQDs (average diameter of 3.3 nm) which contain equal amounts of nitrogen and oxygen (20 % each). Figure 1.6 shows the fluorescence spectra and the corresponding absorbance spectrum of the used GQDs.

The GQDs show a pronounced absorption peak around 225 nm that is usually attributed to the  $\pi - \pi^*$  transition of C=C [27] while the peak around 350 nm belongs to the  $n - \pi^*$  transition of C=O and the long but weak shoulder in the range of 400 to 500 nm to the  $n - \pi^*$  transition of the N state [56]. The fluorescence spectrum reveals that no emission is related to the  $\pi - \pi^*$  transition, excitation at the  $n - \pi^*$  transition of C=O leads to strong fluorescence in the blue around 450 nm and excitation at the  $n - \pi^*$  transition of the N state leads to weak fluorescence in the yellow. Interestingly, the fluorescence emission peaks are broad and non-gaussian with a larger shoulder to lower energies. This might at least in parts be explained by the giant red edge effect, that occurs in polar solvents when the solvent relaxation is on the same time scale as the emitting relaxation to the ground state [57].

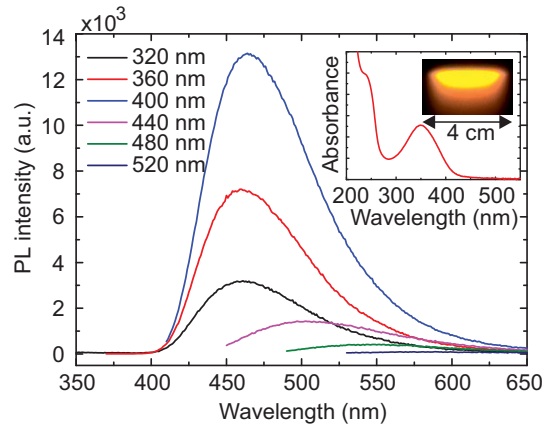


**Figure 1.6:** Fluorescence spectra as a function of the excitation wavelength of the GQDs used in this work. The corresponding absorbance spectrum including an image of the GQD solution under excitation with blue light is shown in the inset. Taken from [3] under Creative Commons Attribution 4.0 International license).



### 1.2.2 Biomedical applications

#### Intracellular sensing

As pointed out above, functional groups and the related  $n - \pi^*$  transition have a pronounced influence on the optical properties of GQDs. Wu et al. showed that the fluorescence intensity of N-doped GQDs depends on the zeta potential. Thus the fluorescence intensity changes with the pH of the environment due to the protonation of the functional groups under acidic conditions [27]. This might be used for non-invasive measurements of the intracellular pH change as shown in Figure 1.7. Similar concepts are also used to monitor intracellular cytokines [58] or glutathione [59].

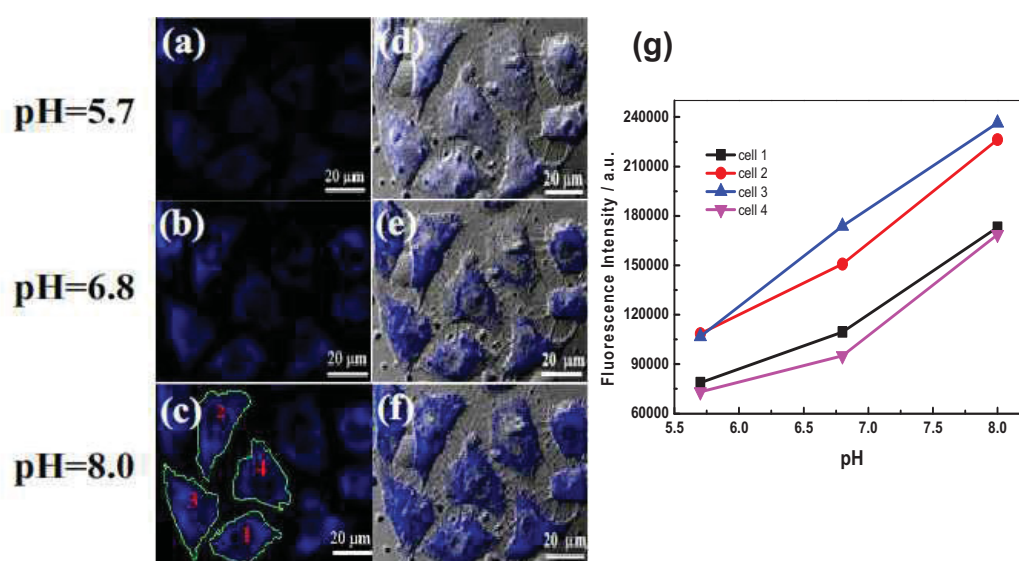


**Figure 1.7:** Confocal fluorescence images of Hep-2 cells after incubation with GQDs at pH (a) 5.7, (b) 6.8, (c) 8.0 and the corresponding overlay with the bright field images at pH (d) 5.7, (e) 6.8 and (f) 8.0. (g) Measurement of the fluorescence intensity of the four cells marked in (c) at different pH. Reprinted with permission from [27]. ©(2014) The Royal Society of Chemistry.

#### Drug delivery

Graphene, graphene quantum dots as well as carbon quantum dots may easily be loaded with the cancer drug doxorubicin by electrostatic attraction as well as  $\pi$ - $\pi$  stacking between the aromatic rings in the carbon core and the conjugated rings of the doxorubicin molecules [60]. While this stacking is relatively stable at pH = 7.4 most of the doxorubicin is released over 24 h at pH = 5.0, where the

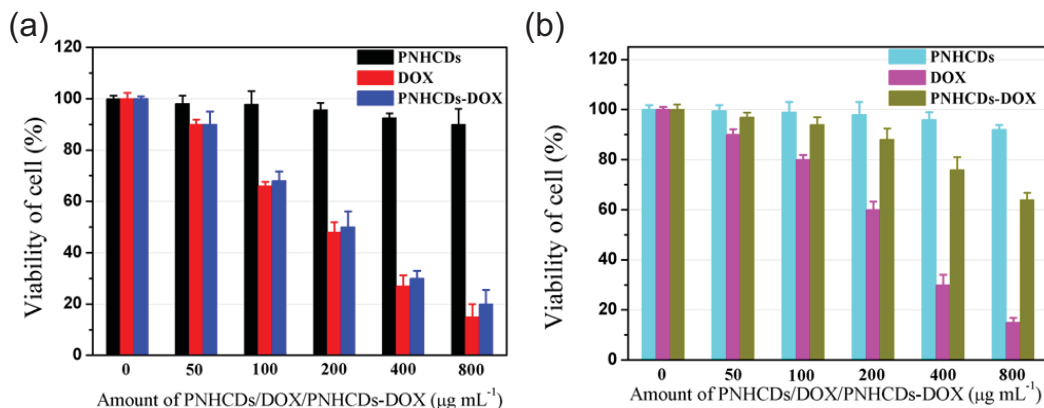


**Figure 1.8:** Cell viability of (a) HepG2 liver cancer cells and (b) noncancerous L-02 fetal hepatocytes treated with carbon dots (PNHCDs), doxorubicin (DOX) and doxorubicin loaded carbon dots (PNHCDs-DOX). Reprinted with permission from [25]. ©(2015) American Chemical Society.

water solubility of doxorubicin is significantly increased and the electric attraction between carrier and drug is decreased [25]. This pH dependent behavior is very important as the microenvironment of tumors often is more acidic compared to healthy tissue [61]. Gong et al. used these properties to build a carbon quantum dot based drug delivery system loaded with doxorubicin. This formulation inhibits growth of the liver cancer cell line HepG2 at least as efficient as doxorubicin alone but protects noncancerous L-02 cells, which is a human fetal hepatocyte line, as shown in Figure 1.8. Furthermore, *in vivo* studies in mice demonstrated similar tumor growth inhibition compared to doxorubicin alone but lower side effects like weight loss [25]. Similar concepts are also applied for more tumor targeted, GQD based doxorubicin delivery using hyaluronic acid [62] or biotin [63] as well as delivery of cisplatin with enhanced anticancer activity [24].

### Long term and deep tissue imaging

Long term and deep tissue imaging of living organisms has three challenges: Toxicity, photostability and the absorption of the emitted light as well as absorption of the light used for excitation. GQDs seem to be relatively non-toxic and possess stable fluorescence properties [17]. However, the excitation wavelength of GQDs is usually in the range of 350 nm to 500 nm, which is too far away from the optical window between 650 nm and 900 nm where the absorption of biological tissue is low enough for deep tissue imaging [64]. Liu et al. tried to overcome this problem by using two photon fluorescence imaging, which means a higher excitation wavelength can be used but therefore two photons at the same time are needed for the excitation



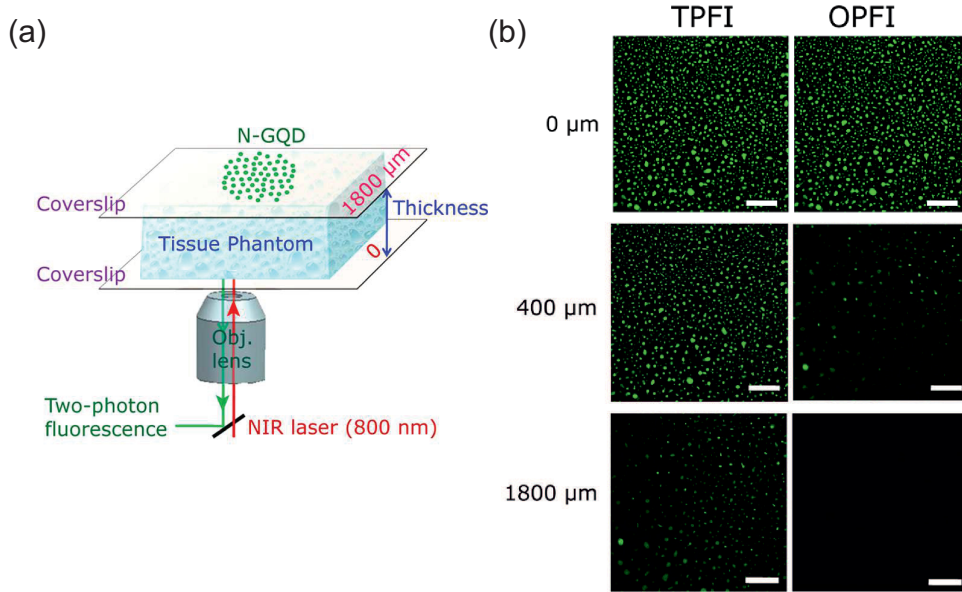


**Figure 1.9:** (a) Experimental setup of the two photon fluorescence imaging experiment. (b) Penetration depth for two photon fluorescence imaging (TPFI, left) and one photon fluorescence imaging (OPFI, right) with GQDs. Scale bars 100  $\mu\text{m}$ . Adapted with permission from [28]. ©(2013) American Chemical Society.

of the fluorescent state. This of course has a much lower absorption cross-section, nevertheless Liu et al. could demonstrate that the remaining fluorescence is high enough to be detected in a depth of up to 1800  $\mu\text{m}$  using a tissue phantom. This depth could not be reached with single photon fluorescence imaging as shown in Figure 1.9 [28]. The same concept was also used by Qian et al. for *in vivo* imaging of blood vessels in mice [65].

## 1.3 Hematopoiesis

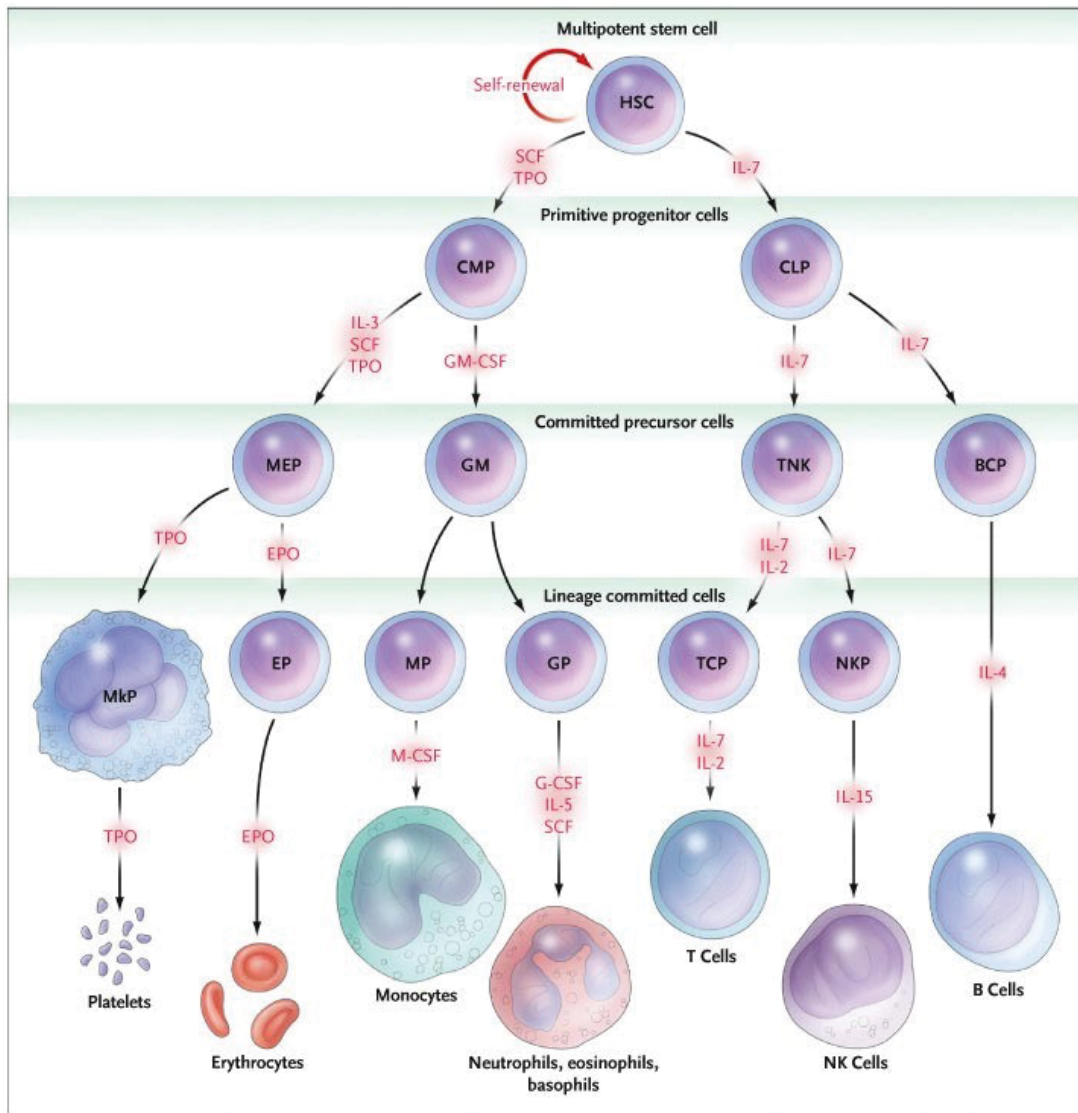
Most parts of this work use primary human blood cells at different development stages as object of study because all *in vivo* applications will expose various blood cells to GQDs. Therefore the process of hematopoiesis, which is the formation of the cellular blood components derived from hematopoietic stem cells, is described in the following.

Figure 1.10 illustrates the development from a hematopoietic stem cell (HSC) to differentiated blood cells: A HSC can either undergo self-renewal or differentiation into a common lymphoid progenitor cell (CLP) or a common myeloid progenitor cell (CMP). CLPs then give rise to precursor cells that are committed to T cells and natural killer cells (TNKs) as well as precursor cells committed to B cells (BCPs), while CMPs give develop into precursor cells that are committed to megakaryocytes and erythroid cells (MEPs) as well as precursor cells committed to granulocytes and macrophages (GMs). These cells give rise to lineage committed progenitors that ultimately form platelets, erythrocytes, monocytes, granulocytes (neutrophils, eosinophils and basophils), T cells, NK cells and B cells [66].

The cells of the human immune system are called leukocytes and are comprised of granulocytes and monocytes, which come from the myeloid lineage, and B cells, T cells and NK cells, which belong to the lymphoid lineage and are called lymphocytes. The most important properties of these cells will be described here briefly, as these will help to understand the uptake of GQDs into the cells.

**Granulocytes** account for up to 70 % of the leukocytes and are characterized by the presence of granules in the cytoplasm [67]. They are also called polymorphonuclear leukocytes due to the varying shape of the nucleus and have a diameter of 10  $\mu\text{m}$  to 15  $\mu\text{m}$  [68]. Granulocytes are part of the innate immune system and are able to attack microorganisms by phagocytosis (ingestion), generation of neutrophil extracellular traps as well as release of toxic granule proteins [69]. According to their staining characteristics granulocytes are further classified into basophils, eosinophils and neutrophils.

**Monocytes** are the largest leukocytes with a diameter of 15  $\mu\text{m}$  to 30  $\mu\text{m}$  [70]. They are not only part of the innate immune system and destroy foreign structures by phagocytosis but also activate the adaptive immune system by antigen presentation. After circulation of 1 - 3 days monocytes infiltrate into tissue and differentiate into macrophages or dendritic cells [71]. Upon the expression of the cell surface



**Figure 1.10:** Blood-cell development progresses from a hematopoietic stem cell (HSC), which can undergo either self-renewal or differentiation into a multilineage committed progenitor cell: a common lymphoid progenitor (CLP) or a common myeloid progenitor (CMP). These cells then give rise to more-differentiated progenitors, comprising those committed to two lineages that include T cells and natural killer cells (TNKs), granulocytes and macrophages (GMs), and megakaryocytes and erythroid cells (MEPs). Ultimately, these cells give develop into unilineage committed progenitors for B cells (BCPs), NK cells (NKPs), T cells (TCPs), granulocytes (GPs), monocytes (MPs), erythrocytes (EPs), and megakaryocytes (MkPs). Cytokines and growth factors that support the survival, proliferation, or differentiation of each type of cell are shown in red. IL denotes interleukin, TPO thrombopoietin, M-CSF macrophage colony-stimulating factor, GM-CSF granulocyte-macrophage CSF, and EPO erythropoietin. Reproduced with permission from [66]. ©(2006) Massachusetts Medical Society.

receptors CD14 and CD16 monocytes are further classified into classical monocytes ( $CD14^{++} CD16^{-}$ ), non-classical monocytes ( $CD14^{+} CD16^{++}$ ) and intermediate monocytes ( $CD14^{++} CD16^{+}$ ) [72].

**Lymphocytes** are the smallest leukocytes with a diameter of 7  $\mu m$  to 15  $\mu m$  [68]. They are comprised of T cells, B cells and NK cells. **T cells** belong to the adaptive immune system which means they have to learn which microorganisms are harmful. Their immunological maturation takes place in the thymus, where they develop T cell specific receptors. By antigen presentation of other immune cells T cells recognize invader and generate specific responses to eliminate specific pathogens or pathogen-infected cells. T cells are further classified into cytotoxic T cells, which produce enzymes that kill pathogen-infected cells and T helper cells, which produce cytokines to direct the immune response [73]. **B cells** are part of the adaptive immune system as well. They are primed in the bone marrow and are activated by foreign antigens. An activated B cell differentiates into plasma cells that produce antibodies against the antigen for immediate protection and memory B cells for persistent protection [74]. In contrast, **NK cells** are part of the innate immune system and do not require activation to kill cells that have a missing expression of certain cell surface markers like MHC class 1, which is often the case for tumor cells. They do this by releasing perforin and granzymes in close proximity to target cells, which induces either apoptosis or osmotic cell lysis. Recent research revealed that NK cells may also play an important role in the adaptive immune response [75].

The above mentioned cell types are distinguishable by the expression of cell surface markers. A selection of some frequently used markers is shown in Table 1.1.

Marker	Cell population	Marker	Cell population
CD34	HSCs	CD16	NK cells, neutrophils, monocytes
CD45	All leukocytes, HSCs	CD19	B cells
CD3	All T cells	CD54	NK cells, monocytes, T cells
CD4	T helper cells	CD56	NK cells
CD8	Cytotoxic T cells	CD62L	T cells, NK cells, neutrophils, monocytes
CD14	Neutrophils, monocytes	CD62P	Monocytes

**Table 1.1:** Expression of surface markers by the main leukocyte populations and hematopoietic stem cells according to [76–78].

## 1.4 *In vitro* and *ex vivo* breast cancer models

To understand the uptake of GQDs into solid tumors, in the present work the breast cancer cell lines MCF-7 and MDA-MB-231 are used as *in vitro* models together with the MCF-10A cell line as a comparison for benign cells. The analysis is then extended to the closer to reality *ex vivo* model of MMTV-PyMT precision-cut tumor slices. Both model systems are briefly introduced in the following.

**In vitro models:** The **MCF-7** cell line was established at the Michigan Cancer Foundation (MCF) in 1970 from a 69-year-old caucasian woman [79] and represents the most studied breast cancer cell type [80]. MCF-7 cells are progesterone receptor positive, estrogen receptor positive and HER2 (ErbB2) negative and are therefore a standard model for estrogen receptor positive breast cancer [81] as well as for the development of treatment resistance to estrogen receptor antagonists [82]. The **MDA-MB-231** cell line was established at M.D. Anderson (MDA) hospital in 1973 from a 51-year-old caucasian woman [83]. MDA-MB-231 cells are progesterone receptor negative, estrogen receptor negative and HER2 negative and therefore represent an example for especially difficult to treat triple-negative breast cancer with highly aggressive, invasive and poorly differentiated cells [84]. The MDA-MB-231 cell line belongs to the most relevant *in vitro* breast cancer models [85] and is well established in metastasis research [86]. In contrast, the **MCF-10-A** cell line is an example for benign epithelial cells from mammary gland tissue. The cell line was established at the Michigan Cancer Foundation in 1989 from a 36-year-old caucasian woman with fibrocystic disease [87] and represents the most common used model for normal breast cells [88].

**The *ex vivo* model of MMTV-PyMT precision-cut tumor slices:** Monoclonal cell lines are not able to represent the heterogeneity of a solid tumor [89] and may display geno- and phenotypic changes due to long-lasting *in vitro* cultivation [90]. On the contrary, *ex vivo* cultivated precision-cut tissue slices contain all cell types of the tissue and allow to study multicellular biochemical processes like transport of drugs in a more natural environment [91]. Transgene **MMTV-PyMT** mice expressing the *Polyomavirus Middle T Antigen* (PyMT) under transcriptional control of the *Mouse Mammary Tumor Virus Promoter* (MMTV) rapidly develop multifocal metastasizing adenocarcinoma of the mammary gland [92]. Compared to the human disease the model presents various similarities on histological and tumor biological levels, especially regarding prognostic biomarkers: On the way

to more invasive stages a loss of estrogen and progesterone receptors is as well depicted as an overexpression of HER2 and Cyclin D1, which coincide with a poor prognosis in the human disease [93].

## 2 Experimental techniques

This chapter deals with the experimental techniques used in this thesis. First, the established process for the preparation of GQDs based on the pyrolysis of citric acid is presented. Then, the methods, that were used to characterize the as prepared GQDs, are introduced: fluorescence spectroscopy and ultraviolet-visible spectrophotometry, X-ray photoelectron spectroscopy, transmission electron microscopy and Raman spectroscopy. Finally, the applied techniques to analyse the uptake of the GQDs into the cells and the reaction of the cells to GQDs are explained, which include flow cytometry, confocal fluorescence microscopy, XTT and MTT assay as well as gene expression analysis based on microarray technique.

### 2.1 Preparation of graphene quantum dots

In general, the synthesis of GQDs is classified into two groups: top down and bottom up approaches. Top down approaches start with bulk materials consisting

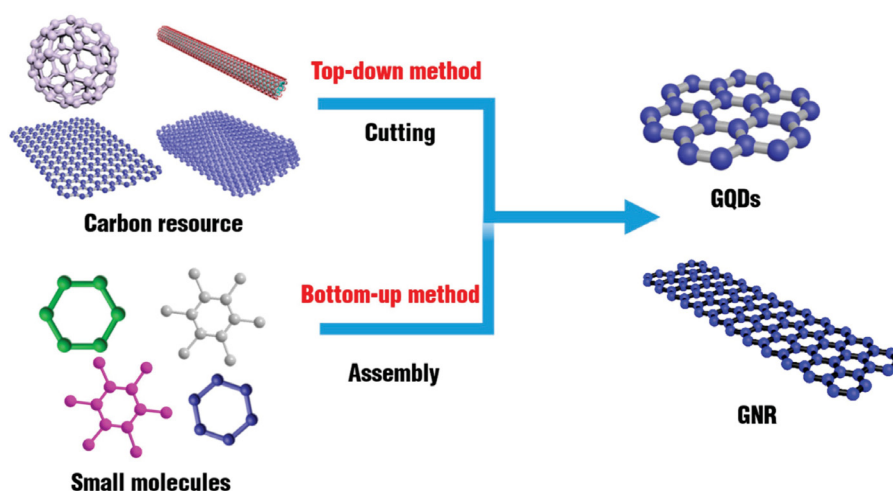


**Figure 2.1:** Schematic illustration of the top down and bottom up approaches for GQD synthesis (taken from [94] under Creative Commons Attribution 4.0 International license). Top down approaches cut bulk materials into smaller pieces while bottom up approaches use small organic starting materials to form GQDs with solution chemistry.

of carbon like graphite, graphene, coal, carbon nanotubes or carbon black and



## 2.1. Preparation of graphene quantum dots

apply methods like chemical acid oxidation [95, 96], hydrothermal cutting [97], electrochemical cutting [29, 98] or ultrasonic exfoliation [99] to cut small pieces, that finally form the GQDs, out of the bulk material. In contrast, bottom up approaches use small organic starting materials like citric acid [13, 27, 56], glucose [100], aspartic acid [101] or phloroglucinol [20] and apply stepwise solution chemistry to form GQDs [94]. Both approaches are illustrated in Figure 2.1.

In the present work only bottom up approaches based on citric acid were used to prepare GQDs as these approaches present as easy to use, scalable and reproducible. Paper 1 [1] applied the method of Wu et al. [27], which forms GQDs by the pyrolysis of citric acid in the presence of dicyandiamide as reduction agent: 70 mg citric acid and 250 mg dicyandiamide are resolved in 4 ml DI water in a stainless steel

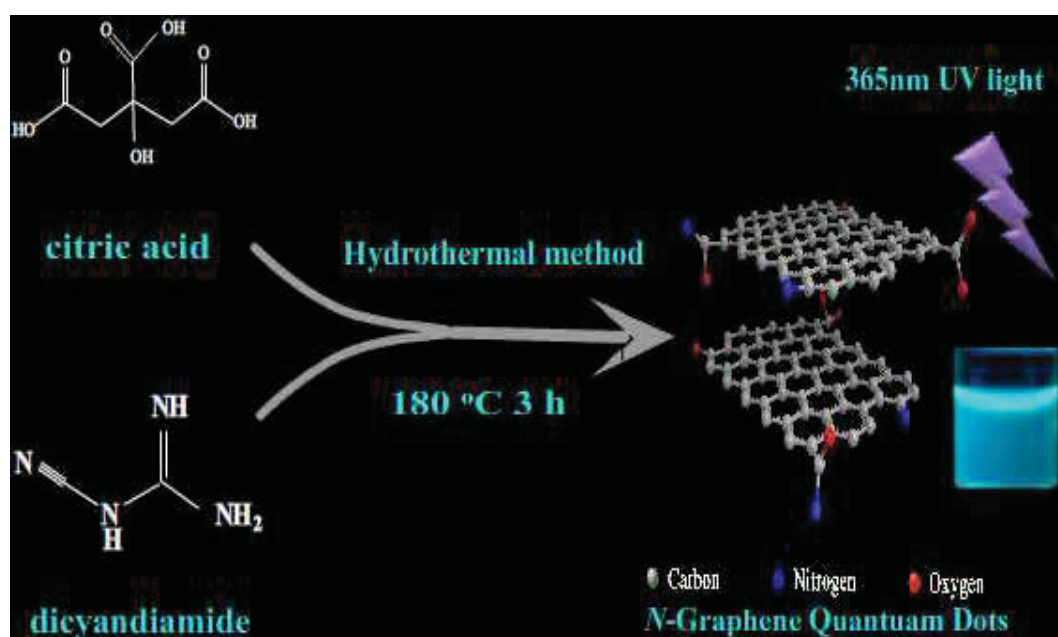


**Figure 2.2:** Illustration of the formation process of GQDs from citric acid and dicyandiamide (Reprinted with permission from [27]. ©(2014) The Royal Society of Chemistry). A solution of dicyandiamide and citric acid is heated to 180° C for 3 h. GQDs are formed due to the pyrolysis of citric acid and contain nitrogen at the edges due to dicyandiamide.

autoclave and heated to 180° C for 3 h on a hot plate under continuous stirring. Afterwards waste is removed by dialysis (see the methods section of Paper 1 for more details). Figure 2.2 illustrates the hydrothermal process. The as prepared GQDs emit their strongest fluorescence at an excitation wavelength of 360 nm and do not emit fluorescence at 488 nm excitation. Excitation at 488 nm is preferable for medical applications as this avoids excitation of cells with UV light and most



medical standard devices like flow cytometers and fluorescence microscopes are equipped with a 488 nm argon-ion laser. Therefore Paper 2 [2] and Paper 3 [3] applied the method of Qu et al. [56]. Qu et al. also use citric acid as carbon source but change the reduction agent to diethylentriamine. Briefly, 210 mg citric acid and 340 mg diethylentriamine are stirred in a stainless steel autoclave and heated to 180° C for 6 h before waste is removed by dialysis. The change of the reduction agent from dicyandiamide to diethylentriamine leads to GQDs that still have their fluorescence maximum at 360 nm excitation but also have some absorbance at the  $n - \pi^*$  transition of the N state (see chapter 1.2.1) and therefore emit fluorescence in the yellow at 488 nm excitation.

The preparation process inside a stainless steel autoclave does not allow to monitor

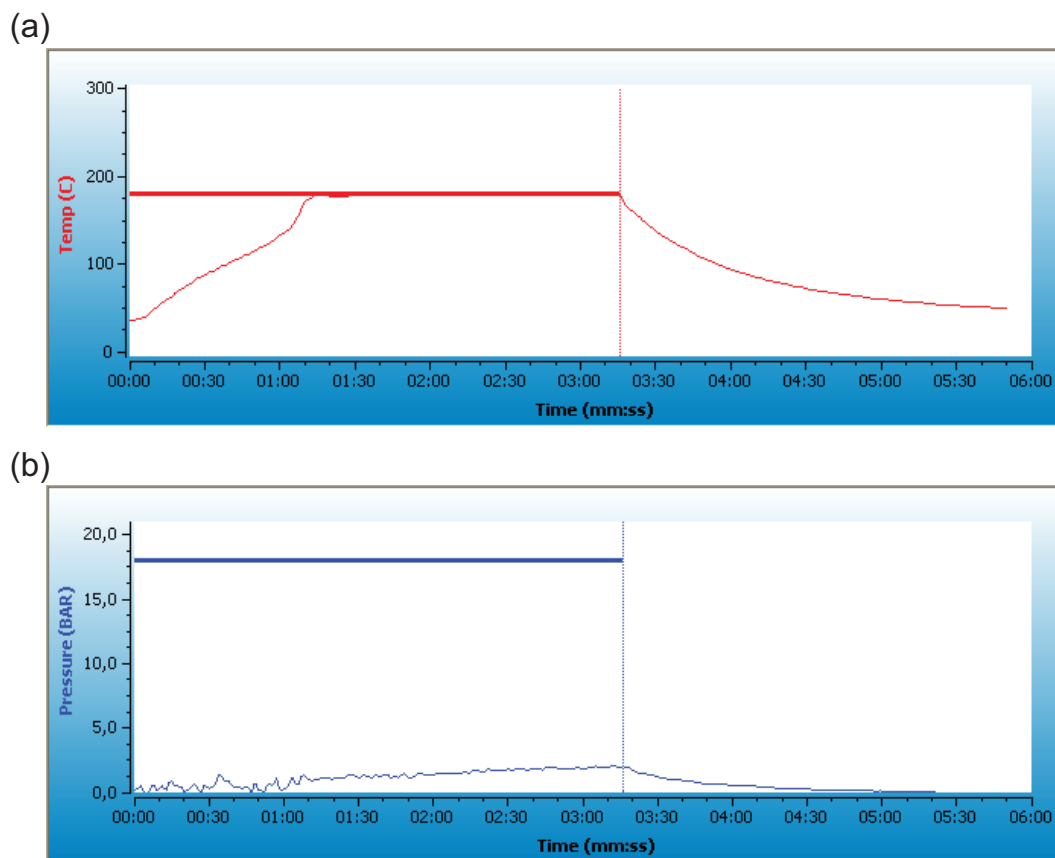


**Figure 2.3:** (a) Temperature profile and (b) pressure profile of the microwave assisted GQD synthesis. The sample is heated to 180° C and the temperature is kept for 2 minutes. Afterwards the sample is cooled down within 2.5 minutes. During the synthesis the pressure never exceeds 2 bar. The red and the blue straight line show the temperature and the pressure maximum that are set for this reaction.

temperature and pressure during the reaction, may be dependent on the surface area of the autoclave and is completed by an undefined cooldown process. Therefore, the reaction process was switched to a CEM Discover SP microwave synthesizer, which enables the monitoring of reaction temperature and pressure as well as a defined cooldown process. The synthesis time in the microwave synthesizer could be shortened to 2 minutes without significant change of the GQD's optical properties, while the quantity of chemicals used by Qu et al. was maintained. The temperature and pressure profile of the microwave assisted GQD synthesis is shown in Figure 2.3. Within 70 seconds the sample is heated to 180° C and the temperature is kept for 2 minutes. Afterwards, the sample is cooled down within 2.5 minutes. During the synthesis the pressure never exceeds 2 bar, as the boiling point of diethylentriamine of 205° C [102] is not reached and the pressure drops to zero after the cooldown, which means no significant generation of gases takes place during the reaction. The obtained solution is then filtered by dialysis to remove waste and obtain an aqueous GQD solution (see the methods section of Paper 2 and Paper 3 for more details).

## 2.2 Analysis of graphene quantum dots

### 2.2.1 Fluorescence spectroscopy and ultraviolet-visible spectrophotometry

To analyse the optical properties of the GQDs, fluorescence spectroscopy and ultraviolet-visible spectrophotometry are used. A scheme of the measurement principle is shown in Figure 2.4. For fluorescence measurements GQDs are solved

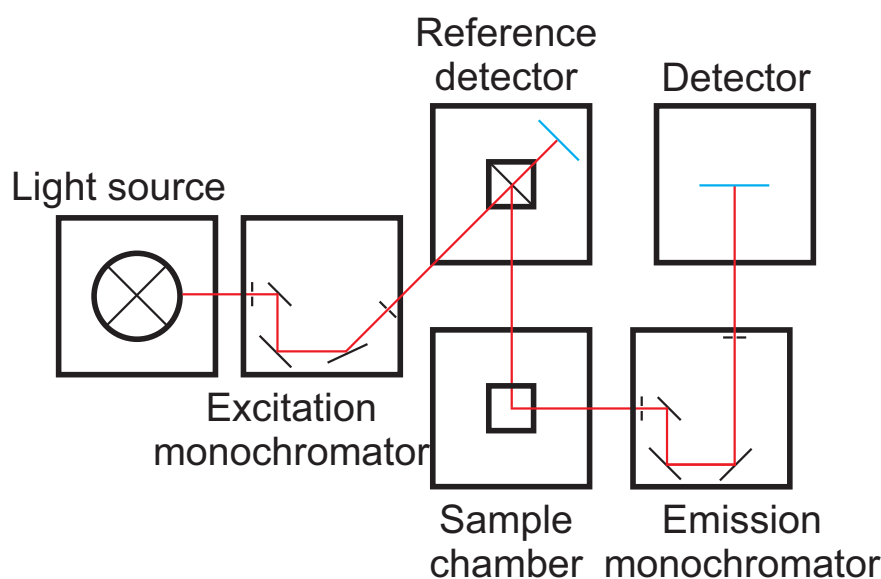


**Figure 2.4:** Scheme of a fluorescence spectrofluorometer. The emission of the light source is filtered by a monochromator, recorded by a reference detector and guided to the sample. The sample emits photons in all directions. For fluorescence spectroscopy the emitted light is detected perpendicular to the excitation beam (after selection by the emission monochromator) to avoid detection of the scattered excitation beam. For absorbance measurements the light is detected parallel to the direction of the excitation. Comparison with the reference measurement of the excitation beam allows the calculation of the sample's absorbance.

in water at a defined concentration and given into a cuvette that is placed inside the sample chamber of the spectrofluorometer. A light source with a continuous spectrum is filtered by a grating monochromator to select the excitation wavelength. The selected light is recorded by a reference detector before the light is guided to the sample. The excited sample emits light in all directions and the emitted light is detected perpendicular to the excitation beam to avoid detection of scattered excitation light. Before the light is detected it is selected by the

emission monochromator, which consists out of a grating and two slits. A stepper motor changes the position of the slits to scan the whole spectrum of emission wavelengths for a given excitation wavelength. Absorption measurements, which are usually mentioned as ultraviolet-visible spectrophotometry (UV-Vis), follow the same principle, but the light is detected in parallel to the direction of the excitation instead of perpendicular. The samples absorbance can than be calculated as

$$E = \log_{10} \frac{I_0}{I_1} = \epsilon \cdot c \cdot d \quad [103] \quad (2.1)$$

with the absorbance  $E$ , the recorded reference signal  $I_0$  of the excitation intensity, the detected signal  $I_1$  after passing the sample, the extinction coefficient  $\epsilon$ , the molar concentration  $c$  and the thickness of the sample  $d$ . For all experiments in this thesis the HORIBA Fluoromax 4 spectrofluorometer was used for fluorescence measurements and absorption measurements were carried out on the Agilent Technologies Cary 4000 UV-Vis spectrofluorometer.

### 2.2.2 X-ray photoelectron spectroscopy

X-ray photoelectron spectroscopy (XPS) is a method to measure the elemental composition, chemical states and electronic states at the surface of a sample. The method was significantly developed by Kai Siegbahn [104] who finally got the Nobel Prize in Physics 1981 for that achievement [105]. The method is based on the photoelectric effect [106]: A sample is irradiated by X-ray with the energy  $E = h\nu$  under ultra high vacuum and the sample is grounded to avoid charging. If the excitation energy is high enough, electrons from atoms in the surface region are knocked out of the electron shell and released in the surroundings with a well-defined kinetic energy  $E_{kin}$  (external photoelectric effect). The kinetic energy of the released electrons is measured by a hemispherical capacitor and the binding energy of the electron can be calculated as:

$$E_B = h\nu - E_{kin} \quad (2.2)$$

The binding energy of the electron is dependent on the atomic orbital where the electron comes from and on the chemical composition of the sample. Therefore not only information about the chemical composition but also more specific information about functional groups (that have slightly different binding energies) can be

obtained by XPS. The information depth is dependent on the mean free path of the electrons through the sample and is usually in the range of a few nm. [107] The principle and a typical XPS-measurement are shown in Figure 2.5.

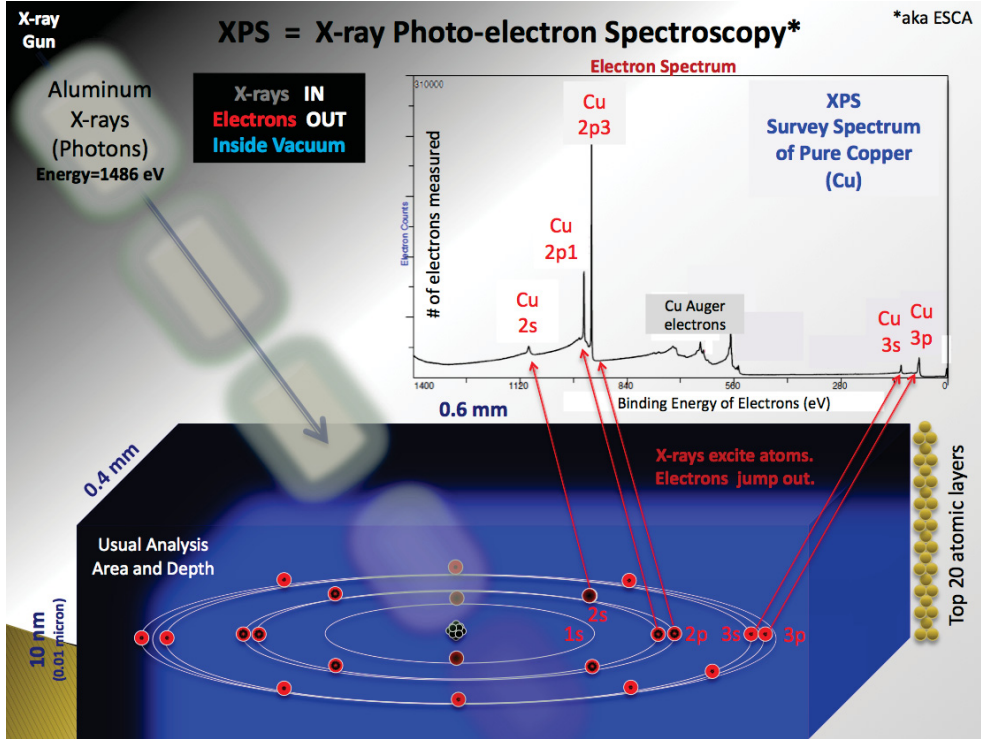


**Figure 2.5:** Illustration of a XPS setup and the basic physical principles. Picture taken from [108], marked as public domain. Photoelectrons are emitted after X-ray irradiation and have different kinetic energies according to their atomic orbital. Their binding energy can be calculated out of the measured data using  $E_B = h\nu - E_{kin}$ , which leads to substance and orbital specific peaks.

The XPS-measurements in the present work were carried out by Dr. Besmehn and Dr. Hartmann at ZEA-3 of Jülich Research Center on a Phi5000 VersaProbe II XPS instrument. For that purpose the GQDs were dried immediately before the measurement at a concentration of  $500 \mu\text{g ml}^{-1}$  on an Au-substrate and measured under ultra high vacuum.

### 2.2.3 Transmission electron microscopy

Transmission electron microscopy (TEM) uses a beam of electrons which is transmitted through a specimen to form an image with a significantly higher resolution as compared to light microscopes, due to the smaller de Broglie wavelength of the

electrons. The technique was developed by Max Knoll and Ernst Ruska in 1931 and Ruska was awarded the Nobel Prize in Physics 1986 for that achievement [109]. Figure 2.6 shows the layout and the path of the electrons of a typical transmission electron microscope: The whole system is operated under ultra high vacuum. The

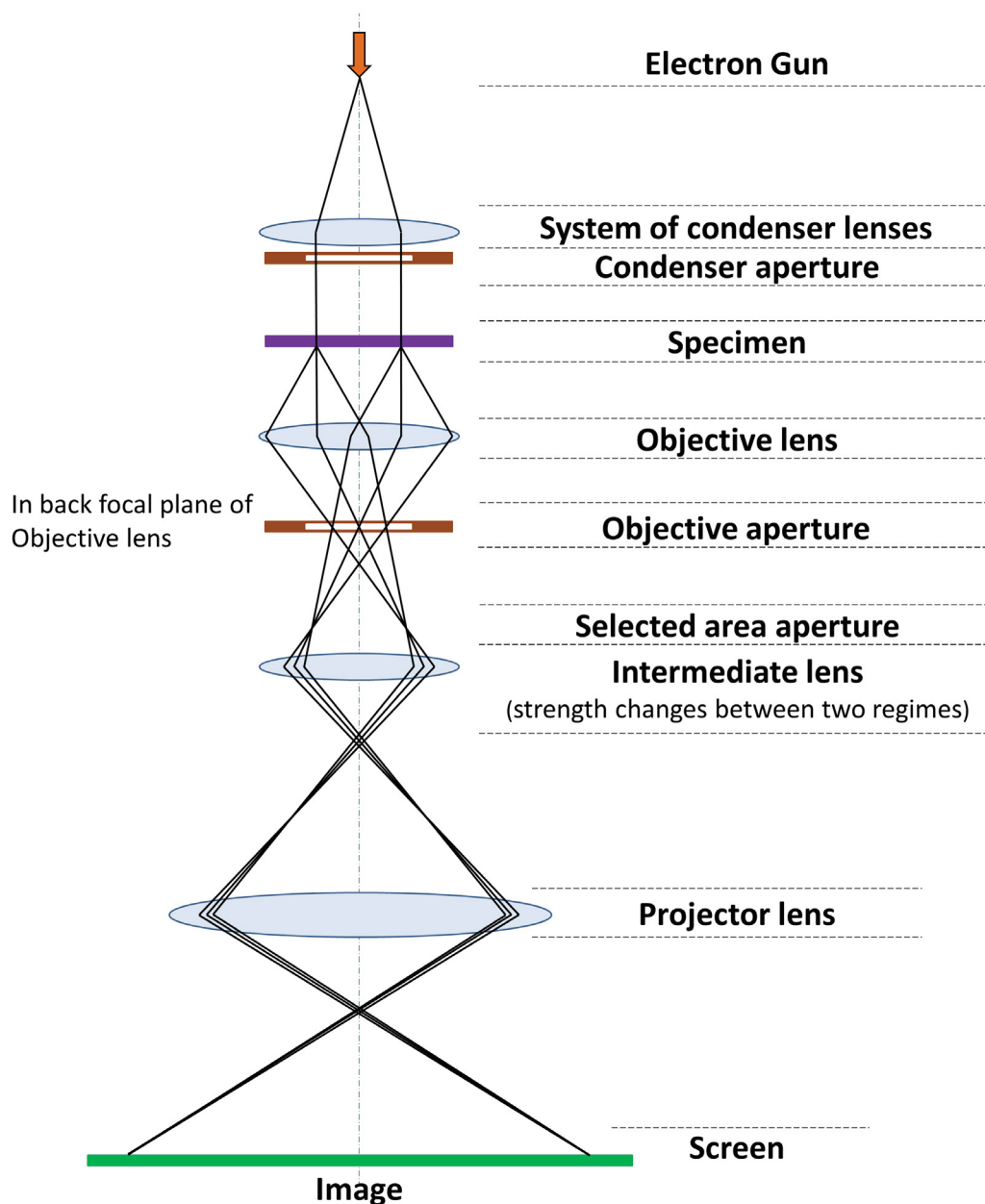


**Figure 2.6:** Layout of the optical components and path of the electrons in a basic TEM. Picture taken from [110] under Creative Commons Attribution-ShareAlike 4.0 International license.

electron gun often consists out of a tungsten filament that is connected to a high

voltage source (100 - 300 kV) and emits electrons by thermionic or field electron emission [111]. The emitted electrons are accelerated by electrostatic plates and focused into a nearly parallel beam on the specimen by the condenser lens system, which consists of solenoid coils that guide the electrons through magnetic fields. Due to Rutherford scattering the electrons change their direction of movement while passing the sample. Electrons that are scattered elastically are focused in the back focal plane of the objective lens. The objective aperture enables to remove scattered electrons, which creates the mass-thickness contrast, as atoms with a higher atomic number or thicker areas of the sample scatter electrons at higher angles. The intermediate and the projector lenses magnify and project the image on a screen. Another important contrast is the phase contrast: Before an electron hits a crystalline sample it can be approximated as a plane wave. Inside of the sample the electron wave experiences phase shifts, due to interaction with the positive potential of the atom cores, which reflect the periodic arrangement of the atoms in the crystal lattice. Using the phase contrast of the electron exit wave, that is a superposition of a plane wave and many diffracted beams, resolutions as good as  $0.5 \text{ \AA}$  are possible [112]. A detailed description how to obtain the phase contrast image can be found in [113].

The TEM images of this thesis were taken by Martina Luysberg at the Ernst Ruska-Center of Jülich Research Center on the Titan G3 50-300 PICO [114]. For that purpose the GQDs were dried immediately before the measurement at a concentration of  $20 \mu\text{g ml}^{-1}$  on ultra thin amorphous carbon TEM grids and measured under ultra high vacuum.

### 2.2.4 Raman spectroscopy

Raman spectroscopy is a method to measure vibrational modes of molecules, which gives information about chemical composition, chemical bonding, intramolecular bonds and the crystallographic orientation of a sample [115]. The technique is based on the inelastic scattering of light, which was predicted by A. Smekal in 1923 [116] and for the first time observed in an organic liquid by C.V. Raman and K. S. Krishnan [117] and in inorganic crystals by G. Landsberg and L. Mandelstam in 1928 [118]. The Nobel Prize in Physics 1930 was awarded to Raman for this discovery [119].

Figure 2.7 shows a basic Raman setup: A laser is focused in a line on the sample (by removing the cylindrical lens this can also be done using a spot) that is usually

placed in a mirrored sample holder. The external electric field of the illuminating

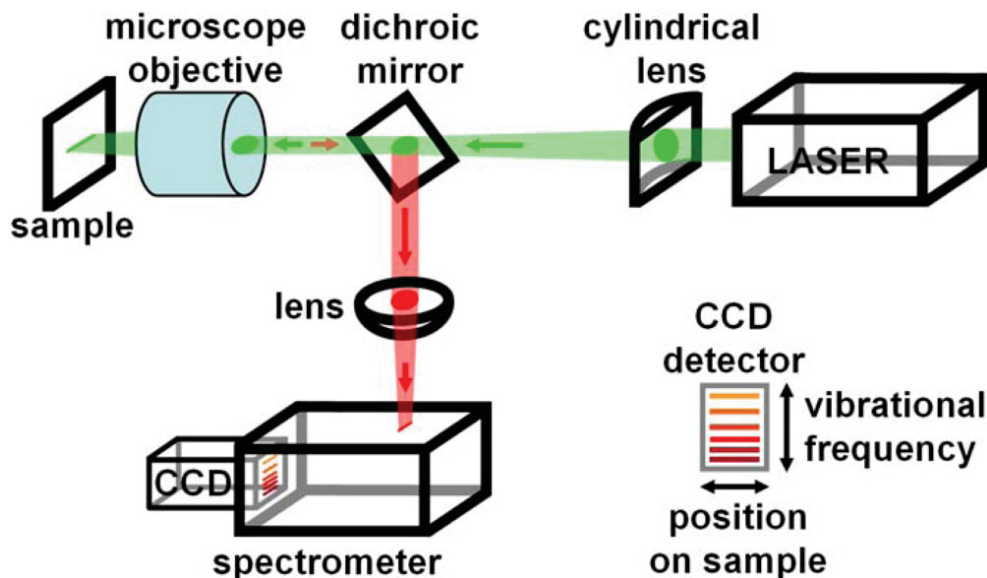


**Figure 2.7:** Schematic of a Raman spectrometer. Picture taken from [120] under Creative Commons Attribution 3.0 Unported license.

light interacts with the electron cloud of the sample (it is important that the laser light does not excite the molecule, no fluorescence is emitted). This interaction changes the rotational or the vibrational state of the molecule: the photon of the illuminating light may transfer energy to the scattering molecule, which is called Stokes-Raman-scattering or the scattering molecule may transfer energy to the photon, which is called Anti-Stokes-Raman scattering. The scattered light then has a slightly different wavenumber and energy as compared to the illuminating light and is filtered out by a dichroic mirror, which guides the light through a lens to a spectrometer to analyse the energy shift. Usually this so called Raman shift is reported in wavenumbers in the unit  $cm^{-1}$ , which is calculated by:

$$\Delta\nu(cm^{-1}) = \left( \frac{1}{\lambda_0(nm)} - \frac{1}{\lambda_1(nm)} \right) \times \frac{10^7 nm}{cm} \quad (2.3)$$

where  $\Delta\nu$  is the Raman shift,  $\lambda_0$  the excitation wavelength and  $\lambda_1$  the measured wavelength.

The Raman spectra used in this thesis were taken by Bastian Moll from the Institute for Inorganic Chemistry and Structural Chemistry of Heinrich-Heine-University Düsseldorf on a Bruker MultiRam-FT Raman spectrometer equipped with a ND:YAD-laser (excitation wavelength 1064 nm). For that purpose the



GQDs were measured in water dispersion at a concentration of  $100 \text{ mg ml}^{-1}$  in a mirrored cuvette with a laser power of 950 mW for 5000 scans.

## **2.3 Analysis of the cells exposed to graphene quantum dots**

### **2.3.1 Flow cytometry**

Flow cytometry is a method to measure the characteristics of cells based on the scattering of laser light as well as the fluorescence of the cell that is excited by the laser light. W. Dittrich and W. Göhde developed the first fluorescence based flow cytometer in 1968 [121] and Becton Dickinson developed the first fluorescence-activated cell sorting device (FACS) in 1974. FACS is often used as a synonym for flow cytometry although it is a registered trademark of Becton Dickinson and many flow cytometers do not allow cell sorting [122].

Figure 2.8 shows the setup of a flow cytometer: A cell suspension enters the device and single cells are pulled out of the suspension by a sheath fluid, which is called hydrodynamic focusing [123]. The single cells are guided to a laser beam, which is scattered by the cell. The scattered light is measured in direction of the laser beam (forward scatter, often called FSC), which is a measure for volume, and perpendicular to the direction of the laser beam (side scatter, often called SSC), which is a measure for morphological complexity of the cells [125]. Additionally the cells may be stained with fluorescent antibodies that are excited by the laser beam. The emitted light is detected by different fluorescence detectors and can be used as a quantitative measure e.g. for the expression of surface antigens [126].

The flow cytometry data used in this thesis were acquired on a Beckman Coulter CytoFLEX flow cytometer in close collaboration with Katharina Raba from the Institute for Transplantation Diagnostics and Cell Therapeutics of Heinrich-Heine-University Düsseldorf as well as on a BD FACSCalibur flow cytometer in close collaboration with Ron-Patrick Cadeddu from the Department of Haematology, Oncology and Clinical Immunology of Heinrich-Heine-University Düsseldorf.

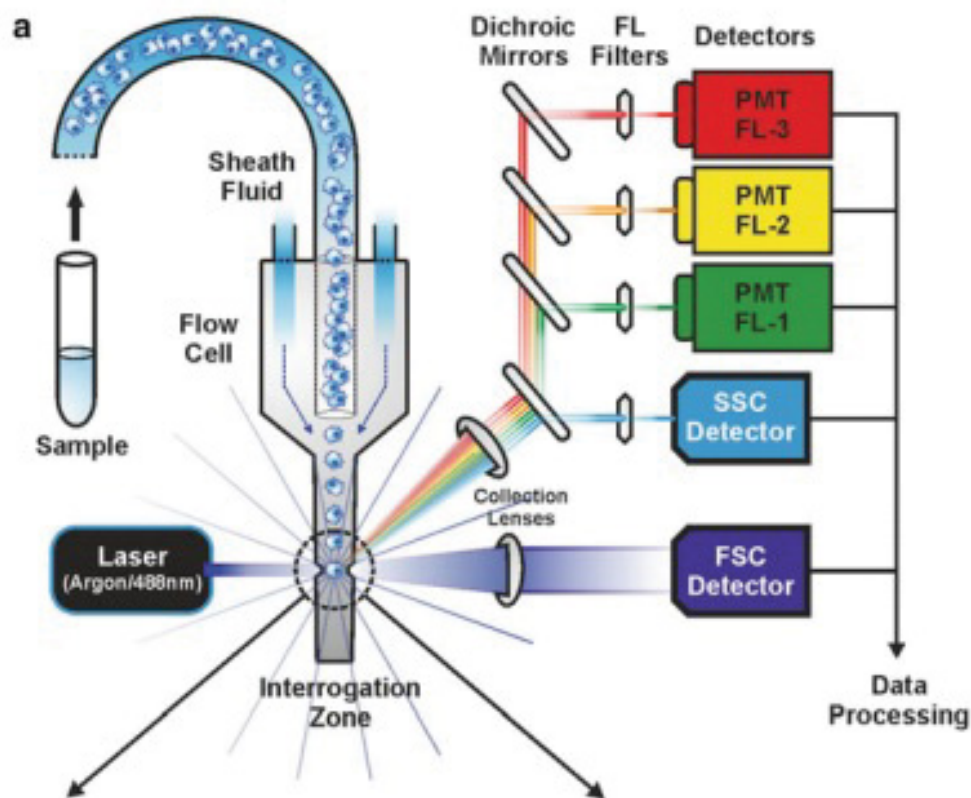


**Figure 2.8:** Principle of a flow cytometer. Reprinted with permission from [124] ©(2013) Springer Nature.

### 2.3.2 Confocal fluorescence microscopy

Confocal fluorescence microscopy, often mentioned as confocal laser scanning microscopy, is a method that uses a pinhole to block out-of-focus light, whereby the resolution and contrast of a micrograph is increased [127]. The first confocal optical system was developed by H. Goldmann in 1940 for the purpose of eye examinations [128]. M. Minsky used the confocal principle in 1955 for the first confocal scanning microscope [129] and M.D. Egger and P. Davidovits built the first confocal laser scanning microscope in 1969 [130].

Figure 2.9 shows the principle of a confocal fluorescence microscope: Excitation light is emitted through a pinhole, reflected by a dichromatic beam splitter and focused on a specimen by the objective. The excited fluorescence light is focused in an optically conjugate plane, where a pinhole is placed. Only light from the chosen confocal plane is able to pass through the detector, light from planes below or above the confocal plane is blocked. In that way only one point at a time is

illuminated, therefore it is required to scan over a raster to form 2D or 3D images, which is done by moving the stage that holds the specimen in x-,y- and z-direction. The confocal fluorescence micrographs used in this thesis were taken on a Zeiss LSM 710 confocal laser scanning microscope at the Center for Advanced Imaging of Heinrich-Heine-University Düsseldorf.

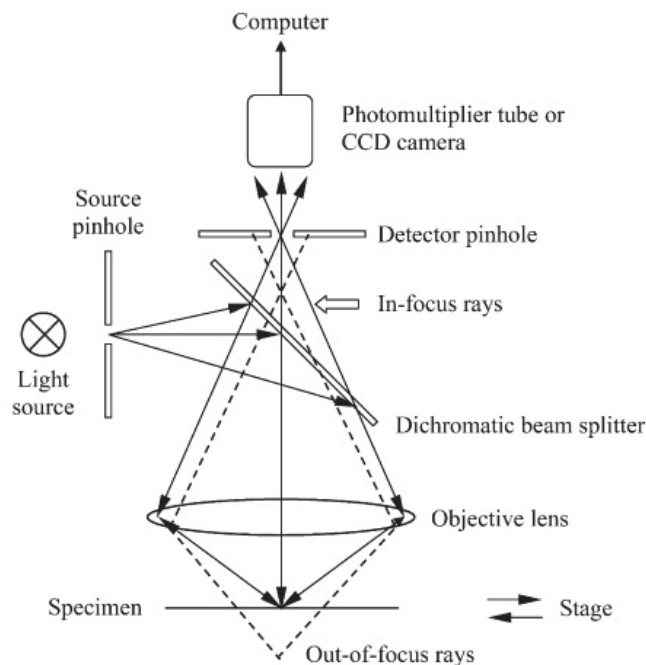


**Figure 2.9:** Principle of a confocal fluorescence microscope. Reprinted with permission from [131] ©(2004) Springer.

### 2.3.3 MTT and XTT assay

The MTT and the XTT assay are methods to measure cell metabolic activity. Under defined conditions this may be a measure for the number of viable cells. The MTT assay is based on the addition of the tetrazolium dye MTT 3-(4,5-dimethylthiazol-2-yl)-2,5-diphenyltetrazolium bromide to the cells, which reduce the dye through NAD(P)H-dependent cellular oxidoreductase enzymes to its insoluble formazan. DMSO has to be added to solve the formazan. In contrast to MTT the formazan has a high absorbance in the range between 500 nm and 600 nm (see Figure 2.10) and therefore the degree of light absorbance is a measure for the cells capability of metabolizing formazan. [133, 134] As many cell culture media like DMEM also absorb in the range between 500 nm and 600 nm the cell culture medium has to be

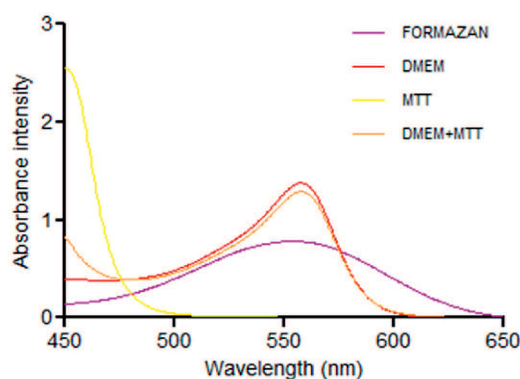


**Figure 2.10:** Absorbance of MTT, formazan and DMEM (which is a cell culture medium). The maximum absorbance of formazan is around 560 nm where the absorbance of MTT is essentially zero. Taken from [132] under Creative Commons Attribution 4.0 International license.

washed away before the measurement or the absorbance of the cell culture medium has to be subtracted out of the measured data.

The XTT assay is based on the same principle but uses XTT (2,3-bis-(2-methoxy-4-nitro-5-sulfophenyl)-2H-tetrazolium-5-carboxanilide) as dye, which has the advantage that its formazan is water-soluble, which avoids the final solubilization step [135].

#### 2.3.4 Gene expression profiling based on microarray technique

Gene expression profiling compares the expression levels (which are a measure for gene activity, that is quantified by measuring the amount of mRNA) of a large number of genes between two or more samples. It creates a global view on the cellular function and gives insight into the role of gene expression changes during disease development. Therefore, gene expression profiling is widely used not only in cancer research [136,137] but also to understand the underlying mechanisms of neurodegenerative diseases [138] and to monitor the toxicity of drugs [139].

Figure 2.11 shows the principle of gene expression profiling based on microarray technique. At least two samples are compared with each other - one represents the control and the other the condition(s) under study. The entire RNA (including the mRNA) is extracted and purified from the cells. Using reverse transcription polymerase chain reaction the RNA is transcribed into cDNA [141]. Furthermore, the cDNA is labeled with a fluorescent dye. Due to Watson-Crick base pairing there exists one specific DNA sequence that can hybridize with the corresponding

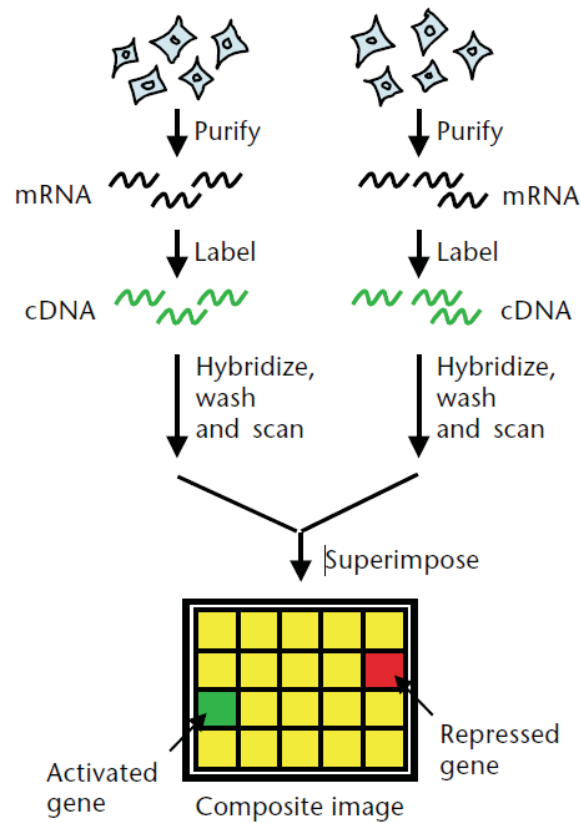


**Figure 2.11:** One-color expression analysis uses a single fluorescent label (green wavy lines) and two chips to generate expression profiles for two cell samples. Activated and repressed genes (green and red squares, respectively) are obtained by superimposing images obtained from different chips. Reprinted with permission from [140] ©(2003) Nature Publishing Group.

cDNA. These DNA fragments are bound in large amounts at defined positions on a chip. After hybridization with the cDNA the fluorescence intensity at the defined positions on the chip quantifies the amount of mRNA (one might also look at other types of RNA like miRNA) and therefore the expression of the given gene. Superimposition of the images on the chips for different conditions allows for quantitative comparisons.

### 3 Publications

The papers resulting from this work are given in this chapter and include:

1. *Uptake Dynamics of Graphene Quantum Dots into Primary Human Blood Cells Following in vitro Exposure*, S. Fasbender, S. Allani, C. Wimmenauer, R.P. Cadeddu, K. Raba, J.C. Fischer, B. Bulat, M. Luysberg, C.A.M. Seidel, T. Heinzl and R. Haas, RSC Advances **7**, 12208-12216 (2017)
2. *From in vitro to ex vivo: Subcellular localization and uptake of graphene quantum dots into solid tumors*, D. Kersting, S. Fasbender, R. Pilch, J. Kurth, A. Franken, M. Ludescher, J. Naskou, A. Hallenberger, C. von Gall, C. J. Mohr, R. Lukowski, K. Raba, S. Jaschinski, I. Esposito, J. C. Fischer, T. Fehm, D. Niederacher, H. Neubauer and T. Heinzl, Nanotechnology **30**, 395101 (2019)
3. *The Low Toxicity of Graphene Quantum Dots is Reflected by Marginal Gene Expression Changes of Primary Human Hematopoietic Stem Cells*, S. Fasbender, L. Zimmermann, R. P. Cadeddu, M. Luysberg, B. Moll, C. Janiak, T. Heinzl and Rainer Haas, Scientific Reports **9**, 1 (2019)

---

# **Uptake Dynamics of Graphene Quantum Dots into Primary Human Blood Cells Following in vitro Exposure**

## **Reference**

S. Fasbender, S. Allani, C. Wimmenauer, R.P. Cadeddu, K. Raba, J.C. Fischer, B. Bulat, M. Luysberg, C.A.M. Seidel, T. Heinzl and R. Haas, RSC Advances **7**, 12208-12216 (2017), Published by The Royal Society of Chemistry.  
<https://doi.org/10.1039/C6RA27829A>

## **Copyright statement**

This article is licensed under a Creative Commons Attribution 3.0 Unported License. Material from this article can be used in other publications provided that the correct acknowledgement is given with the reproduced material.

## **Contributions**

I participated in the planning and the conductance of the experiments and contributed to manuscript writing.

Cite this: *RSC Adv.*, 2017, 7, 12208

# Uptake dynamics of graphene quantum dots into primary human blood cells following *in vitro* exposure†

Stefan Fasbender,<sup>a</sup> Sonja Allani,<sup>a</sup> Christian Wimmenauer,<sup>a</sup> Ron-Patrick Cadeddu,<sup>b</sup> Katharina Raba,<sup>c</sup> Johannes C. Fischer,<sup>c</sup> Bekir Bulat,<sup>d</sup> Martina Luysberg,<sup>e</sup> Claus A. M. Seidel,<sup>d</sup> Thomas Heinzel<sup>\*a</sup> and Rainer Haas<sup>\*b</sup>

Human leukocytes obtained from samples of leukapheresis products of three healthy donors stimulated by granulocyte colony stimulating factor (G-CSF) were exposed to graphene quantum dots. A time- and concentration dependent uptake was observed with a significantly greater uptake into monocytes and granulocytes in comparison to lymphocytes, suggesting a better incorporation ability of cells with phagocytotic properties. The uptake rates also correlate with the cell membrane area. Looking at the different lymphoid subsets a greater uptake was found into CD19<sup>+</sup> B-, CD56<sup>+</sup> natural killer cells and CD34<sup>+</sup> hematopoietic stem cells (HSC) in comparison to CD4<sup>+</sup> T- and CD8<sup>+</sup> T cells. Independent of the cell type studied, the observed uptake dynamics is consistent with a diffusion-driven process, which allows the determination of cell-specific membrane permeabilities for the graphene quantum dots. The toxicity of the quantum dots is relatively low resulting in a 90% viability of the entire leukocyte population after 36 hours of exposure to GQDs at a concentration of 500 µg ml<sup>-1</sup>.

Received 6th December 2016

Accepted 8th February 2017

DOI: 10.1039/c6ra27829a

rsc.li/rsc-advances

## 1 Introduction

Semiconductor quantum dots are used in many fields of biology and medicine, like long term imaging of various normal and malignant cells *in vivo* and *in vitro*,<sup>1,2</sup> cancer diagnostics<sup>3,4</sup> and therapeutic tumor cell targeting.<sup>5,6</sup> Their application is advantageous because of their long-term photostability, tunable color and high photoluminescence quantum yield. Still, potential toxic side effects are an important issue prompting the search for suitable alternatives which also necessitate comprehensive studies as far as biocompatibility, toxicity and applicability are concerned. Graphene quantum dots (GQDs) are promising candidates sharing the advantages of semiconductor quantum dots without their intrinsic toxicity.<sup>7</sup> In addition, their production is relatively easy, reproducible and inexpensive. The spectrum of applications includes photocatalysts, ion detectors,

solar cells with improved light-to-energy conversion, drug delivery and biomarkers.<sup>8</sup> Due to their solubility in water, additional coatings are not necessary for studies in bio-environments. GQDs enter into the cytoplasm of different human cell lines as well as in human neural stem cells most likely *via* endocytosis without obvious negative effects on cell proliferation.<sup>9–12</sup> Their fluorescence intensity depends on the environmental pH value,<sup>13</sup> a relevant parameter related to membrane permeability, cell-cell coupling, metabolism and fertilization.<sup>14</sup> *In vivo* studies have shown that GQDs accumulate in the kidney with a time constant of approximately 3 hours after subcutaneous and intravenous injection in mice, before they are excreted *via* the urine.<sup>15</sup> As far as cancer therapy is concerned, it was interesting to observe that GQDs are able to pass the blood-brain barrier with enhanced uptake in glioma tissue in comparison to normal brain cells.<sup>16</sup> GQDs are also believed to enhance the potency and selectivity of cancer drugs like cisplatin and doxorubicin.<sup>17,18</sup> While larger sheets of graphene oxide show significant toxicity,<sup>19</sup> GQDs are often considered to be less toxic with a dependency on particle size, charge and impurities.<sup>20</sup> We are interested in the interaction of GQDs with blood cells and its stem and progenitor cells, because the later ones have a great potential of differentiation and are particularly sensitive to all kind of genotoxic effects. For instance, in the treatment of patients with cytotoxic chemotherapy, the hematopoietic system represents most often the dose-limiting organ. For our *in vitro* studies, we used the preparation process of Wu *et al.* due to its excellent

<sup>a</sup>Condensed Matter Physics Laboratory, Heinrich-Heine-University, 40204 Düsseldorf, Germany. E-mail: Thomas.Heinzel@hhu.de

<sup>b</sup>Department of Haematology, Oncology and Clinical Immunology, Heinrich-Heine-University, 40204 Düsseldorf, Germany. E-mail: Haas.med@uni-duesseldorf.de

<sup>c</sup>Institute for Transplantation Diagnostics and Cell Therapeutics, Heinrich-Heine-University, 40204 Düsseldorf, Germany

<sup>d</sup>Institute of Molecular Physical Chemistry, Heinrich-Heine-University, 40204 Düsseldorf, Germany

<sup>e</sup>Ernst Ruska-Centre, Jülich Research Centre, 52425 Jülich, Germany

† Electronic supplementary information (ESI) available: Additional figures with AFM, TEM, XPS and fluorescence images. Additional data characterizing the quantum dots. See DOI: 10.1039/c6ra27829a



reproducibility of the quantum yield and the fluorescence spectra in our laboratory. The obtained GQDs with a diameter of approximately 2 nm are not only excellent fluorescence markers, but are also suitable for drug delivery as well as for functional studies inside cells.<sup>13</sup> We also view GQDs as model particles for other kinds of graphitic particles, which are abundantly present in the environment due to *e.g.* combustion.

## 2 Results and discussion

### 2.1 Preparation and characterization of the graphene quantum dots

The GQDs were prepared by pyrolysis of citric acid<sup>21</sup> under high pressure and in the presence of dicyandiamide to ensure nitrogen adsorbates at their edges.<sup>13</sup> The dots were purified by dialysis yielding particles with a minimum mass of 500 Da and a maximum mass of 20 kDa. Some of these GQDs were placed on a silicon dioxide substrate for characterization by scanning force microscopy, showing a height of 0.7 nm to 1.3 nm (see Fig. S1†) which is consistent with one to three layers of graphene.<sup>22,23</sup> TEM images of the GQDs (see Fig. S2†) reveal almost circular particles with a diameter around 2 nm (ranging from 1–3 nm). We used X-ray photoelectron spectroscopy (XPS) to determine the chemical composition. The relative strength of the C 1s, N 1s and O 1s peaks indicate that the GQDs are composed of 50% carbon, 30% nitrogen and 20% oxygen atoms (see Fig. S3†). The carbon 1s XPS spectrum is the most relevant (see Fig. 1A). According to a best fit analysis, the C 1s signal around an energy of 287 eV is composed of five significant terms, plus three terms of low weight which will not be discussed here. Approximately 36% of the total signal strength originates from a peak centered at 285.0 eV, corresponding to C–C bonds of  $sp^2$  hybridized carbon as it is characteristic for carbon atoms in graphene.<sup>24</sup> The peak at 288.2 eV, contributing a weight of 19.4%, stems from the C=O double bond, which is interpreted as oxidized bulk graphene that generates a local  $sp^3$ -hybridization. The C=O double bond also appears in combination with nitrogen with a similar weight of 16.5% at an energy of 289.0 eV. We attribute this arrangement to C atoms at the GQD edge which have only a single bond to one neighboring C atom of the graphene layer. Furthermore, another 11.0% is contributed by the O–C=O group, which is also a plausible conformation at the GQD edge. Finally, 8% of the total signal is due to the C–O single bond. This analysis suggests that about one third of the carbon atoms in the bulk of the GQDs is oxidized, and oxygen as well as nitrogen are engaging the loose bonds of the carbon atoms at the edge. Our results differ somewhat from those obtained by Wu *et al.*<sup>13</sup> for GQDs prepared by a very similar method. They observed a larger fraction of nitrogen bonds, which may be explained by the different filter parameters they used. Absorption- and fluorescence spectroscopy was carried out for optical characterization (see Fig. 1B and C). A prominent absorbance peak is observed at a wavelength of 340 nm, which can be attributed to the  $n-\pi^*$  transition the C=O site.<sup>25</sup> Along with a reduction of the wavelength below 280 nm, a strong increase in absorption is observed, with a superimposed peak at  $\approx 235$  nm, which is usually attributed

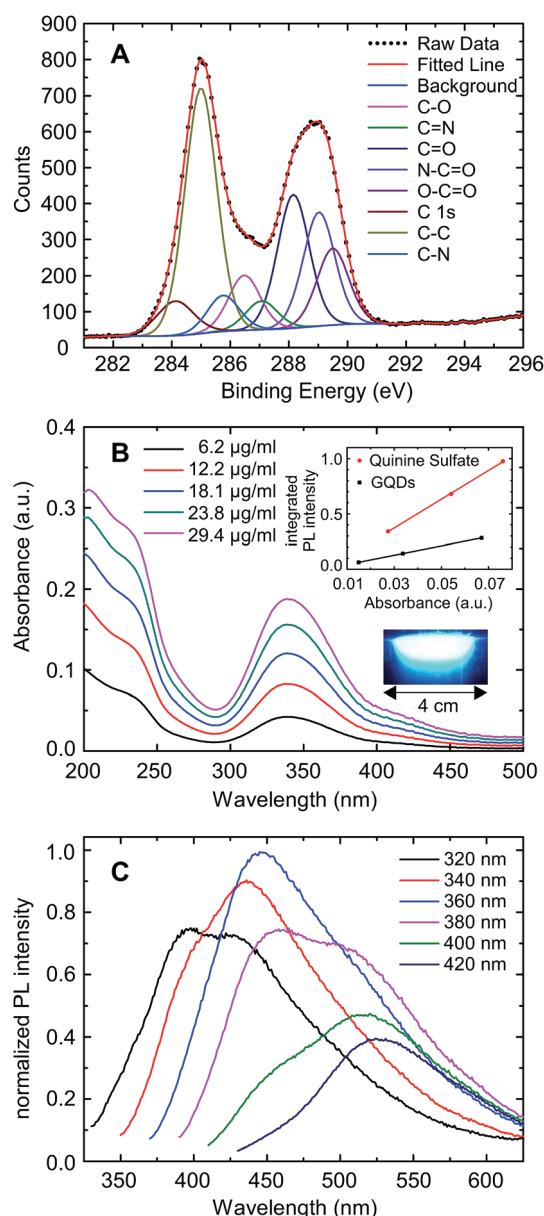


Fig. 1 (A) XPS spectrum of the GQDs at the carbon 1s state (dots) and its composition, based on a best fit analysis. (B) Absorption spectra of the GQDs in aqueous solution. The upper inset shows the integrated PL intensity vs. absorbance of quinine sulfate and GQDs at concentrations of  $3 \mu\text{g mL}^{-1}$ ,  $6 \mu\text{g mL}^{-1}$  and  $12 \mu\text{g mL}^{-1}$  and the lower inset shows an image of the GQD solution excited with UV light. (C) Fluorescence spectra of the quantum dots as a function of the excitation wavelength.

to the  $\pi-\pi^*$  transition of the GQD.<sup>24</sup> Furthermore, a small absorption peak of unknown origin is seen at 420 nm. The absorption shows a long tail towards larger wavelengths as reported earlier.<sup>13</sup> This may be due to other graphitic particles but is of minor relevance here. The absorbance is a linear function of the GQD concentration, which is characteristic for a homogeneous solution of GQDs without absorption by the solvent itself (see Fig. S4†). The fluorescence spectrum depends, in qualitative agreement with Wu *et al.*, on the excitation wavelength. Absorption around the peak at 340 nm results in strong



fluorescence at approximately 450 nm, while a smaller excitation wavelength generates a second, weaker fluorescence resonance at 380 nm. Absorption around 420 nm induces a fluorescence peak close to 530 nm. The strongest fluorescence around 450 nm results from the  $n-\pi^*$  transition, while the fluorescence at larger wavelengths may be due to groups at the GQD edge containing nitrogen.<sup>26</sup> The quantum yield was calculated to be 17% using quinine sulfate as reference (see inset in Fig. 1B). We note that this is an estimate of the lower bound since the long wavelength tail of the absorbance has been attributed to the GQDs. In general, the relation between the optical spectra and electronic states in GQDs is not yet well understood.<sup>8</sup>

## 2.2 Uptake studies in blood cells from leukapheresis products of normal donors

In a first step we examined the uptake of GQDs into primary human cells obtained from the leukapheresis product (LP) of 3 normal donors who had received granulocyte-colony stimulating factor (G-CSF) to mobilize  $CD34^+$  human progenitor and stem cells (HSCs) into the peripheral blood for allogeneic HSC transplantation. Samples of this kind of LPs are enriched for mononuclear blood cells (MNC) including T and B cells, natural killer cells monocytes and  $CD34^+$  HSCs.<sup>27–29</sup> Still, they also contain a substantial number of granulocytes which are functionally activated as a result of the exposure to G-CSF for at least

4 days.<sup>30</sup> To look for a potentially different uptake of the various white blood cell subpopulations a scatter plot was created based on the expression of the pan leukocyte antigen CD45 and the side scatter properties of the cells defining three gates: (1) lymphoid, (2) monocyte, and (3) granulocyte. Monoclonal antibodies directed against lineage specific antigens were used to differentiate between the lymphoid subpopulations. The gating procedure is shown in Fig. 2A–D. Looking at the samples of the donors we found the usual variation among individuals as far as the composition of the cell types is concerned. Reflecting the mode of collection the major population consists of lymphoid cells with a proportion between 80% and 89%, while the proportion of monocytes is relatively small ranging between 1% and 3%. The number and proportion contained within the samples may also vary depending on the total number of leukocytes induced following the stimulation by G-CSF, with a fraction of granulocytes between 7% and 18% in our series. The median values of leukapheresis products collected for allogeneic HSC transplantation are 60% leukocytes, 28% monocytes and 12% granulocytes. The deviations in the samples under study reflect the typical changes observed after keeping them in cell culture for 36 hours. The majority of lymphoid cells belongs to the  $CD3^+$  T cell fraction with a variable proportion of either  $CD4^+$  T helper or  $CD8^+$  cytotoxic T cells. There is also a considerable number of  $CD19^+$  B cells – varying between 9% and 24% – while the proportion of  $CD56^+$  natural killer cells is relatively small. The

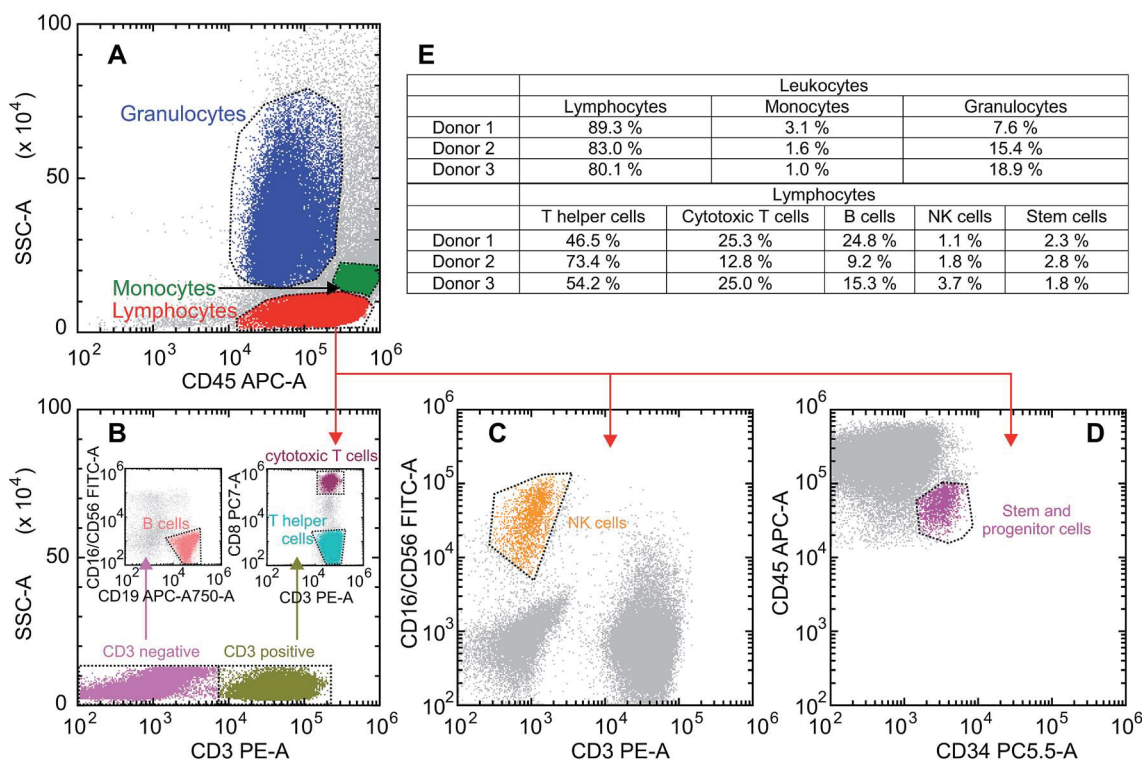


Fig. 2 Gating strategy and composition of the three blood samples: (A) scatter plot of the leukocyte population of donor 2 to differentiate between lymphocytes, monocytes and granulocytes. (B) Discrimination between  $CD3^+$  and  $CD3^{neg}$  lymphocytes to assess  $CD3^{neg}/CD19^+$  B cells (left inset) and  $CD3^+/CD8^+$  cytotoxic T cells as well as  $CD3^{neg}$  T helper cells (right inset). (C) Differentiation of  $CD3^{neg}/CD16^+/CD56^+$  NK cells out of the lymphocyte population. (D) Gating of the  $CD34^+$  stem and progenitor cells. (E) Composition of the three different blood samples.



composition of the three different blood samples is summarized in Fig. 2E. It should be noted that in comparison to “steady-state hematopoiesis” the proportion of CD34<sup>+</sup> cells representing HSCs is greatly enhanced as a consequence of a successful G-CSF induced *in vivo* mobilization.<sup>27</sup> Different from blood samples obtained from normal volunteers during steady-state hematopoiesis, this kind of sample from cytokine-stimulated blood allows us to perform uptake studies in an otherwise extremely rare cell population which is usually residing in the bone marrow requiring a biopsy for sufficient yield.

The donor samples were exposed to GQD solutions with concentrations of 200  $\mu\text{g ml}^{-1}$  as well as 500  $\mu\text{g ml}^{-1}$ , and the uptake was studied as a function of time *via* the fluorescence intensity emitted by the cells. Typical microscopic images of the fluorescent cells are shown in the insets in Fig. 3A–C following an exposure time of 36 hours. As seen previously for adherent cells,<sup>9–12</sup> the GQDs accumulate in the cells without entering the nuclei. Following the uptake microscopically, we noted an increase of the fluorescence intensity over time (see Fig. S5†). For a quantitative analysis, the fluorescence intensity distribution was measured over a period of 36 h for all donor samples in intervals of 2 hours. A representative example for that kind of measurement is given separately for lymphocytes, granulocytes and monocytes in Fig. 3A–C. Starting the incubation at time  $t = 0$  h, the peaks represent the distribution of the

autofluorescence. With time elapsing, the mean value of the intensity increases along with a broadening of the distributions, as illustrated here for an incubation time of 36 h. It is also noted that the time dependence of the intensity distribution is cell-type specific.

These changes of the immunofluorescence distributions as a function of time were recorded for the three donor samples using a GQD concentration of 200  $\mu\text{g ml}^{-1}$  and 500  $\mu\text{g ml}^{-1}$  (see Fig. 3D and E). The mean values of the intensity – with the error bars representing the corresponding standard errors obtained for the three samples – show an approximately linear increase for all three cell types. For all cell types the mean GQD uptake was approximately 2.5-fold greater when the cells were exposed to 500  $\mu\text{g ml}^{-1}$  instead of 200  $\mu\text{g ml}^{-1}$ , while the mean uptake by granulocytes and monocytes is 3.6 and 6.7 times greater compared to lymphocytes, respectively. This implies a cell-specific GQD uptake with a time independent rate  $r$  (given in the figure) which depends linearly on the GQD concentration in solution. Assuming that an incubation period of 36 h – particularly as far as the viability of cells in culture is concerned – at a concentration of 500  $\mu\text{g ml}^{-1}$  might be an optimal condition for the signal strength obtainable from the entire population of leukocytes, a more detailed uptake analysis was performed based on lineage-specific antigens such as CD34 (HSC), CD3 (pan T cell), CD19 (pan B cell), CD56 (natural killer cell). As shown in Fig. 4, similar to the findings made with the

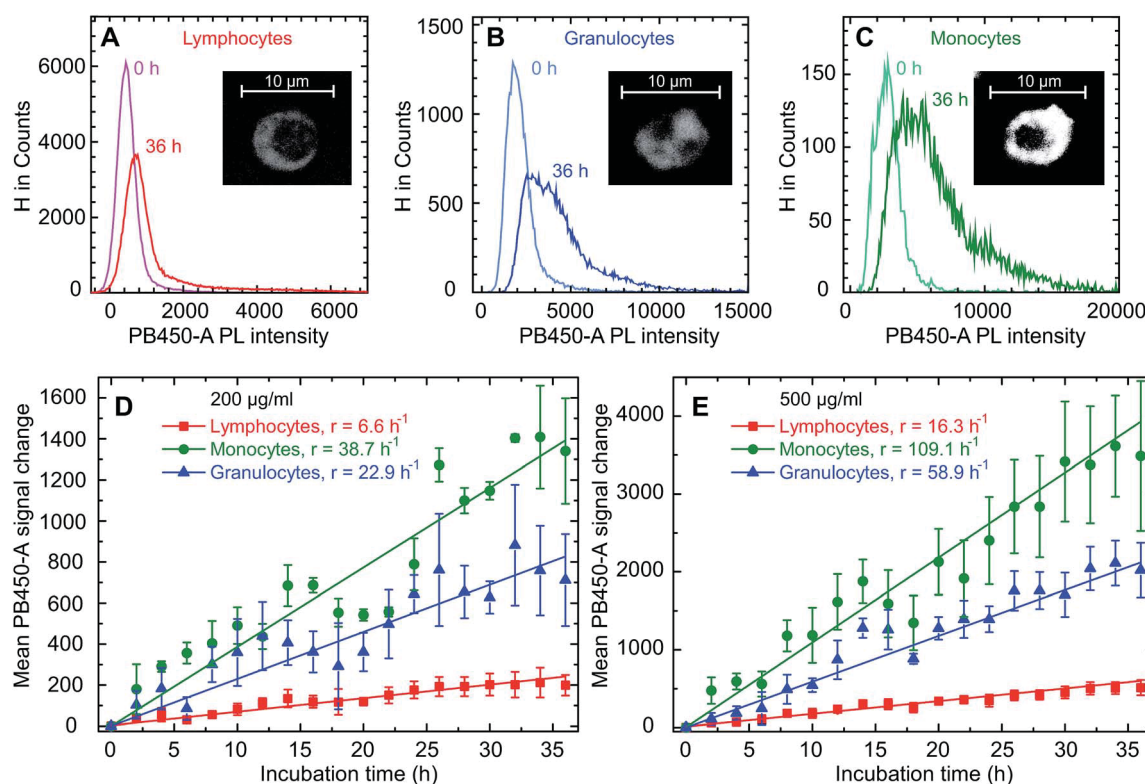


Fig. 3 Changes of the fluorescence intensity histogram in lymphocytes (A), monocytes (B) and granulocytes (C) for donor 2, where the number counts of cells is plotted as a function of the intensity measured in the Cytoflex PB450-A channel following the exposure to GQDs at a concentration of 500  $\mu\text{g ml}^{-1}$ . The insets show typical confocal microscope pictures of the various cell types after 36 h exposure to GQDs. The change of intensity mean values in these three cell types for a GQD concentration of 200  $\mu\text{g ml}^{-1}$  and 500  $\mu\text{g ml}^{-1}$  is shown in (D) and (E). Linear fits were used to determine the uptake rates  $r$  as given in the legend. The error bars represent the standard errors obtained for the three samples.





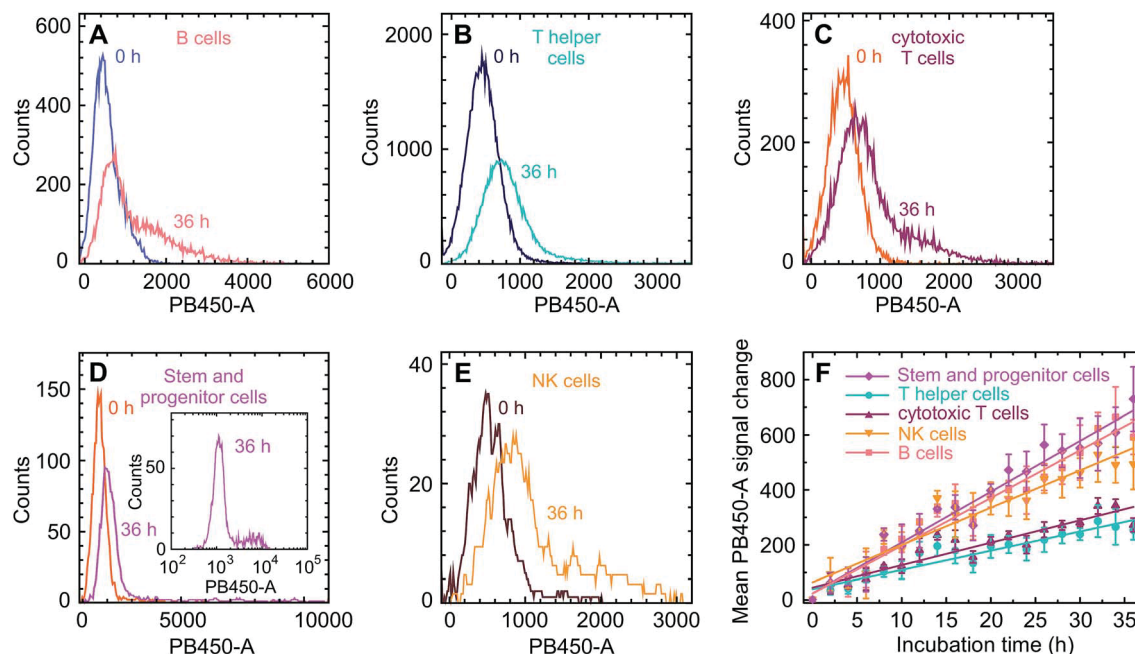


Fig. 4 (A–E) Fluorescence intensity distributions and their changes with incubation time for the five lymphoid subsets under study as seen in the PB 450–A channel, exemplified at samples from donor 2. We note the particularly pronounced tail towards large GQD-induced fluorescence intensities observed in stem and progenitor cells (inset in (D)). (F) Temporal evolution of the ensemble – averaged intensity mean values. The GQD concentration was 500  $\mu\text{g ml}^{-1}$  in all experiments.

leukocytes an uptake of GQDs into the various lymphoid subpopulations was observed which increases linearly with incubation time. Representative examples of the evolution of the intensity distribution as observed for the sample of donor 2 are given for the different subsets. In general, a shift of the mean immunofluorescence intensity distribution towards larger mean values is noted. A greater enhancement was found within CD34<sup>+</sup> cells, NK- and B cells in comparison to the cytotoxic and helper T cells. The combined results observed in our 3 normal donors following the various incubation periods are shown in Fig. 4F. Again as for the leukocytes in total, the mean value of the intensity is specific for each lymphoid subset and increases linearly with time, with rates  $r_{\text{Th}} = 8.3 \text{ h}^{-1}$  for T helper cells,  $r_{\text{CT}} = 9.4 \text{ h}^{-1}$  for cytotoxic T cells,  $r_{\text{NK}} = 17.7 \text{ h}^{-1}$  for NK cells,  $r_{\text{B}} = 20.1 \text{ h}^{-1}$  for B cells and  $r_{\text{stem}} = 22.2 \text{ h}^{-1}$  for stem and progenitor cells.

We proceed with an analysis of the uptake dynamics. Due to the approximately linear dependence of the uptake as a function of both time and GQD concentration in solution  $c_{\text{sol}}$ , its dynamics is qualitatively consistent with a diffusion process, *i.e.* a process driven by a concentration gradient across the cell membrane, which can be described by the diffusion equation  $j = P\Delta c$ , where  $j$  denotes the particle current density into the cell,  $P$  the permeability of the cell membrane for the GQDs and  $\Delta c \equiv c_{\text{sol}} - c_{\text{cell}}$  the difference of the GQD particle concentration between the solution and the intracellular space. The diffusion model allows an order-of-magnitude estimate of  $P$ . For the GQD mass concentration in solution of 500  $\mu\text{g ml}^{-1}$ ,  $c_{\text{sol}}$  can be estimated using the GQD size of approximately 2 nm,<sup>13</sup> an average of two graphene layers per quantum dot and their composition as given on the basis of the XPS analysis to  $4 \times 10^{19}$

$\text{cm}^{-3}$ . By comparing the fluorescence light intensity of the GQD solution and the cells prior to and after the uptake experiments (see Fig. S6†), we find that the  $10^6$  cells per sample take up approximately 0.7% of the GQDs in the solution. This leads to an estimation of the extent of the uptake. After 36 h incubation time, the number of GQDs per cell amounts to  $1.9 \times 10^8$ ,  $6.9 \times 10^8$  and  $1.3 \times 10^9$  for lymphocytes, granulocytes and monocytes, respectively. As can be seen from the fluorescence images in Fig. 3A–C, the particles distribute homogeneously in the cytoplasm but do not enter the nucleus. For the cytoplasm volumes of  $V_{\text{cp}}(\text{L}) = 62 \text{ }\mu\text{m}^3$ ,  $V_{\text{cp}}(\text{G}) = 120 \text{ }\mu\text{m}^3$ ,  $V_{\text{cp}}(\text{M}) = 150 \text{ }\mu\text{m}^3$ ,<sup>31</sup> we find an average distance between the GQDs in the cytoplasm between 5 nm for monocytes and 7 nm for lymphocytes, under the assumption that the cells do not swell due to the uptake. These values illustrate the leukocyte's large capability for GQD incorporation.

Since the fraction of the GQDs entering the cells is quite small, we assume  $\Delta c$  as time-independent, which is in accordance with the fact that no saturation of the uptake is observed. With the presumption that the GQD uptake is proportional to the GQD-induced fluorescence intensity, we obtain particle uptake rates per cell of  $890 \text{ s}^{-1}$  for lymphocytes,  $3190 \text{ s}^{-1}$  for granulocytes and  $5950 \text{ s}^{-1}$  for monocytes. With the reported average cell membrane areas of  $270 \text{ }\mu\text{m}^2$  for lymphocytes,  $300 \text{ }\mu\text{m}^2$  for granulocytes and  $430 \text{ }\mu\text{m}^2$  for monocytes,<sup>31</sup> the GQD influx densities  $j$  are  $\approx 3.3 \text{ }\mu\text{m}^{-2} \text{ s}^{-1}$ ,  $\approx 10.6 \text{ }\mu\text{m}^{-2} \text{ s}^{-1}$ , and  $\approx 13.8 \text{ }\mu\text{m}^{-2} \text{ s}^{-1}$ , corresponding to membrane permeabilities for the GQDs of  $P \approx 8.3 \times 10^{-14} \text{ ms}^{-1}$ ,  $\approx 2.7 \times 10^{-13} \text{ ms}^{-1}$  and  $\approx 3.5 \times 10^{-13} \text{ ms}^{-1}$  for lymphocytes, granulocytes and monocytes, respectively. These permeabilities are plausible values considering that they are significantly smaller than those for



large molecules, like  $P(\text{erythritol}) \approx 6.7 \times 10^{-11} \text{ ms}^{-1}$  (ref. 32) or  $P(\text{glycerol}) \approx 1.6 \times 10^{-9} \text{ ms}^{-1}$ ,<sup>33</sup> since it is well-known that  $P$  decays approximately exponentially as the size of the particle increases.<sup>34</sup> While the permeabilities of the granulocyte and monocyte membranes are comparable, that one of the lymphocytes is a factor of about four smaller. Our results therefore imply that the differences in the uptake rates between lymphocytes and other leukocytes cannot be solely explained by the cell size, even if the relatively large size variation of the monocytes<sup>35</sup> is taken into account. The measurements rather suggest that the uptake mechanisms differ. Electrostatic effects may be considered as an explanation, since it is well-known that the membrane potential influences the uptake of charged particles. While typical zeta potentials of GQDs in aqueous solution of  $-10 \text{ mV}$  to  $-48 \text{ mV}$  have been reported in literature,<sup>13,23</sup> we are not aware of significant differences among the membrane potentials of the various leukocyte subtypes of approximately  $-60 \text{ mV}$ ,<sup>36</sup> and such differences are also not to be expected considering that the cells are not excitable. We therefore discard electrostatic effects as possible explanation. It is, however, notable that the preferential uptake is observed for cell types with a preponderance for phagocytosis, a correlation which may be worth further studies.

As can be seen in Fig. 4, the uptake rates of the lymphocyte subspecies fall into two categories. A faster uptake is observed for stem and progenitor, NK and B cells, while that one of T and T helper cells is relatively slow. To the best of our knowledge, corresponding differences in the cell sizes are not reported. Furthermore, this bimodal behavior does not correlate with the cell's phagocytotic activity, even though B cells are capable of absorbing objects. The distribution of the uptake for the stem and progenitor cells is particularly broad and shows a pronounced, long tail towards large values, see the inset of Fig. 4D. Their relatively large uptake rate may therefore indicate a differentiated hierarchical heterogeneity in relation to the cell evolution. In this context, a recent article of D'Aveni *et al.* is of interest, who describe a particular subset of monocytic CD34<sup>+</sup> cells which are only seen in individuals who had received G-CSF like our normal donors.<sup>29</sup> It is tempting to speculate that the subset of bright CD34<sup>+</sup> cells in our samples could represent that type of monocytic HSC with a more avid uptake of GQDs.

Some further insight regarding the uptake dynamics can be gained by a separate study of the GQD-induced fluorescence intensity distribution  $Q(I)$ . The measured intensity distribution  $H(I)$  is a convolution of the autofluorescence  $A(I)$  and of  $Q(I)$ , expressed by

$$H(I) = \int_0^\infty A(I - J)Q(J)dJ$$

where  $I$  and  $J$  denote the fluorescence intensities. In Fig. 5,  $Q(I)$  as obtained from the measured distributions  $H(I)$  and  $A(I)$  of Fig. 3A–C is shown. It was extracted *via* the convolution theorem which states that  $Q^* = H^*/A^*$ , where  $*$  denotes the Fourier transform of the corresponding distribution, followed by a Fourier back transformation. All cell types show a multi-peaked distribution, which suggests that they contain subpopulations with markedly different GQD uptake rates. Two

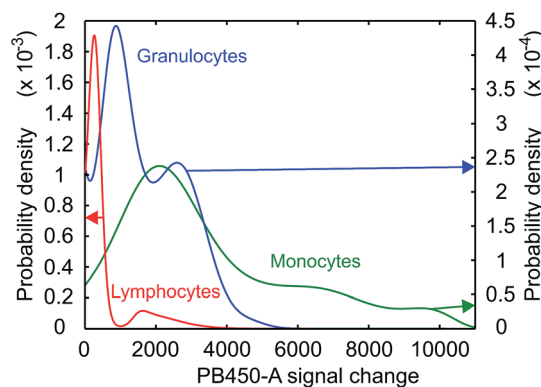


Fig. 5 Probability densities of the GQD – induced fluorescence in lymphocytes, granulocytes and monocytes after 36 h of exposure to a GQD concentration of  $500 \mu\text{g ml}^{-1}$ .

well-separated peaks are observed for the lymphocytes, and it appears self-evident to attribute them to the two subgroups showing small and large uptake rates (see Fig. 4). This could conceptually be checked by summing up the GQD-induced components of the distributions measured for the five lymphoid subsets represented in Fig. 5, but the noise in some of the spectra is too large for a meaningful deconvolution. For the granulocytes and monocytes, the distributions are much broader, containing two and three overlapping peaks, respectively. The possibility of counting two or three cells sticking together as a single cell of correspondingly increased intensity can be safely excluded by the gating procedure. Furthermore, this structure cannot be correlated to cell subpopulations and suggests that other mechanisms exist which determine the GQD uptake rate within one cell type.

Even taking into account a potential decrease of the permeability among the various leukocyte populations during the incubation period this would rather be viewed as a continuous process and therefore does not explain distinct peaks in the uptake rates. As a second possibility, different charge states of the GQDs in solution may be considered, which would result in charge-specific uptake rates. However, since all cells are exposed to the same GQD ensemble, this should lead to a qualitatively identical peak distribution for all three cell types, which is not observed. The reasons for this behavior may be related to different functional states of unidentified character and require further studies. It should be noted that this structure is visible at all exposure times.

### 2.3 Toxicity studies

The question of toxicity was addressed using the XTT viability assay concentrating on the total population of mononuclear cells without particular subset analysis (see Fig. 6). Over the entire period of 36 h covered by 2 h incubation intervals we observed a time- and concentration dependent approximately linear decrease with regard to the proportion of viable cells. The strongest effect was observed during the last 12 h of incubation at a concentration of  $500 \mu\text{g ml}^{-1}$  resulting in a proportion of 90% viable cells in comparison to the untreated controls (see Fig. S7† for the control measurement of all intervals).



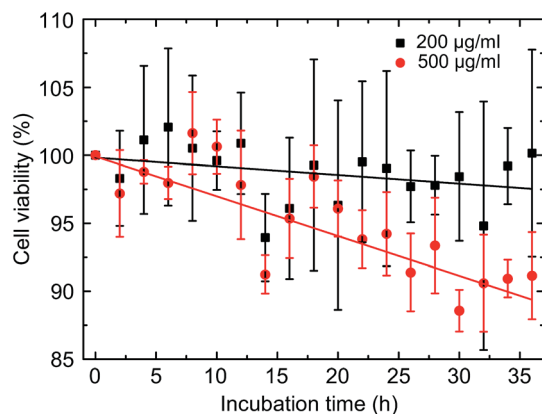


Fig. 6 Viability of the cells as a function of time for the two concentrations.

Putting our findings in the context of the current literature, there are only few studies on the effects of GQDs on blood cells. There is one report showing that large graphitic flakes with diameters in the range of 300 nm to 1 µm cause apoptosis in red blood cells and in macrophages, most likely through generation of intracellular reactive oxygen species (ROS),<sup>37</sup> which is in line with earlier studies on skin fibroblasts.<sup>38</sup> In this study, a GQD-triggered increase of *in vivo* haemolysis has been observed as well. GQDs also induced apoptosis and inflammatory reactions in macrophages following exposure to GQDs. This was accompanied by expression of characteristic response factors such as interleukin-8 or tumor necrosis factor.<sup>39</sup> Interestingly, in an animal model using rats no significant toxicities were observed at different doses up to 10 mg g<sup>-1</sup>.<sup>40</sup> The general cytotoxicity is apparently not influenced by functional groups attached to GQDs.<sup>41</sup> As far as the aspect of toxicity is concerned within our experimental setting, the CD34<sup>+</sup> cells would be of particular interest for further studies, as they represent the stem cell population responsible for the lifelong self-renewal of the hematopoietic system, whereas granulocytes and monocytes have a half live of only a few hours, thus representing target cells of immediate and not long time toxicity.

### 3 Conclusions

In our studies we assessed the new generation of quantum dots based on graphene with regard to their uptake properties into primary human blood cells consisting of a broad spectrum of leukocyte subsets which include the rare population of CD34<sup>+</sup> hematopoietic stem and progenitor cells. The *in vitro* exposure resulted in a time- and concentration dependent cellular uptake leading to significant intracellular concentrations of quantum dots without undue toxicity. We found that the uptake rate in granulocytes and monocytes is significantly greater as compared to lymphocytes, a difference that cannot solely be explained by the variations in cell size alone but rather implies an intrinsic difference of the effective cell membrane permeabilities. As the leukocytes of the same species show multi-peaked uptake rates we suggest that some functional diversity among the subsets

exists which requires further assessment. The open questions in mind we consider these readily available GQDs as promising compounds for *in vivo* and *in vitro* cell tracking studies as well as low weight carriers for different molecules such as mRNA for *in vitro* vaccination CD34<sup>+</sup> cell derived dendritic cells.

## 4 Experimental section

### 4.1 Materials

Citric acid (ACS reagent, ≥99.5%), dicyandiamide (99%), Fetal Bovine Serum (FBS), Iscove's Modified Dulbecco's Medium (IMDM), L-glutamine–penicillin–streptomycin solution, Dulbecco's Phosphate Buffered Saline (PBS) and the Cell Proliferation Kit II (XTT) were purchased from Sigma Aldrich. Float-A-Lyzer dialysis devices (100–500 Da and 20 kDa) and sterile filters (200 nm) were obtained from VWR and antibodies against CD45-APC, CD16/CD56-FITC, CD3-PE, CD34-PerCP-Cy5.5, CD8-PE-Cy7 and CD19-APC-H7 were purchased from BD biosciences.

### 4.2 Synthesis of graphene quantum dots (GQDs)

Fluorescent GQDs were synthesized according to the method of Wu *et al.*<sup>13</sup> with slight modifications. 70 mg citric acid and 250 mg dicyandiamide were dissolved in 4 ml DI water and heated to 180 °C on a hot plate for 3 h under continuous stirring in a 10 ml stainless steel autoclave. The obtained aqueous solution was centrifuged with an Eppendorf MiniSpin® at 13 400 rpm for 15 minutes to remove insoluble residual. Citric acid and dicyandiamide waste were removed by dialyzing 10 ml of GQD solution against 2 l of DI water for 48 h with one water exchange after 24 h using a 100–500 Da dialysis membrane. Afterwards larger particles were filtered out with a 20 kDa membrane. Finally, the GQDs were dried and weighed using a Sartorius A 200S electronic analytical balance.

### 4.3 Characterization of GQDs

Photoluminescence properties were measured using a Horiba FluoroMax®-4 spectrofluorometer and absorbance spectra were taken with an Agilent Cary 4000 spectrophotometer. The quantum yield (QY) was obtained using quinine sulfate (QS) dissolved in 0.5 M H<sub>2</sub>SO<sub>4</sub> as reference (QY<sub>QS</sub> = 54%). The concentrations 3 µg ml<sup>-1</sup>, 6 µg ml<sup>-1</sup> and 12 µg ml<sup>-1</sup> of OS and of the GQDs were excited at a wavelength of 346 nm and 360 nm, respectively. The integrated fluorescence intensities were plotted vs. the corresponding absorbance values from which the slopes were determined. The quantum yield was calculated using  $QY_{GQDs} = QY_{QS} \times \frac{m_{GQDs} \eta_{GQDs}^2}{m_{QS} \eta_{QS}^2}$  where  $m$  is the slope and  $\eta$  the refractive index of the solvent. Confocal fluorescence microscopy was performed on a Zeiss LSM710 laser scanning system and AFM measurements were executed using the tapping mode of a Veeco 3100 with SiO<sub>2</sub> as substrate. XPS data were collected on a PHI 5000 Versaprobe II XPS microprobe instrument using Au as substrate and TEM images were taken with the Titan G3 50-300 PICO<sup>42</sup> on amorphous carbon TEM grids.





#### 4.4 Collection of leukapheresis derived blood samples from normal donors

The primary human cells for our study were obtained from leukapheresis products (LP) of three normal individuals who served as HLA-identical donors for an allogeneic blood stem cell transplantation (SCT) in patients with hematological malignancies. For the purpose of blood stem cell collection, the normal donors had received granulocyte colony stimulating factor (G-CSF) at the usual dose of 480  $\mu\text{g}$  per day over a time period of 4 to 5 days in order to increase the number of circulating human progenitor and stem cells (HSC) – as defined by the expression of CD34 on the cell surface – in the peripheral blood for allogeneic HSC transplantation. On average, the treatment with G-CSF in normal individuals leads to a 100-fold increase in the concentration of CD34<sup>+</sup> blood stem cells in comparison to steady-state hematopoiesis. Samples of this kind of LPs are enriched for mononuclear blood cells (MNC) including T and B cells, natural killer cells monocytes and CD34<sup>+</sup> HSC. In that respect, the samples that we used for our experiments are unique with regard to their content of early hematopoietic stem and progenitor cells. Still, they also contain a substantial number of granulocytes which are functionally activated as they had been exposed to G-CSF for at least 4 days.

#### 4.5 Cell preparation

Blood samples from leukapheresis products of three healthy donors were used for the *in vitro* studies. From each of them a sample of 1 ml was obtained and lysed two times using 50 ml ammonium chloride to remove erythrocytes. The remaining leukocytes were resuspended in Iscove's Minimal Dulbecco Medium (IMDM) containing 20% Fetal Bovine Serum (FBS) and 1% L-glutamine–penicillin–streptomycin solution and cultivated in a Heracell TM 150i incubator in a humidified atmosphere at 5% CO<sub>2</sub> and 37 °C. 500  $\mu\text{l}$  per well of cell suspension were dispensed in 24 well plates at a final concentration of  $2 \times 10^6$  cells per ml.

#### 4.6 Cell cultivation for GQD uptake studies

GQDs were dissolved in cell culture medium at concentrations of 1.2 mg ml<sup>-1</sup> and 3.0 mg ml<sup>-1</sup> and the obtained solutions were sterile filtered. From the beginning of the cultivation period – termed as time point 0–100  $\mu\text{l}$  of the GQD solutions were added in 2 h intervals into the wells to achieve GQD concentrations of 200  $\mu\text{g}$  ml<sup>-1</sup> and 500  $\mu\text{g}$  ml<sup>-1</sup>. The cultivation was stopped after 36 hours. As a result, uptake measurements for a total of 18 different incubation periods are available. In parallel, the same amount of sterile filtered cell culture medium without containing GQDs was added to the wells serving as control. After 36 hours all samples were washed two times with PBS (centrifugation for 5 minutes at 470g) and stained with antibodies as detailed below.

#### 4.7 Immunocytological characterization of blood-derived mononuclear cells

To look for a potentially different uptake of the various MNC subpopulation monoclonal antibodies directed against lineage-

and differentiation specific antigens, *i.e.* CD45-APC, CD16/CD56-FITC, CD3-PE, CD34-PerCP-Cy5.5, CD8-PE-Cy7 and CD19-APC-H7 were used. The cells were incubated for 15 minutes with 5  $\mu\text{l}$  of each antibody per sample and fixed with 150  $\mu\text{l}$  4% formaldehyde solution, before the cells were transferred to a 96 well plate for flow cytometry analysis. Debris was removed by gating the living cells in a forward *vs.* sideward scatter plot (FSC *vs.* SSC). Out of all living cells, gates were set individually for each sample, in a CD45 *vs.* SSC plot to assess lymphocytes, monocytes and granulocytes as established in immune-phenotyping of leukemia<sup>43</sup> and the analysis of human bone marrow specimens.<sup>44</sup> To distinguish between lymphocyte subpopulations, CD3<sup>+</sup> and CD3<sup>neg</sup> cells were gated in a SSC *vs.* CD3 plot. NK cells (CD3<sup>neg</sup>/CD16<sup>+</sup>/CD56<sup>+</sup>) were gated out of the lymphocyte population in a CD3 *vs.* CD16/CD56 plot and B-cells (CD3<sup>neg</sup>/CD16<sup>neg</sup>/CD56<sup>neg</sup>/CD19<sup>+</sup>) were gated out of the CD3 negative cells in a CD16/CD56 *vs.* CD19 plot. Cytotoxic T cells (CD3<sup>+</sup>/CD8<sup>+</sup>) and T helper cells (CD3<sup>+</sup>/CD8<sup>neg</sup>) were differentiated out of the CD3<sup>+</sup> population in a CD3 *vs.* CD8 plot. Finally, stem and progenitor cells (CD45<sup>+</sup>/CD34<sup>+</sup>) were assessed with a CD34 *vs.* CD45 plot. The gating strategy is shown in Fig. 2. Information regarding the occurrence of NK cells, cytotoxic T cells, T helper cells, B-cells and stem and progenitor cells is given in relation to the lymphocyte population out of the CD45/SSC plot, whereas the occurrence of lymphocytes, monocytes and granulocytes is given with respect to the whole leukocyte population, *i.e.*, the sum of lymphocytes, monocytes and granulocytes out of the CD45/SSC plot. FACS analysis was performed using a Beckmann Coulter CytoFLEX flow cytometer with an automatic 96-well-plate loader. The FACS is equipped with a 488 nm and a 638 nm laser beam, measuring the antibody-coupled fluorescence dyes in the APC, PE, PC5.5, APC-A750, PC7 and FITC channels and a laser beam with an excitation wavelength of 405 nm, measuring the GQD induced fluorescence in the PB450 channel. For each sample at least 100 000 events were recorded permitting a statistically valid evaluation with a minimum of at least 1000 cellular events per sample and cell type. The mean fluorescence intensity recorded for a particularly labeled blood cell was subtracted by the respective autofluorescence observed in the control and the resulting “true fluorescence activity” taken as the parameter reflecting the cellular uptake of GQDs. The analysis was carried out using the Beckmann Coulter CytExpert software.

#### 4.8 Cell viability

Cell viability was determined by the standard XTT assay. Briefly, 100  $\mu\text{l}$  per well of cell suspension with a final concentration of  $2 \times 10^6$  cells per ml were dispensed in 96 well plates. The cells were treated with 20  $\mu\text{l}$  of sterile filtered GQD containing cell culture medium for each concentration and with sterile filtered pure cell culture medium for the controls. 60  $\mu\text{l}$  XTT labeling solution was added and incubated for 4 h before the absorbance at 490 nm was measured with an ELISA microplate reader.

#### 4.9 Ethical statement

All experiments were performed in compliance with the relevant laws and institutional guidelines and have been approved by the



ethical committee of the Heinrich Heine University (No. 3240 from August/October 2009). All donors had given their informed consent according to the guidelines of the ethical committee specified above.

## Acknowledgements

The first author acknowledges financial support of his position by the Düsseldorf School of Oncology (DSO). T. H. acknowledges support by the Betz foundation. Support regarding the XPS analysis by A. Besmehn and H. Hartmann (FZ Jülich), as well as access to the confocal microscope at the Center of Advanced imaging (CAi) of HHU Düsseldorf, is gratefully acknowledged. The authors thank S. Wesselborg for his advice regarding the toxicity studies.

## References

- 1 J. K. Jaiswal, H. Mattoussi, J. M. Mauro and S. M. Simon, *Nat. Biotechnol.*, 2002, **21**, 47–51.
- 2 X. Michalet, F. F. Pinaud, L. A. Bentolila, J. M. Tsay, S. Doose, J. J. Li, G. Sundaresan, A. M. Wu, S. S. Gambhir and S. Weiss, *Science*, 2005, **307**, 538.
- 3 B. A. Kairdolf, A. M. Smith, T. H. Stokes, M. D. Wang, A. N. Young and S. Nie, *Annu. Rev. Anal. Chem.*, 2013, **6**, 143.
- 4 A. M. Smith, S. Dave, S. Nie, L. True and X. H. Gao, *Expert Rev. Mol. Diagn.*, 2006, **6**, 231–244.
- 5 V. Bagalkot, L. Zhang, E. Levy-Nissenbaum, S. Jon, P. W. Kantoff, R. Langer and O. C. Farokhzad, *Nano Lett.*, 2007, **7**, 3065.
- 6 X. Gao, Y. Cui, R. M. Levenson, L. W. K. Chung and S. Nie, *Nat. Biotechnol.*, 2004, **22**, 969.
- 7 S. N. Baker and G. A. Baker, *Angew. Chem., Int. Ed.*, 2010, **49**, 6726.
- 8 H. Li, Z. Kang, Y. Liu and S.-T. Lee, *J. Mater. Chem.*, 2012, **22**, 24230.
- 9 L. Cao, X. Wang, M. J. Meziani, F. Lu, H. Wang, P. G. Luo, Y. Lin, B. A. Harruff, L. M. Veca, D. Murray, S. Xie and Y. Sun, *J. Am. Chem. Soc.*, 2007, **129**, 11318.
- 10 C. Liu, P. Zhang, F. Tian, W. Li, F. Li and W. Liu, *J. Mater. Chem.*, 2011, **21**, 13163.
- 11 S. Zhu, J. Zhang, C. Qiao, S. Tang, Y. Li, W. Yuan, B. Li, L. Tian, F. Liu, H. Gao, H. Wei, H. Zhang, H. Sun and B. Yang, *Chem. Commun.*, 2011, **47**, 6858.
- 12 W. Shang, X. Zhang, M. Zhang, Z. Fang, Y. Sun, M. Han and L. Fan, *Nanoscale*, 2014, **6**, 5799.
- 13 Z. L. Wu, M. X. Gao, T. T. Wang, X. Y. Wan, L. L. Zheng and C. Z. Huang, *Nanoscale*, 2014, **6**, 3868.
- 14 A. Roos and W. F. Boron, *Physiol. Rev.*, 1981, **61**, 296–434.
- 15 X. Huang, F. Zhang, L. Zhu, K. Y. Choi, N. Guo, J. Guo, K. Tackett, P. Anilkumar, G. Liu, Q. Quan, H. S. Choi, G. Niu, Y.-P. Sun, S. Lee and X. Chen, *ACS Nano*, 2013, **7**, 5684.
- 16 M. Zheng, S. Ruan, S. Liu, T. Sun, D. Qu, H. Zhao, Z. Xie, H. Gao, X. Jing and Z. Sun, *ACS Nano*, 2015, **9**, 11455.
- 17 X. Sui, C. Luo, C. Wang, F. Zhang, J. Zhang and S. Guo, *Nanomedicine*, 2016, **12**, 1997.
- 18 X. Gong, Q. Zhang, Y. Gao, S. Shuang, M. M. F. Choi and C. Dong, *ACS Appl. Mater. Interfaces*, 2016, **8**, 11288.
- 19 M. Kryuchkova, A. Danilushkina and R. F. Y. Lvov, *Environ. Sci.: Nano*, 2016, **3**, 442–452.
- 20 X. Guo and N. Mei, *J. Food Drug Anal.*, 2014, **22**, 105–115.
- 21 Y. Dong, J. Shao, C. Chen, H. Li, R. Wang, Y. Chi, X. Lin and G. Chen, *Carbon*, 2012, **50**, 4738.
- 22 D. Graf, F. Molitor, K. Ensslin, C. Stampfer, A. Jungen, C. Hierold and L. Wirtz, *Nano Lett.*, 2007, **7**, 238.
- 23 M. Zhang, L. Bai, W. Shang, W. Xie, H. Ma, Y. Fu, D. Fang, H. Sun, L. Fan, M. Han, C. Liub and S. Yang, *J. Mater. Chem.*, 2012, **22**, 7461.
- 24 F. Liu, M.-H. Jang, H. D. Ha, J.-H. Kim, Y.-H. Cho and T. S. Seo, *Adv. Mater.*, 2013, **25**, 3657.
- 25 G. Eda, Y.-Y. Lin, C. Mattevi, H. Yamaguchi, H.-A. Chen, I. S. Chen, C.-W. Chen and M. Chhowalla, *Adv. Mater.*, 2010, **22**, 505.
- 26 D. Qu, M. Zheng, J. Li, Z. Xie and Z. Sun, *Light: Sci. Appl.*, 2015, **4**, e364.
- 27 R. Möhle, M. Pförsich, S. Fruehauf, B. Witt, A. Krämer and R. Haas, *Bone Marrow Transplant.*, 1994, **14**, 827.
- 28 K. Theilgaard-Mönch, K. Raaschou-Jensen, H. Palm, K. Schødt, C. Heilmann, L. Vindeløv, N. Jacobsen and E. Dickmeiss, *Bone Marrow Transplant.*, 2001, **28**, 1073.
- 29 M. D'Aveni, J. Rossignol, T. Coman, S. Sivakumaran, S. Henderson, T. Manzo, P. S. E. Sousa, J. Bruneau, G. Fouquet, F. Zavala, O. Alegria-Prvot, M. Garfa-Traor, F. Suarez, H. Trebeden-Ngre, M. Mohty, C. L. Bennett, R. Chakraverty, O. Hermine and M. T. Rubio, *Sci. Transl. Med.*, 2015, **7**, 281ra42.
- 30 S. Murea, S. Fruehauf, W. J. Zeller and R. Haas, *J. Hematother.*, 1996, **5**, 351.
- 31 G. W. Schmid-Schönbein, *Cell Biophys.*, 1990, **17**, 107.
- 32 J. O. Wieth, *J. Physiol.*, 1971, **213**, 435.
- 33 A. Carlsen and J. O. Wieth, *Acta Physiol. Scand.*, 1976, **97**, 501.
- 34 W. D. Stein, *Transport and Diffusion across Cell Membranes*, Academic Press, London, 1985.
- 35 G. W. Schmid-Schönbein, Y. Y. Shih and S. Chien, *Blood*, 1980, **56**, 866.
- 36 E. K. Gallin, *Physiol. Rev.*, 1991, **71**, 775.
- 37 G. Qu, X. Wang, Z. Wang, S. Liu and G. Jiang, *Nanoscale Res. Lett.*, 2013, **8**, 198.
- 38 K. H. Liao, Y. S. Lin, C. W. Macosko and C. L. Haynes, *ACS Appl. Mater. Interfaces*, 2011, **3**, 2607.
- 39 Y. Qin, Z.-W. Zhou, S.-T. Pan, Z.-X. He, X. Zhang, J.-X. Qiu, W. Duan, T. Yang and S.-F. Zhou, *Toxicology*, 2015, **327**, 62.
- 40 M. Nurunnabi, Z. Khatun, K. M. Huh, S. Y. Park, D. Y. Lee, K. J. Cho and Y. Lee, *ACS Nano*, 2013, **7**, 6858–6867.
- 41 X. Yuan, Z. Liu, Z. Guo, Y. Ji, M. Jin and X. Wang, *Nanoscale Res. Lett.*, 2014, **9**, 108.
- 42 J. Barthel, L. Houben and K. Tillmann, *Journal of large scale research facilities*, 2015, **1**, 57.
- 43 F. Lacombe, L. Lacoste, A. Briais, P. Dumain, F. Belloc, J. Reiffers and P. Bernard, *Blood*, 1997, **90**, 2895.
- 44 G. T. Stelzer, K. E. Shults and M. R. Loken, *Ann. N. Y. Acad. Sci.*, 1993, **677**, 265.





# Supporting information for: Uptake dynamics of graphene quantum dots into primary human blood cells following in vitro exposure

S. Fasbender,<sup>†</sup> S. Allani,<sup>†</sup> C. Wimmenauer,<sup>†</sup> R.-P. Cadeddu,<sup>‡</sup> K. Raba,<sup>¶</sup> J. C.  
Fischer,<sup>¶</sup> Bekir Bulat,<sup>§</sup> Claus A. M. Seidel,<sup>§</sup> Martina Luysberg,<sup>||</sup> T. Heinzl,<sup>\*,†</sup> and  
R. Haas<sup>\*,‡</sup>

<sup>†</sup>*Condensed Matter Physics Laboratory, Heinrich-Heine-University, D-40204 Düsseldorf,  
Germany*

<sup>‡</sup>*Department of Haematology, Oncology and Clinical Immunology,  
Heinrich-Heine-University, D-40204 Düsseldorf, Germany*

<sup>¶</sup>*Institute for Transplantation Diagnostics and Cell Therapeutics,  
Heinrich-Heine-University, D-40204 Düsseldorf, Germany*

<sup>§</sup>*Institute of Molecular Physical Chemistry, Heinrich-Heine-University, D-40204  
Düsseldorf, Germany*

<sup>||</sup>*Ernst Ruska-Centre, Jülich Research Centre, 52425 Jülich, Germany*

E-mail: thomas.heinzel@hhu.de; Haas.med.uni-duesseldorf.de

## Abstract

The supporting information provides further data regarding the characterization of the graphene quantum dots and the fluorescence measurements used to quantify the uptake of the quantum dots by the cells.

# Keywords

Graphene Quantum Dots, Leukocytes, Nanoparticles, Fluorescence spectroscopy, Toxicity

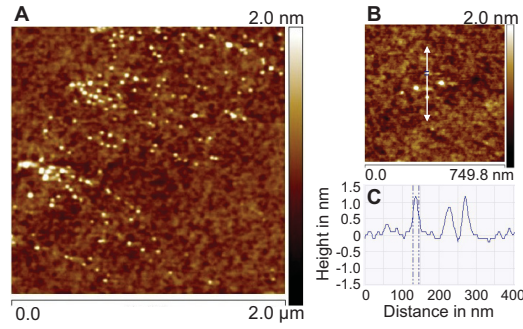


Figure S 1: The GQDs deposited on SiO<sub>2</sub> as seen by an atomic force microscope. Their apparent width is  $\approx 20$  nm, which is much larger than their true width, in accordance with earlier works. The height of less than 1 nm indicates single-layer graphene.

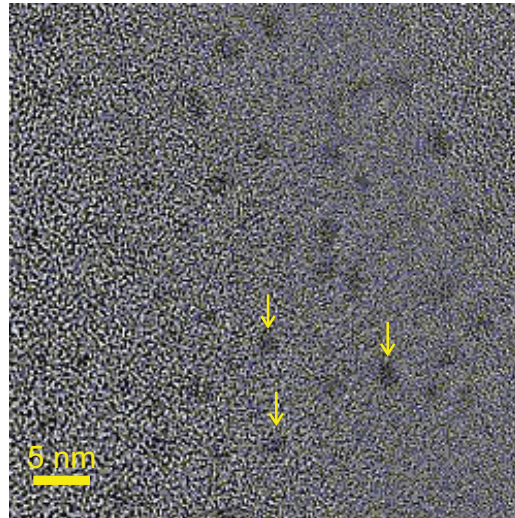


Figure S 2: Transmission electron microscope picture of the graphene quantum dots used in the experiment. The quantum dots appear as full, dark circles on top of the substrate, an amorphous carbon grid of 5 nm thickness. Some of the dots are marked by an arrow.

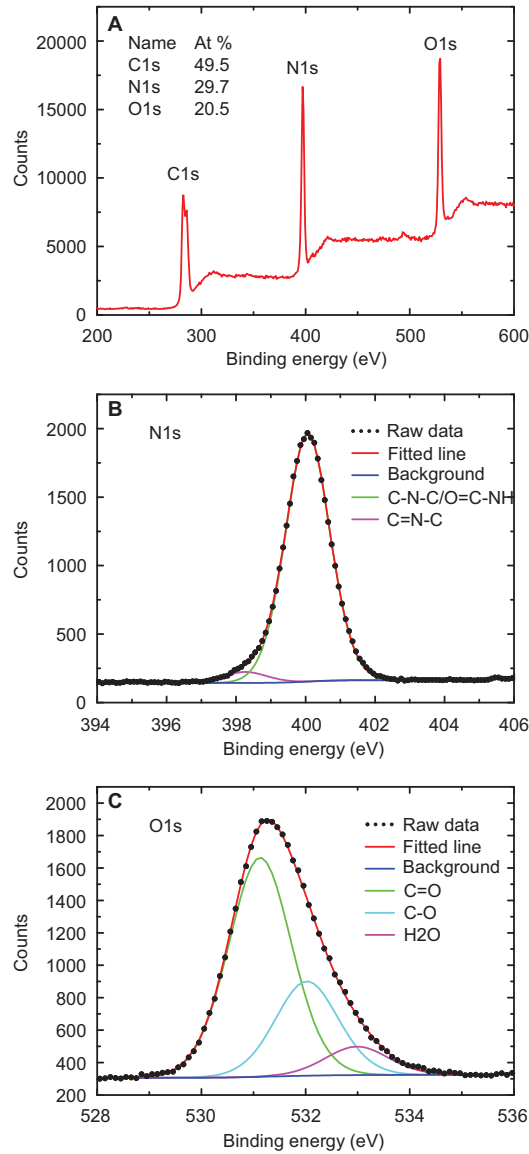


Figure S 3: (A) Overview of the XPS spectrum of the GQDs. the three dominant peaks are due to the electrons excited from the 1s states of the carbon, nitrogen and oxygen atoms, respectively. The fine structures of the N1s- and O1s- resonances are shown in (B) and (C), respectively. Their best fit analysis is in qualitative agreement with that one of the C1s - peak discussed in the main text. In particular, the absence of nitrogen-oxygen bonds is remarkable.

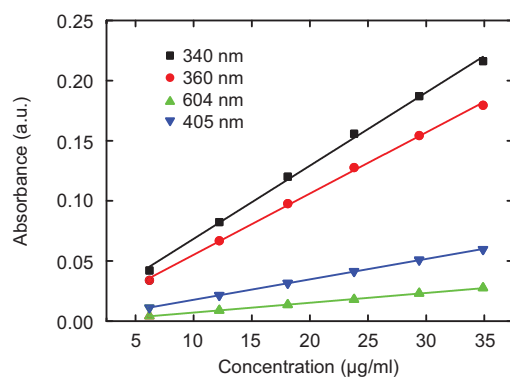


Figure S 4: The dependence of the absorbance of the GQD solutions depends linearly on the GQD concentration and implies that the absorbance of the solvent is negligible.

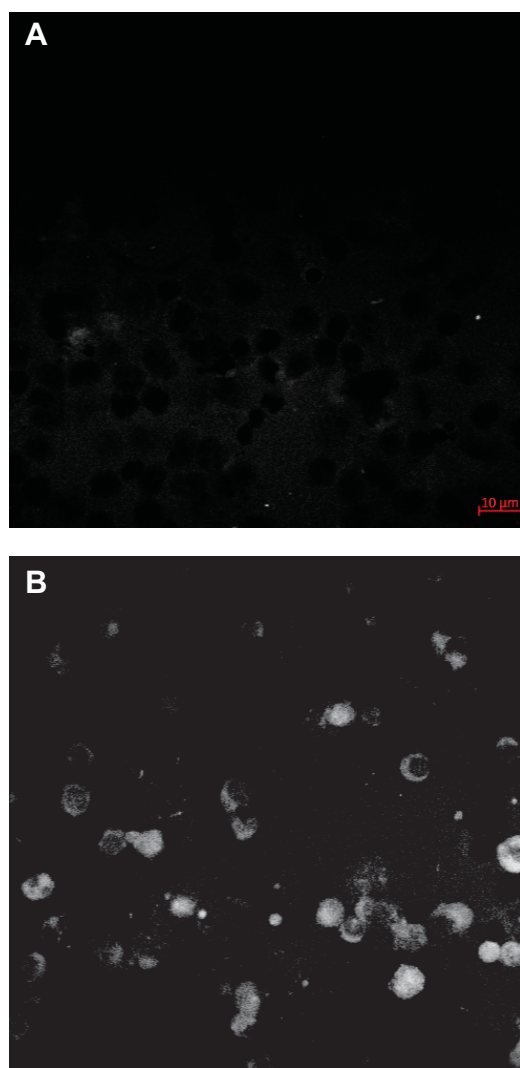


Figure S 5: Fluorescence intensity of the cells prior to (upper part) and after exposure to GQDs for 36 hours (lower part), as observed in a confocal optical microscope. Before the exposure to GQDs, the cells appear as dark with respect to a slightly fluorescent environment. After the exposure, the GQD - induced fluorescence inside the cells dominates the picture. All microscope parameters are identical, such that the comparison of the intensities by eye can be taken as a qualitative measure of the uptake.

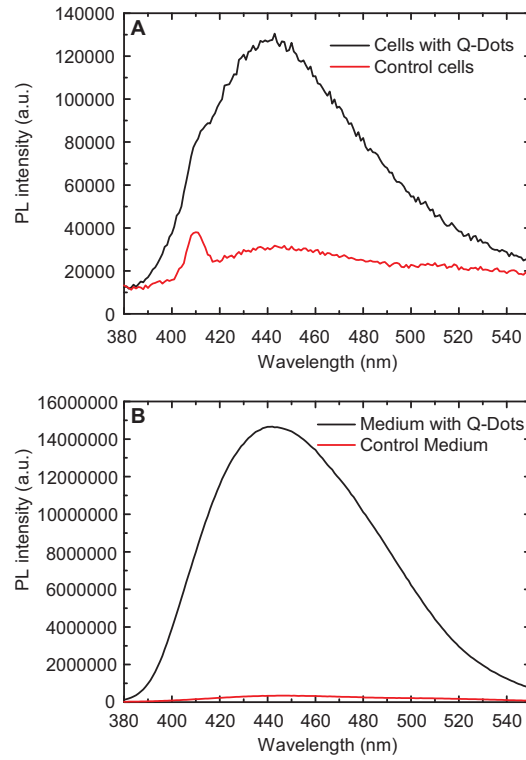


Figure S 6: Fluorescence spectrum of the GQDs in the cells (A) in comparison to that one obtained for the solution prior to the addition of the cells (B). After the Raman peak at a wavelength of 410nm has been removed, the ratio of the integrated intensities, corrected by the intensity of the control, corresponds to the fraction of the absorbed GQDs.

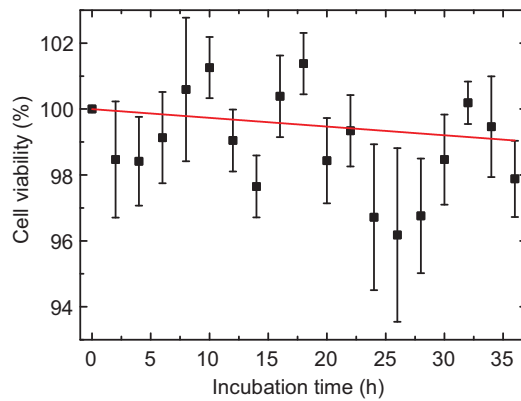


Figure S 7: Control experiment of the cell viability in the culture medium, as specified in the experimental Section (paragraph on cell preparation), in the absence of GQDs.

---

# From *in vitro* to *ex vivo*: Subcellular localization and uptake of graphene quantum dots into solid tumors

## Reference

D. Kersting, S. Fasbender, R. Pilch, J. Kurth, A. Franken, M. Ludescher, J. Naskou, A. Hallenberger, C. von Gall, C. J. Mohr, R. Lukowski, K. Raba, S. Jaschinski, I. Esposito, J. C. Fischer, T. Fehm, D. Niederacher, H. Neubauer and T. Heinzl, *Nanotechnology* **30**, 395101 (2019), Published by IOPscience.  
<https://doi.org/10.1088/1361-6528/ab2cb4>

## Copyright statement

Original content from this work may be used under the terms of the Creative Commons Attribution 3.0 licence. Any further distribution of this work must maintain attribution to the author(s) and the title of the work, journal citation and DOI.

## Contributions

I planned the experiments. I participated in the conductance of parts of the experiments and contributed to manuscript writing.

PAPER • OPEN ACCESS

# From *in vitro* to *ex vivo*: subcellular localization and uptake of graphene quantum dots into solid tumors

To cite this article: David Kersting *et al* 2019 *Nanotechnology* **30** 395101

View the [article online](#) for updates and enhancements.

## Recent citations

- [Time-Resolved Quantification of Nanoparticle Uptake, Distribution, and Impact in Precision-Cut Liver Slices](#)  
Roberta Bartucci *et al*



**IOP | ebooks™**

Bringing you innovative digital publishing with leading voices to create your essential collection of books in STEM research.

Start exploring the collection - download the first chapter of every title for free.



# From *in vitro* to *ex vivo*: subcellular localization and uptake of graphene quantum dots into solid tumors

David Kersting<sup>1</sup>, Stefan Fasbender<sup>1</sup> , Rabea Pilch<sup>1</sup>, Jennifer Kurth<sup>1</sup>, André Franken<sup>2</sup>, Marina Ludescher<sup>2</sup>, Johanna Naskou<sup>2</sup>, Angelika Hallenberger<sup>3</sup>, Charlotte von Gall<sup>3</sup>, Corinna J Mohr<sup>4</sup>, Robert Lukowski<sup>4</sup>, Katharina Raba<sup>5</sup>, Sandra Jaschinski<sup>6</sup>, Irene Esposito<sup>6</sup>, Johannes C Fischer<sup>5</sup>, Tanja Fehm<sup>2</sup>, Dieter Niederacher<sup>2</sup>, Hans Neubauer<sup>2</sup> and Thomas Heinzl<sup>1</sup> 

<sup>1</sup> Condensed Matter Physics Laboratory, Heinrich-Heine-University, D-40204 Düsseldorf, Germany

<sup>2</sup> Department of Obstetrics and Gynecology, University Hospital and Medical Faculty, Heinrich-Heine-University, D-40204 Düsseldorf, Germany

<sup>3</sup> Institute for Anatomy II, Medical Faculty, Heinrich-Heine-University, D-40204 Düsseldorf, Germany

<sup>4</sup> Institute of Pharmacy, Department of Pharmacology, Toxicology and Clinical Pharmacy, University of Tübingen, D-72076 Tübingen, Germany

<sup>5</sup> Institute for Transplantation Diagnostics and Cell Therapeutics, Heinrich-Heine-University, D-40204 Düsseldorf, Germany

<sup>6</sup> Institute of Pathology, University Hospital and Medical Faculty, Heinrich-Heine-University, D-40204 Düsseldorf, Germany

E-mail: [Thomas.Heinzl@hhu.de](mailto:Thomas.Heinzl@hhu.de)

Received 25 March 2019, revised 20 May 2019

Accepted for publication 25 June 2019

Published 15 July 2019



## Abstract

Among various nanoparticles tested for pharmacological applications over the recent years, graphene quantum dots (GQDs) seem to be promising candidates for the construction of drug delivery systems due to their superior biophysical and biochemical properties. The subcellular fate of incorporated nanomaterial is decisive for transporting pharmaceuticals into target cells. Therefore a detailed characterization of the uptake of GQDs into different breast cancer models was performed. The demonstrated accumulation inside the endolysosomal system might be the reason for the particles' low toxicity, but has to be overcome for cytosolic or nuclear drug delivery. Furthermore, the penetration of GQDs into precision-cut mammary tumor slices was studied. These constitute a far closer to reality model system than monoclonal cell lines. The constant uptake into the depth of the tissue slices underlines the systems' potential for drug delivery into solid tumors.

Supplementary material for this article is available [online](#)

Keywords: graphene quantum dots, drug delivery, intracellular localization, cellular uptake, tissue slices

(Some figures may appear in colour only in the online journal)

## 1. Background

Nanoparticle based drug delivery systems have gained a lot of research interest due to their ability to control the release of



Original content from this work may be used under the terms of the [Creative Commons Attribution 3.0 licence](#). Any further distribution of this work must maintain attribution to the author(s) and the title of the work, journal citation and DOI.

drugs and improve their selectivity and potency [1]. Possible applications range from tuberculosis [2] and inflammation [3] to cancer [4], where nanoparticle based drug delivery systems have the potential to overcome platinum treatment resistance [5]. Recently, a liposomal nanoparticle formulation of cytarabine and daunorubicin showed impressive clinical benefit in AML patients with subsequent FDA approval [6].

Among the nanomaterial platforms already established in research are liposomes, carbon nanotubes, gold nanoparticles, dendrimers, polymeric nanoparticles and superparamagnetic iron oxides [7]. Graphene quantum dots (GQDs) present a promising next generation nanomaterial due to their extremely large surface to mass ratio. They consist of one or few layers of graphene and emit strong fluorescence due to quantum confinement and edge effects [8, 9]. As GQDs enter the cytoplasm of various cell types *in vitro* without significant toxicity [10–12], they are used in biomedical research not only for drug delivery applications, but also for long term and deep tissue imaging, cancer diagnostics and intracellular sensing [13–16]. Regarding drug delivery, it has been shown that GQDs improve the anti-cancer activity of cisplatin [17] and doxorubicin [18, 19], while it is possible to monitor the release of doxorubicin due to their fluorescence properties [20]. For the use of GQDs as a carrier of anti-cancer drugs a detailed knowledge about their subcellular localization, their differential uptake into different tumor models and their penetration into the depth of solid tumor tissues is vital.

Breast cancer represents the most common cancer among women worldwide [21] and incident rates are still predicted to increase [22]—a reason for the unaltered urgent demand for new therapeutic concepts. Breast cancer cell lines are commonly applied as easy-to-use laboratory model systems, but may display geno- and phenotypic changes from the original tissue due to longstanding *in vitro* cultivation [23]. Moreover monoclonal cell lines can hardly depict the heterogeneity presented by the human breast cancer disease [24].

In contrast, *ex vivo* cultivated precision-cut tissue slices (PCTS) of defined thickness contain all cell types of an organ and therefore allow to examine multicellular biochemical processes like metabolism, bio-transformation and transport of drugs in a nearly natural environment [25]. Possible applications regarding tumor tissue reach from exploring signal transduction pathways [26, 27] and response to pharmacotherapy [27–29] to the recently established examination of gene therapy [30] and oncolytic viruses [30, 31]. Moreover, the decisive role of communication between tumor cells and their unaltered microenvironment for the settling and proliferation of metastasized tumor cells renders PCTS a potential in the basic examination of metastasis [32].

To evaluate the potential of GQDs as nanocarriers targeting human breast cancer cells, we characterized their uptake into benign MCF-10A breast epithelial, malignant luminal MCF-7 and triple-negative MDA-MB-231 breast cancer cell lines in detail. As especially for the development of nanocarriers a high degree of consistency between an experimental model system and the target tumor tissue is vital [33], we extended our analysis to the *ex vivo* model of MMTV-PyMT precision-cut mammary tumor slices

(PCMTS). Compared to the human disease, the model presents various similarities on histological and tumor biological levels, especially regarding prognostic biomarkers [34–36]. For a detailed analysis the complete penetration of GQDs into the depth of the *ex vivo* cultivated PCMTS was demonstrated constituting a highly important prerequisite for an application as drug delivery system.

## 2. Methods

A detailed description of all experimental procedures can be found in the supplementary material available online at [stacks.iop.org/NANO/30/395101/mmedia](https://stacks.iop.org/NANO/30/395101/mmedia).

### 2.1. Synthesis of GQDs

GQDs were synthesized from citric acid and diethylene-triamine in accordance to the method published by Qu *et al* [37].

### 2.2. Fluorescence analysis

FACS analysis on single cells was performed using a Beckmann Coulter *CytoFLEX* flow cytometer. Photoluminescence (PL) properties of cell suspensions and GQD solutions were recorded using a Horiba *FluoroMax-4* spectrofluorometer at an excitation wavelength of 360 nm.

### 2.3. Cultivation and incubation of GQDs on cell lines and primary cells

MCF-7, MDA-MB-231, MCF-10A monoclonal and MMTV-PyMT primary cells were cultured in selected nutrition media. Sterile GQDs were added to the cell suspensions for the indicated incubation periods. Counter-staining of various cell organelles was performed using Thermo Fisher Scientific CellLight fluorescent proteins.

### 2.4. Cultivation and incubation of GQDs on PCTS

PCTS were cut and cultured following the protocol by de Graaf *et al* [25] for handling precision cut liver slices (PCLS). For cutting a Leica *VT1200 S* vibrating blade microtome was used. Sterile GQDs were added to the nutrition media for the incubation period. Fine slices were cut using a Leica *Frigomobil* sliding microtome.

### 2.5. Confocal fluorescence microscopy

Confocal imaging on living single cells and fixated tissue slices was performed using a Zeiss *LSM 710* confocal laser scanning microscope evaluating the DAPI or Hoechst 33342 channel (405 nm excitation, 410–495 nm emission), the GQD channel (488 nm excitation, 495–530 nm emission) and the RFP channel (543 nm excitation, 550–700 nm emission).

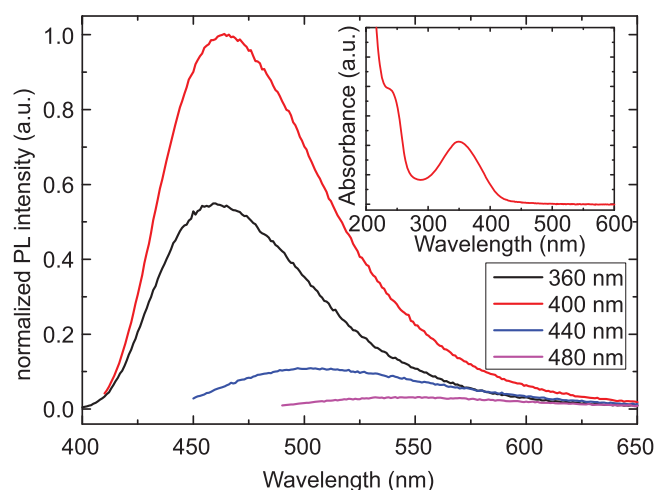


**Figure 1.** Photoluminescence (PL) spectra of the GQDs at different excitation wavelengths and the corresponding absorbance spectrum (inset).

## 2.6. Ethical statement

All animal procedures regarding C57BL/6 mice were approved by the North Rhine-Westphalia State Agency for Nature, Environment and Consumer Protection (case number: 84-02.04.2013.A358) and conform to international guidelines for the care and use of animals. All animal procedures regarding transgene MMTV-PyMT mice were approved by the Ethics Committee for Animal Research (Regierung-spraesidium Tübingen) and conform to international guidelines for the care and use of animals.

## 3. Results

### 3.1. Properties of the applied GQDs

Briefly, the GQDs present with a graphene-like, hexagonal crystal structure, have an average diameter of 3.3 nm and consist of 62% Carbon, 19% Oxygen and 19% Nitrogen atoms. Figure 1 shows the fluorescence properties of relevance for this study. At excitation wavelengths from 360 to 400 nm, the emission has a maximum around 460 nm, while the PL intensity increases with increasing excitation wavelengths. At higher excitation wavelengths, the PL intensity decreases drastically and the emission maximum shifts to higher wavelengths, reaching 550 nm at 480 nm excitation. The absorbance shows a marked peak around 350 nm with a long tail still not reaching 0 at 500 nm. In this study we mainly used the GQDs at 405 nm excitation and 460 nm emission, which fits well to the preconfigured PB450 or DAPI channel of standard flow cytometers and fluorescence microscopes. At some points the excitation of the GQDs at 488 nm was needed, which gives a markedly lower, but clearly detectable signal fitting to the FITC and PE channels of the used devices.

### 3.2. GQD uptake into benign and malignant human breast epithelial cell lines

Starting with the most primitive *in vitro* breast cancer model, we studied the uptake of GQDs into MCF-7 cells, representing the estrogen receptor (ER) positive, progesterone receptor (PgR) positive, HER2 negative luminal A-subtype, into MDA-MB-231 cells as an example for triple negative (ER negative, PgR negative, HER2 negative) breast cancer and into MCF-10A cells as a model for non-tumorigenic mammary epithelial cells. To establish a GQD concentration and a time frame, that is tolerable for the cells, we conducted the MTT viability assay at concentrations ranging from  $50 \mu\text{g ml}^{-1}$  to  $1 \text{ mg ml}^{-1}$  over a period of 24 h, 48 h and 72 h (left part of figures 2(A)–(C)). After 24 h incubation time, no significant changes (statistically significant defined as  $p < 0.05$  as compared to the untreated controls) in cell viability was detected for all cell lines and concentrations, while after 48 h a statistically significant decrease in cell viability to 67% compared to control cells was measured for MCF-7 cells at a concentration of  $1 \text{ mg ml}^{-1}$ . The viability of MDA-MB-231 cells and MCF-10A cells decreased to 74% at the same time point and concentration, but did not reach statistical significance. In contrast, a clear concentration dependent decrease in cell viability was observed for all three cell lines following 72 h of incubation with a statistically significant decrease at concentrations of  $750 \mu\text{g ml}^{-1}$  and  $1 \text{ mg ml}^{-1}$  to minimum values of 64% for MCF-7 cells, 56% for MDA-MB-231 cells and 66% for MCF-10A cells. Summarized, all three cell lines show a similar MTT pattern and the GQDs seem to be well tolerated up to concentrations of  $500 \mu\text{g ml}^{-1}$  over a time period of 48 h.

Therefore, we decided to use a GQD concentration of  $500 \mu\text{g ml}^{-1}$  and a maximum time of 48 h for the following uptake studies. The uptake of the GQDs into the cells after 48 h incubation time at a concentration of  $500 \mu\text{g ml}^{-1}$  was visualized by confocal fluorescence microscopy on living cells stained with Hoechst 33342. The right parts of figures 2(A)–(C) show the merged fluorescence images of the cells, representing the nuclei in blue (405 nm excitation, 410–495 nm emission, referred to as Hoechst 33342 channel) and the GQDs in olive (488 nm excitation, 495–630 nm emission, referred to as GQD channel). GQDs appear as bright spots as they also emit in the Hoechst 33342 channel. The observed distinct and localized bright areas near the nucleus indicate, that the GQDs accumulate in the same regions for all three cell lines.

To assess the uptake into the cell lines quantitatively, we measured the change of the cells' mean fluorescence intensity by flow cytometry (figure 2(D)) using the PB450 channel. The MDA-MB-231 and MCF-10A cells showed a similar behavior over time with a signal change of 7500 following 24 h incubation time and a change of 10 000 after 48 h of incubation, which indicates a saturation over time. In contrast, the MCF-7 cells showed a three times higher signal change, namely 22 000 after 24 h and of 30 000 after 48 h incubation time, implying a similar saturation pattern just at a higher level. Additionally, we analyzed the forward scatter (FSC)

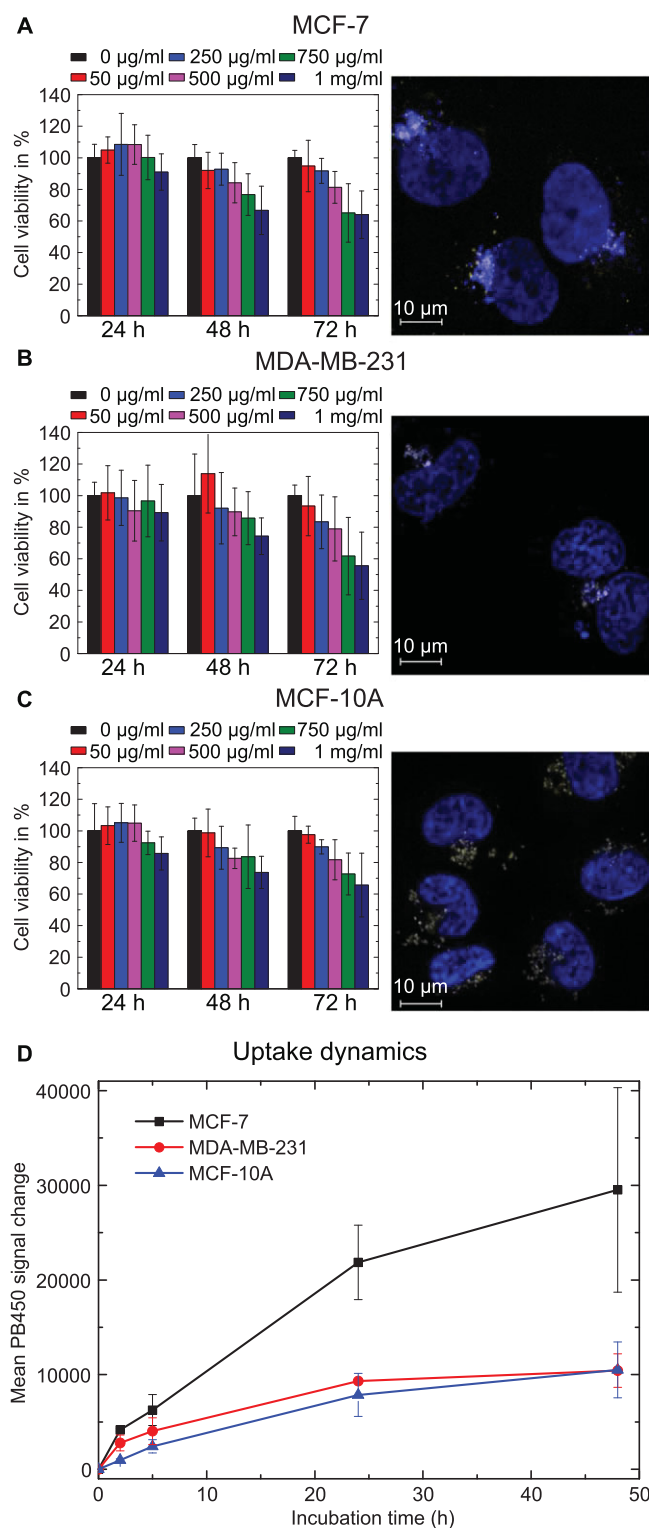


**Figure 2.** MTT assay at GQD concentrations of up to  $1 \text{ mg ml}^{-1}$  and confocal microscopy pictures of (A) MCF-7 cells, (B) MDA-MB-231 cells and (C) MCF-10A cells incubated with GQDs. The nuclei are stained with Hoechst 33342 (blue). GQDs appear as bright spots. (D) Differential uptake of the GQDs into the cells at a concentration of  $500 \text{ μg ml}^{-1}$  over a time period of 48 h as measured by flow cytometry.

data as a measure for the cells' size. The MCF-7 cells appeared to be larger than MDA-MB-231 and MCF-10A cells with a mean FSC value of  $5.1 \times 10^5$  for MCF-7 cells,  $3.9 \times 10^5$  for MDA-MB-231 cells and  $4.3 \times 10^5$  for MCF-10A cells.

In order to explore the regions of accumulation, we counter-stained various cell organelles in typically perinuclear localization using organelle specific RFP-tagged proteins (see figure 3). To depict the cell borders we first analyzed the GQDs' fluorescence channels in combination with transmitted light. In all experiments (except for the mitochondrial counter-staining) the nuclei were co-stained, as well. Again, the GQD accumulations were uniquely identified by a fluorescence signal in both the Hoechst 33342 channel and the GQD channel. A further merging with the cell organelles' fluorescence signal recorded in the RFP channel allowed the identification of the GQD containing subcellular structures: endoplasmic reticulum (figure 3(B)) and mitochondria (figure 3(F)) were depicted close to the GQD accumulations, but no superimpositions of all signals could be determined. Instead the GQDs accumulated in late endosomes (figure 3(D)) and, to a larger extent, in lysosomes (figure 3(E)). Slight shifts between the different signals that keep the morphology of the stained structures can be explained by motions of the living cells. Moreover, these structures were localized next to the Golgi apparatus, which itself did not display a direct merging of fluorescence signals with the GQDs (figure 3(C)). The localization inside late endo- and lysosomes next to Golgi apparatus and nucleus indicates that the nanoparticles are taken up via endocytosis [38, 39].

### 3.3. GQD uptake into PCTS

Next, we extended our examination towards PCTS presenting the probably closest-to-reality *in vitro* cultivation system. We started analyzing the *ex vivo* uptake of GQDs into mouse liver tissue of C57BL/6 mice, as PCLS constitute a well established model system with pre-defined methods of cultivation available. The homogeneous tissue facilitates precise cutting under defined conditions leading to comparable slices of high similarity [40]. These are optimally suited to establish incubation and analyzing methods before extending the experiment to more difficult-to-handle tumor tissue.

In order to characterize the uptake of GQDs into PCLS we performed various incubation experiments modifying slice thickness, incubation time and analyzing methods. All incubation steps were carried out using the GQD concentration of  $500 \text{ μg ml}^{-1}$  and incubation period of 48 h as previously established.

We first evaluated the GQD uptake analyzing  $20 \text{ μh}$  fine slices cut from  $300 \text{ μh}$  PCLS via confocal microscopy. As all recorded images were massively overlayed with the cells' auto-fluorescence signal in both detection channels (probably enhanced by PFA fixation [41]), a detailed subcellular localization was not possible. Exemplary images are presented in figure S1.



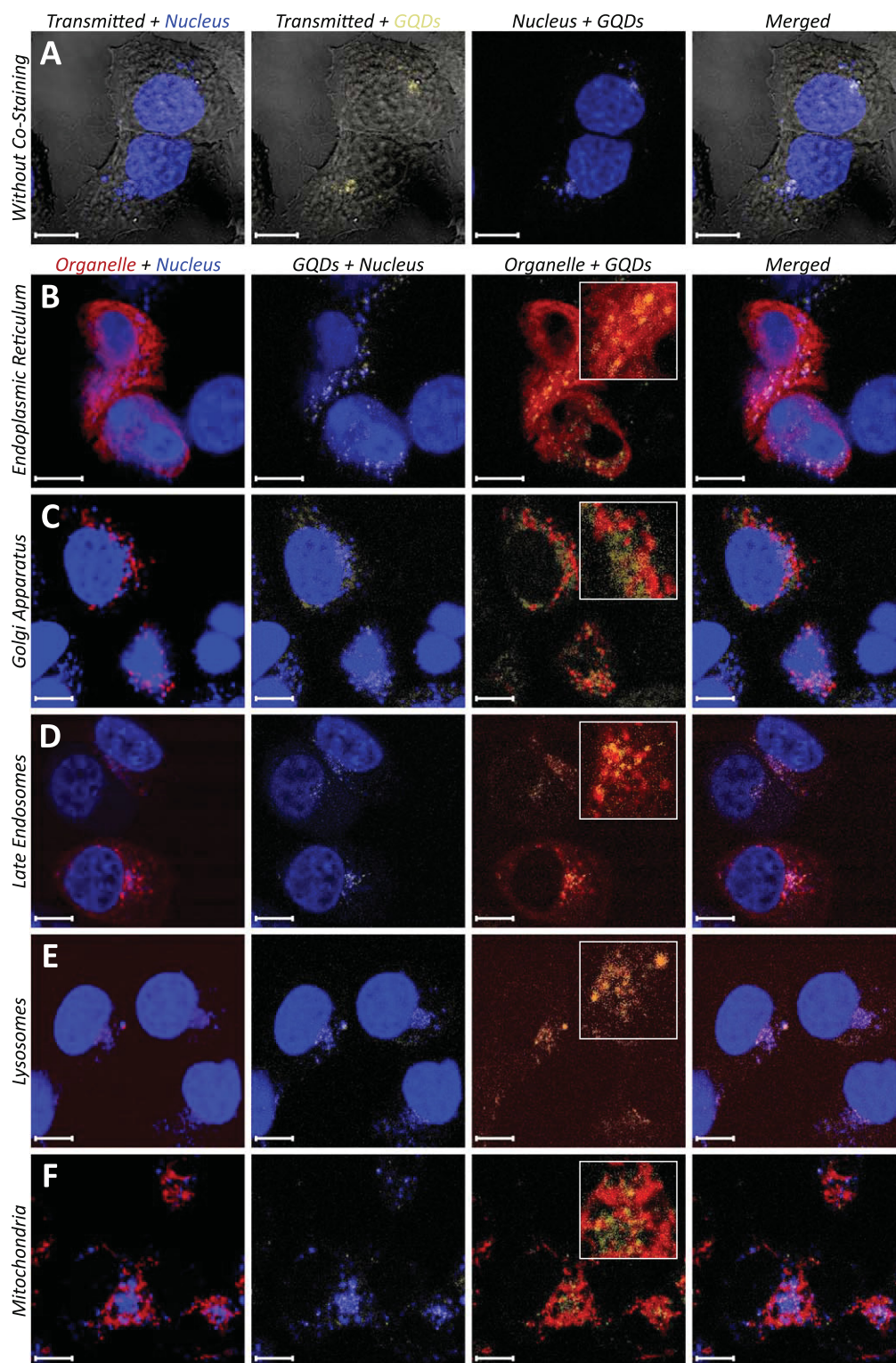


**Figure 3.** Confocal microscopy images of MCF-7 cells incubated with GQDs after counter-staining of perinuclear cell organelles. (A) Superimposition of the transmitted light, nuclei are represented in blue, GQD emissions in blue and olive. (B)–(F) Cell organelles are represented in red, nuclei in blue, GQDs in blue and olive. Merging of the blue and olive color results in a white signal, merging of the red and olive color in an orange signal and merging of all three colors in a dark yellow signal. For the mitochondrial counter-staining (F) the nucleus was not stained due to overlapping fluorescence channels of the applied dyes. All images were taken using a 63× oil objective. Scale bars: 10  $\mu$ m.

Therefore, we evaluated the fluorescence properties of dissolved complete or fine-cut PCLS using an excitation wavelength of 360 nm (corresponding to the GQDs' maximum of absorption). Generally, the incubation with GQDs led to an increase in the fluorescence intensity and a shift of the wavelength of maximum fluorescence towards the evaluated emission channel of the applied GQDs. The evaluation reached statistical significance and the results were further verified by a flow cytometric evaluation. They indicate that the GQD fluorescence dominated the cells' fluorescence spectra outstripping the native and fixative-induced autofluorescence as a consequence of the incubation experiments. This demonstrates a cellular uptake of the applied GQDs by the PCLS. Typical examples for GQD incubated and control group slices can be found in figure S2.

We further evaluated the uptake of the GQDs into the depth of PCLS. Analyzing the fluorescence of fine-cut PCLS both by fluorescence spectroscopy and by flow cytometry, we did not detect a decreasing uptake over the penetration depth (examples are presented in figures S2(C) and (D)). This indicates a homogeneous uptake into all layers of the PCLS.

After establishing culture and incubation techniques using liver tissue we extended our study to PCMTS from the mouse MMTV-PyMT model, which is widely used in experimental breast cancer research due to the spontaneous induction of multiple tumors early in life.

Already in the macroscopic examination the MMTV-PyMT tumors presented as inhomogeneous and irregularly formed, especially in comparison to the homogeneous liver tissue. Again, all uptake experiments of GQDs on PCMTS were performed for 48 h using the GQD optimized concentration for incubation experiments of  $500 \mu\text{g ml}^{-1}$  established before.

After cultivation, a histological evaluation of the PCMTS showed that about 90% of the cells were vital while 10% presented necrosis without significant differences when the slices were cultivated with or without GQDs (figure 4(A)). Furthermore, an M30 apoptosis staining was performed. Neither in the control nor in the GQD incubated PCMTS we determined a relevant amount of apoptosis (see figure S4). This indicates that the tissue slices tolerate both cultivation and incubation with GQDs without major cellular damage. For the incubation with GQDs, this observation resembles the outcome of the MTT viability assay formerly performed on monoclonal cell lines and primary tumor cells.

To verify the GQD uptake into MMTV-PyMT PCMTS we performed a statistical evaluation of the integrated fluorescence intensity signal from dissolved  $30 \mu\text{h}$  fine slices cut from  $300 \mu\text{h}$  PCMTS. For each group ( $N_{\text{GQDs}} = 44$ ,  $N_{\text{control}} = 43$ ) the slices were cut from four different tumors explanted from three mice. Following the GQD incubation we observed an increase in the integrated fluorescence intensity from  $1.9 \times 10^5$  to  $3.9 \times 10^5$  (see figure 4(B)) at an excitation wavelength of 360 nm reflecting the GQDs' maximum emission; the evaluation reached statistical significance indicated by a  $p$ -value of  $p = 1.15 \times 10^{-3}$ . We continued analyzing the wavelength of maximum fluorescence intensity by

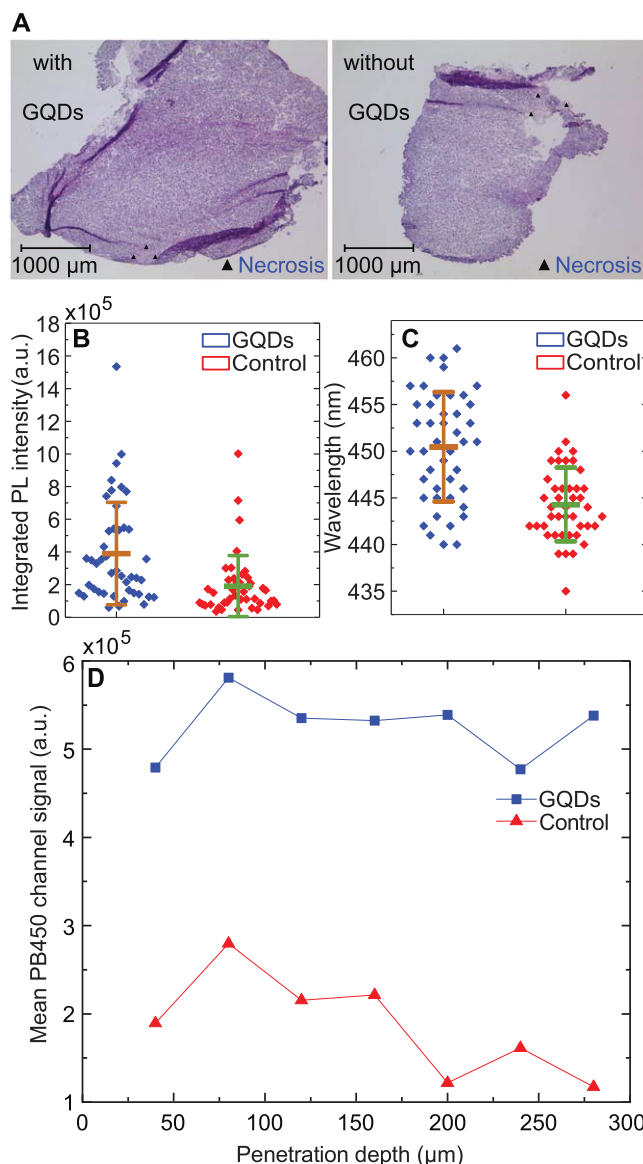


**Figure 4.** (A) HE-stained microscopic pictures of the MMTV-PyMT tissue after cultivation of the PCMTS. The images were taken using a  $2.5\times$  objective. (B) Normalized integrated fluorescence intensity for GQD incubated (blue) and control group (red) dissolved fine slices. The orange and the green bar show the mean fluorescence intensity  $\pm$  one standard deviation. The mean fluorescence intensity increased from  $1.9 \times 10^5$  to  $3.9 \times 10^5$  when the slices were incubated with GQDs. (C) Wavelength of maximum fluorescence intensity for GQD incubated (blue) and control group dissolved fine slices (red). The orange and the green bar show the mean wavelength of maximum fluorescence  $\pm$  one standard deviation. The mean wavelength of maximum fluorescence increased from  $\lambda_{\text{max}} = 444.3 \text{ nm}$  to  $\lambda_{\text{max}} = 450.5 \text{ nm}$  when the slices were incubated with GQDs. (D) GQD uptake into the depth of PCMTS displayed by mean fluorescence intensities of cells as measured by flow cytometry.

a statistical evaluation. Here, the incubation with GQDs led to a shift in wavelength from  $\lambda_{\text{max}} = 444.3 \text{ nm}$  to  $\lambda_{\text{max}} = 450.5 \text{ nm}$ . A  $p$ -value of  $p = 6.0 \times 10^{-7}$  demonstrated statistical significance (see figure 4(C)). The elevated fluorescence intensity and the wavelength shift towards the maximal emission wavelength of the applied GQDs clearly



demonstrated a cellular uptake of the GQDs into the depth of the PCMTS. This was further validated by an increase in the mean fluorescence intensity of *in toto* dissolved PCMTS recorded via flow cytometry from  $\langle I \rangle = 0.5 \times 10^5$  to  $\langle I \rangle = 4.1 \times 10^5$  following the incubation with GQDs (not shown).

To analyze a possible dependency of the GQD uptake on the penetration depth inside the slices we first regarded the integrated fluorescence intensity data as a function of the fine slices' position inside the PCMTS. In all four individually performed experiments we did not detect a significant dependency of the fluorescence intensity on the penetration depth (see figure S3 for an example comparing a GQD incubated PCMTS with a native control slice). We validated this finding by changing the analyzing method to flow cytometry. Using the flow cytometer's PB450 channel we did not detect any correlation between the mean fluorescence intensity of the single suspended cells and the position inside the PCMTS (an example is presented in figure 4(D)).

To conclude, as for the liver tissue, we could demonstrate a cellular GQD uptake into MMTV-PyMT PCMTS. As again for this tissue type no decrease of the uptake over the penetration depth was detectable applying two different methods of analysis, we assume a homogeneous uptake even into deeper tumor cell layers similar to the liver tissue.

### 3.4. GQD uptake into MMTV-PyMT primary cells

To verify the method of uptake for the particular cell types present into the MMTV-PyMT tissue, we finally analyzed MMTV-PyMT primary cells. Primary cell cultures established from a small tumor piece after collagenase D digestion constitute a more realistic model than monoclonal cell lines, as their percentage distribution of cell types may be compared to solid tissue.

Again, we started the analysis performing the MTT viability assay. As for the monoclonal cell lines, we did not see a significant decrease in cellular viability. For GQD concentrations and incubation periods up to the formerly applied parameters of  $500 \mu\text{g ml}^{-1}$  and 48 h the vitality stayed  $>90\%$  (see figure 5(A)).

For the analysis of the subcellular GQD uptake we used confocal microscopy, applying the same conditions as for the MCF-7 cells (48 h incubation time at a concentration of  $500 \mu\text{g ml}^{-1}$ ). The counter-staining of cell organelles was limited to an examination of late endosomes (figure 5(C)) and lysosomes (figure 5(D)) representing the organelles in which the GQDs localized in MCF-7 cells. In general, we could demonstrate the same subcellular accumulation of the nanoparticles as in the former experiments. Variations in the subcellular distribution of endosomes and lysosomes between MCF-7 and MMTV-PyMT cells may be explained by morphological differences between the two cell types.

To quantitatively investigate the GQD uptake by flow cytometry, we used concentrations of  $200 \mu\text{g ml}^{-1}$  and  $500 \mu\text{g ml}^{-1}$  and an incubation period for up to 48 h. For both concentrations the changes in mean fluorescence intensity (using the flow cytometer's PB450 channel) were examined

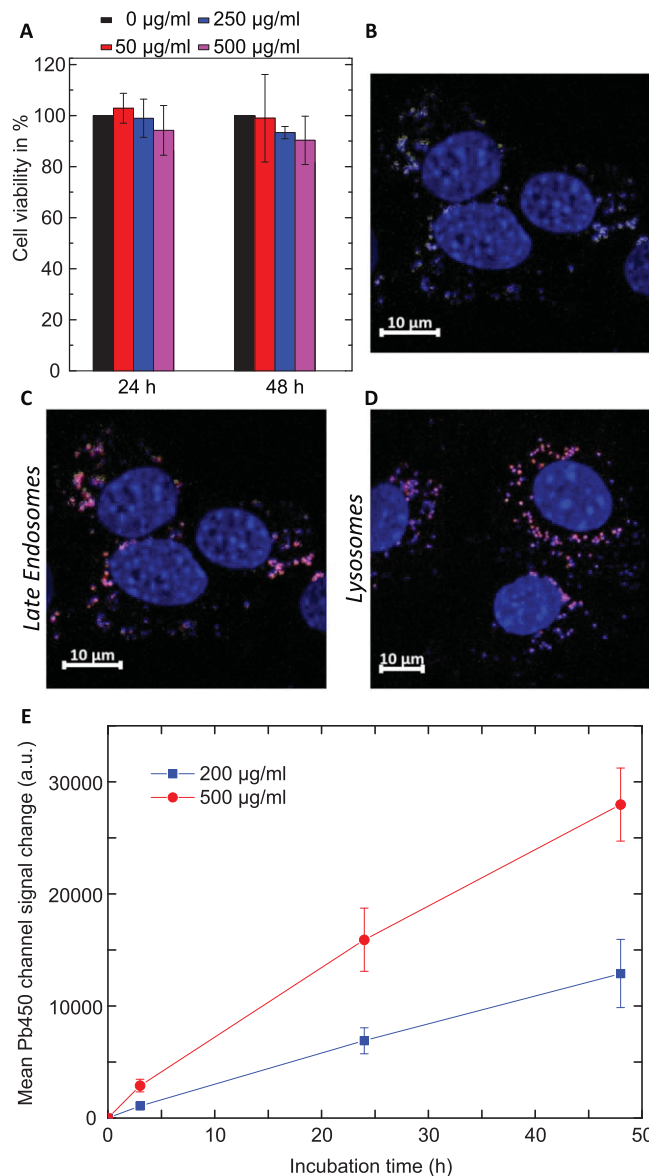


**Figure 5.** (A) Cell viability of MMTV-PyMT primary cells after 24 h and 48 h of incubation with different concentrations of GQDs. (B) Confocal microscopy images of GQD incubated MMTV-PyMT cells. (C) Counter staining of endosomes and (D) counter staining of lysosomes. (E) Temporal evolution of the fluorescence intensity measured in MMTV-PyMT primary cells after incubation with GQDs. All images were taken using a  $63\times$  oil objective.

as a function of time setting the zero point to the cells' auto-fluorescence signal and the starting point of the incubation period to  $t = 0$  h (figure 5(E)).

After 24 h of incubation we observed a signal change (with the error bars indicating the standard deviation) to 16 000 for the higher and to 7000 for the lower concentration. After 48 h the signal changed to 28 000 and 13 000, respectively. These values are comparable to the results from the former measurements on monoclonal breast epithelial and adenocarcinoma cells.

## 4. Discussion

In this study the uptake of GQDs into various breast cancer tumor models was studied in detail. All cell types analyzed in our experiments (in particular benign epithelial and adenocarcinoma cells of different malignancy) depicted a cellular uptake of GQDs, which did not reach complete saturation over the incubation period of 48 h. MCF-7 cells showed a three fold higher uptake as compared to MDA-MB-231 and MCF-10A cells. This can only partially be explained by the cells' size, as the forward scatter data only translates into a 1.5 fold higher surface area of MCF-7 cells. Therefore luminal MCF-7 cells seem to have a higher natural affinity for the uptake of GQDs than triple negative MDA-MB-231 cells and benign MCF-10A cells. This might be related to an endocytotic uptake, as MCF-7 are known to have a high endocytosis rate as compared to other cell lines [42].

The method of uptake is decisive for a nanoparticle's intracellular fate [43], which in consequence may influence the applicability for drug delivery. Moreover, the uptake mechanism is strongly dependent on the physical properties of the applied particle [44].

The model of *in vitro* cultivated cell lines allowed for a subcellular localization of the nanoparticles in living cells via confocal fluorescence microscopy. Inside the cells the particles were localized in late endosomes and lysosomes, which is consistent with a mechanism of uptake via endocytosis. Similar observations were made analyzing primary breast cancer cells. These may be regarded a superior model system compared to tumor cell lines, as long-term cultivated immortalized monoclonal cells are prone to genotypic and phenotypic drifting [45].

An endocytotic uptake has been described for different types of nanoparticles [43] and is connected with a membranous encapsulation inside the endolysosomal system [38]. This might be the reason for the low cytotoxicity of the applied GQDs. For constructing a drug delivery system, however, an endosomal escape has to be achieved to render cytosolic and nuclear access to the particles. Otherwise, an application stays limited to the specific field of pharmaceuticals targeting structures inside the endolysosomal system such as pH-dependent pro-drugs, lysosomal enzymes and inhibitors of  $\beta$ -secretase [46].

To evaluate a more close to reality model system, we transferred our analysis to the examination of PCTSs. We started analyzing the *ex vivo* uptake of GQDs into mouse liver tissue of C57BL/6 mice as a well established model system. Regarding gene expression PCLS show the highest degree of similarity in comparison to liver cell lines and hepatocyte cultures [47].

We found a homogeneous uptake into all layers of the PCLS, which is of relevance as the liver plays an important role for the bio-transformation, metabolization and toxicity of nanoparticles. For example, carbon nanotubes showed a long-term accumulation in this organ, which underlines its importance for toxicology studies [48]. More recently, carbonate apatite nanoparticles were used to deliver the pro-drug

cyclophosphamide into murine livers, where it was activated for a later treatment of breast cancer [49].

Especially for the evaluation of pharmaceutical effects on tumors the *ex vivo* system can represent a vital tool, as the sensitivity of breast cancer cells to cytostatics depends on dynamic interactions between tumor cells and their micro-environment [50]. Moreover, PCTSs can depict the intra- and inter-tumoral variability of solid tumors to a larger extent [51].

The *ex vivo* breast cancer model represents the most sophisticated tumor model we used and may depict the *in vivo* situation in breast cancer to a large extent. For tumor biology studies, cultivation of PCTS offers the chance to allow deeper insights into the underlying pathogenic processes than highly reductionist cell lines, as alterations in biology and pharmacology regarding signal dynamics within a tumor's micro-environment can be studied [52]. Thus, they might be regarded as one of the most realistic model systems to perform basic uptake analysis for building up a nanoparticle based drug delivery system, before extending the examinations towards animal experiments necessitating unlikely larger cost and regularly effort. In our experiments the GQDs had no obvious negative effects on the viability of the tissue as assessed by M30 CytoDEATH assay and a histological evaluation. Unfortunately, we were not able to perform a subcellular localization of the applied GQDs inside the tissue slices, as confocal microscopy on fixated cells was hampered by a massive auto-fluorescence and live experiments are not possible due to the necessity of cutting the tissue to thinner slices. We therefore changed our method of analysis to evaluating the fluorescence of dissolved PCMTS. We were not only able to verify the cellular uptake, but did also detect a homogeneous uptake into the depth of the tissue. This result is consistent with the distribution of the fluorescent dyes rhodamine B and lucigenin in rat precision-cut liver slices [53] and fluorescence marked taxol in human mammary breast cancer slices [50].

In conclusion, the complete penetration of the GQDs into the solid tumor slices without obvious negative effects on the viability of the tissue is promising for a usage as core of a drug delivery system, since for that purpose a distribution of anti-cancer drugs throughout complete tumors has to be ensured. First studies of such a system should concentrate on the luminal type, as MCF-7 cells appear to have a distinct higher uptake of GQDs. Nevertheless, the GQDs appear to be encapsulated in endosomes and lysosomes. Therefore endosomal escape has to be achieved to target the cytoplasm or the nucleus.

## Acknowledgments

SF acknowledges financial support of his position by the Düsseldorf School of Oncology (DSO). TH acknowledges support by the Betz foundation. Access to the confocal microscope at the Center of Advanced imaging (CAi) of HHU Düsseldorf is gratefully acknowledged. The authors thank C



A M Seidel for access to the Horiba FluoroMax spectrofluorometer and the Agilent Cary 4000 spectrophotometer.

## ORCID iDs

Stefan Fasbender  <https://orcid.org/0000-0003-3054-7720>

Thomas Heinzel  <https://orcid.org/0000-0001-5149-4379>

## References

- [1] Liu D, Yang F, Xiong F and Gu N 2016 *Theranostics* **6** 1306
- [2] Gelperina S, Kisich K, Iseman M D and Heifets L 2005 *Am. J. Respir. Crit. Care Med.* **172** 12
- [3] Sun D, Zhuang X, Xiang X, Liu Y, Zhang S, Liu C, Barnes S, Grizzle W, Miller D and Zhang H 2010 *Mol. Ther.* **18** 1606
- [4] Cho K, Wang X, Nie S, Chen Z and Shin D M 2008 *Clin. Cancer Res.* **14** 1310
- [5] Ling X, Chen X, Ridell I A, Tao W, Wang J, Hollett G, Lippard S J, Farokhzad O C, Shi J and Wu J 2018 *Nano Lett.* **18** 4618
- [6] Lancet J *et al* 2017 *Biol. Blood Marrow Transplant.* **23** S38
- [7] Nazir S, Hussain T, Ayub A, Rashid U and MacRobert A J 2014 *Nanomedicine: NBM* **10** 19
- [8] Kim S *et al* 2012 *ACS Nano* **6** 8203
- [9] Jin S H, Kim D H, Jun G H, Hong S H and Jeon S 2013 *ACS Nano* **7** 1239
- [10] Huang H, Liu M, Tuo X, Chen J, Mao L, Wen Y, Tian J, Zhou N, Zhang X and Wei Y 2018 A novel thiol-ene click reaction for preparation of graphene quantum dots and their potential for fluorescence imaging *Mater. Sci. Eng. C* **91** 631–7
- [11] Shang W, Zhang X, Zhang M, Fang Z, Sun Y, Han M and Fan L 2014 The uptake mechanism and biocompatibility of graphene quantum dots with human neural stem cells *Nanoscale* **6** 5799
- [12] Fasbender S *et al* 2017 *RSC Adv.* **7** 12208–16
- [13] Liu Q, Guo B, Rao Z, Zhang B and Gong J 2013 *Nano Lett.* **13** 2436–41
- [14] Zhang M *et al* 2012 Facile synthesis of water-soluble, highly fluorescent graphene quantum dots as a robust biological label for stem cells *J. Mater. Chem.* **22** 7461
- [15] Al-Ogaidi I, Gou H, Aguilar Z, Guo S, Melconian A, Al-Kazaz A, Meng F and Wu N 2014 *Chem. Commun.* **50** 1344–6
- [16] Wu Z L, Gao M X, Wang T T, Wan X Y, Zheng L L and Huang C Z 2014 A general quantitative pH sensor developed with dicyandiamide n-doped high quantum yield graphene quantum dots *Nanoscale* **6** 3868
- [17] Sui X, Luo C, Wang C, Zhang F, Zhang J and Guo S 2016 Graphene quantum dots enhance anticancer activity of cisplatin via increasing its cellular and nuclear uptake *Nanomedicine: Nanotechnol. Biol. Med.* **12** 1997–2006
- [18] Gong X, Zhang Q, Gao Y, Shuang S, Choi M M F and Dong C 2016 Phosphorus and nitrogen dual-doped hollow carbon dot as a nanocarrier for doxorubicin delivery and biological imaging *ACS Appl. Mater. Interfaces* **8** 11288
- [19] Iannazzo D, Pistone A, Salamo M, Galvagno S, Romeo R, Giofre S V, Branca C, Visalli G and Petro A D 2017 *Int. J. Pharm.* **518** 185–92
- [20] Ding H, Zhang F, Zhao C, Lv Y, Ma G, Wei W and Tian Z 2017 *ACS Appl. Mater. Interfaces* **9** 27396
- [21] Torre L A, Siegel R L, Ward E M and Jemal A 2016 Global cancer incidence and mortality rates and trends—an update *Cancer Epidemiol. Prevention Biomarkers* **25** 16–27
- [22] Youlden D R, Cramb S M, Dunn N A M, Muller J M, Pyke C M and Baade P D 2012 The descriptive epidemiology of female breast cancer: an international comparison of screening, incidence, survival and mortality *Cancer Epidemiol.* **36** 237–48
- [23] Burdall S E, Hanby A M, Lansdown M R and Speirs V 2003 Breast cancer cell lines: friend or foe? *Breast Cancer Res.* **5** 89–95
- [24] Holliday D L, Moss M A, Pollock S, Lane S, Shaaban A M, Millican-Slater R, Nash C, Hanby A M and Speirs V 2013 The practicalities of using tissue slices as preclinical organotypic breast cancer models *J. Clin. Pathol.* **66** 253–5
- [25] de Graaf I A M, Olinga P, de Jager M H, Merema M T, de Kanter R, van de Kerkhof E G and Groothuis G M M 2010 Preparation and incubation of precision-cut liver and intestinal slices for application in drug metabolism and toxicity studies *Nat. Protocols* **5** 1540–51
- [26] Närhi K *et al* 2018 Spatial aspects of oncogenic signalling determine the response to combination therapy in slice explants from kras-driven lung tumours *J. Pathol.* **245** 101–13
- [27] Parajuli N and Doppler W 2009 Precision-cut slice cultures of tumors from mmtv-neu mice for the study of the *ex vivo* response to cytokines and cytotoxic drugs *In Vitro Cell. Dev. Biol.—Animal* **45** 442–50
- [28] Naipal K A T, Verkaik N S, Sánchez H, van Deurzen C H M, den Bakker M A, Hoeijmakers J H, Kanaar R, Vreeswijk M P, Jager A and van Gent D C 2016 Tumor slice culture system to assess drug response of primary breast cancer *BMC Cancer* **16** 78
- [29] Hirn S, Haberl N, Loza K, Eppel M, Kreyling W G, Rothen-Rutishauser B, Rehberg M and Krombach F 2014 Proinflammatory and cytotoxic response to nanoparticles in precision-cut lung slices *Beil. J. Nanotechnol.* **5** 2440–9
- [30] Rosales Gerpe M C, van Vloten J P, Santry L A, de Jong J, Mould R C, Pelin A, Bell J C, Bridle B W and Wootton S K 2018 Use of precision-cut lung slices as an *ex vivo* tool for evaluating viruses and viral vectors for gene and oncolytic therapy *Mol. Ther. Methods Clin. Dev.* **10** 245–56
- [31] Pennington K, Chu Q D, Curiel D T, Li B D and Mathis J M 2010 The utility of a tissue slice model system to determine breast cancer infectivity by oncolytic adenoviruses *J. Surg. Res.* **163** 270–5
- [32] Koch A, Saran S, Tran D D H, Klebba-Färber S, Thiesler H, Sewald K, Schindler S, Braun A, Klopffleisch R and Tamura T 2014 Murine precision-cut liver slices (pcls): a new tool for studying tumor microenvironments and cell signaling *ex vivo Cell Commun. Signaling* **12** 73
- [33] Rosenblum D, Joshi N, Tao W, Karp J M and Peer D 2018 Progress and challenges towards targeted delivery of cancer therapeutics *Nat. Commun.* **9** 1410
- [34] Lin E Y, Jones J G, Li P, Zhu L, Whitney K D, Muller W J and Pollard J W 2003 Progression to malignancy in the polyoma middle t oncoprotein mouse breast cancer model provides a reliable model for human diseases *Am. J. Pathol.* **163** 2113–26
- [35] Guy C T, Cardiff C T and Muller C T 1992 Induction of mammary tumors by expression of polyomavirus middle t oncogene: a transgenic mouse model for metastatic disease *Mol. Cell Biol.* **12** 954–61
- [36] Steudel F A *et al* 2017 Sk4 channels modulate  $Ca^{2+}$  signalling and cell cycle progression in murine breast cancer *Mol. Oncol.* **11** 1172–88
- [37] Qu D, Zheng M, Li J, Xie Z and Sun Z 2015 Tailoring color emissions from n-doped graphene quantum dots for bioimaging applications *Light: Sci. Appl.* **4** e364
- [38] Huotari J and Helenius A 2011 Endosome maturation *EMBO J.* **30** 3481–500

- [39] Maxfield F R and McGraw T E 2004 Endocytic recycling *Nat. Rev. Mol. Cell Biol.* **5** 121
- [40] Zimmermann M, Lampe J, Lange S, Smirnow I, Königsrainer A, Hann-von Weyhern C, Fend F, Gregor M, Bitzer M and Lauer U M 2009 Improved reproducibility in preparing precision-cut liver tissue slices *Cytotechnology* **61** 145–52
- [41] Baschong W, Suetterlin R and Laeng R H 2001 Control of autofluorescence of archival formaldehyde-fixed, paraffin-embedded tissue in confocal laser scanning microscopy (clsm) *J. Histochem. Cytochem.* **49** 1565–71
- [42] de Beco S, Gueudry C, Amblard F and Coscoy S 2009 Endocytosis is required for e-cadherin redistribution at mature adherens junctions *Proc. Natl Acad. Soc.* **106** 7010–5
- [43] Adjei I M, Sharma B and Labhasetwar V 2014 *Nanoparticles: Cellular Uptake and Cytotoxicity* (Dordrecht: Springer)
- [44] Nativo P, Prior I A and Brust M 2008 Uptake and intracellular fate of surface-modified gold nanoparticles *ACS Nano* **2** 1639–44
- [45] Pan C, Kumar C, Bohl S, Klingmueller U and Mann M 2009 Comparative proteomic phenotyping of cell lines and primary cells to assess preservation of cell type-specific functions *Mol. Cell. Proteomics* **8** 443–50
- [46] Rajendran L, Knolker H-J and Simons K 2010 Subcellular targeting strategies for drug design and delivery *Nat. Rev. Drug Discovery* **9** 29–42
- [47] Boess F, Kamber M, Romer S, Gasser R, Muller D, Albertini S and Suter L 2003 Gene expression in two hepatic cell lines, cultured primary hepatocytes, and liver slices compared to the *in vivo* liver gene expression in rats: Possible implications for toxicogenomics use of *in vitro* systems *Toxicol. Sci.* **73** 386–402
- [48] Schipper M L, Nakayama-Ratchford N, Davis C R, Kam N W S, Chu P, Liu Z, Sun X, Dai H and Gambhir S S 2008 A pilot toxicology study of single-walled carbon nanotubes in a small sample of mice *Nat. Nanotechnol.* **3** 216–21
- [49] Tiash S and Chowdhury M E H 2016 Passive targeting of cyclophosphamide-loaded carbonate apatite nanoparticles to liver impedes breast tumor growth in a syngeneic model *Curr. Pharm. Des.* **22** 5752–9
- [50] van der Kuip H, Mürdter T E, Sonnenberg M, McClellan M, Gutzeit S, Gerteis A, Simon W, Fritz P and Aulitzky W E 2006 Short term culture of breast cancer tissues to study the activity of the anticancer drug taxol in an intact tumor environment *BMC Cancer* **6** 86
- [51] Hickman J A, Graeser R, de Hoogt R, Vidic S, Brito C, Gutekunst M, van der Kuip H and IMI PREDECT consortium 2014 Three-dimensional models of cancer for pharmacology and cancer cell biology: capturing tumor complexity *in vitro/ex vivo Biotechnol. J.* **9** 1115–28
- [52] Davies E J *et al* 2015 Capturing complex tumour biology *in vitro*: histological and molecular characterisation of precision cut slices *Sci. Rep.* **5** 17187
- [53] Olinga P, Meijer D, Slooff M and Groothuis G 1997 Liver slices in *in vitro* pharmacotoxicology with special reference to the use of human liver tissue *Toxicol. in Vitro* **12** 77–100

# Supporting information for: From in vitro to ex vivo: Subcellular localization and uptake of graphene quantum dots into solid tumors

David Kersting<sup>a</sup>, Stefan Fasbender<sup>a</sup>, Rabea Pilch<sup>a</sup>, Jennifer Kurth<sup>a</sup>, André Franken<sup>b</sup>, Marina Ludescher<sup>b</sup>, Johanna Naskou<sup>b</sup>, Angelika Hallenberger<sup>c</sup>, Charlotte von Gall<sup>c</sup>, Corinna J. Mohr<sup>d</sup>, Robert Lukowski<sup>d</sup>, Katharina Raba<sup>e</sup>, Sandra Jaschinski<sup>f</sup>, Irene Esposito<sup>f</sup>, Johannes C. Fischer<sup>e</sup>, Tanja Fehm<sup>b</sup>, Dieter Niederacher<sup>b</sup>, Hans Neubauer<sup>b</sup>, Thomas Heinzel<sup>a,\*</sup>

<sup>a</sup>Condensed Matter Physics Laboratory, Heinrich-Heine-University, 40204 Düsseldorf, Germany

<sup>b</sup>Department of Obstetrics and Gynecology, University Hospital and Medical Faculty, Heinrich-Heine-University, 40204 Düsseldorf, Germany

<sup>c</sup>Institute for Anatomy II, Medical Faculty, Heinrich-Heine-University, 40204 Düsseldorf, Germany

<sup>d</sup>Department of Pharmacology, Toxicology and Clinical Pharmacy, University of Tübingen, 72076 Tübingen, Germany

<sup>e</sup>Institute for Transplantation Diagnostics and Cell Therapeutics, Heinrich-Heine-University, 40204 Düsseldorf, Germany

<sup>f</sup>Institute of Pathology, University Hospital and Medical Faculty, Heinrich-Heine-University, 40204 Düsseldorf, Germany

---

## 1. EXPERIMENTAL SECTION

### 1.1. Materials

Citric acid (ACS reagent, 99.5%), diethylenetriamine (ReagentPlus, 99%) and Dispase II (neutral protease, grade II) were purchased from Sigma Aldrich (St. Louis, USA). Fetal Bovine Serum (FBS), Dulbecco's Modified Eagle Medium *high glucose*, *GlutaMAX*, *pyruvate* (DMEM), Richter's Minimum Essential Medium (IMEM), penicillin/streptomycin solution, 10x Hank's Balanced Salt solution *with Ca*, *with Ma*, *without phenol red* (HBSS), HEPES (1M) and Dulbecco's Phosphate Buffered Saline (PBS) were obtained from Thermo Fisher Scientific (Waltham, USA). Collagenase D was purchased from Roche (Mannheim, Germany). Float-A-Lyzer dialysis devices (100-500 Da) and sterile filters (200 nm) were obtained from VWR (Radnor, USA). Cell culture flasks, well plates and cell strainer were purchased from Greiner Bio-One (Kremsmünster, Austria). Unless otherwise stated, all further solid and fluid chemicals were purchased from Sigma Aldrich.

All incubation steps were performed in a Heracell 150i incubator (Thermo Fisher Scientific). Centrifugation steps were carried out using a Heraeus Biofuge Primo R centrifuge (Thermo Fisher Scientific), micro-centrifugation steps using a 5430 R micro-centrifuge (Eppendorf, Hamburg, Germany).

---

\*Corresponding author

Email address: Thomas.Heinzel@hhu.de (Thomas Heinzel)

### 1.2. Synthesis of Graphene Quantum Dots (GQDs)

Fluorescent GQDs were synthesized slightly modifying the method published by Qu et al.: [1] 1 mmol citric acid (0.21 g) and 3 mmol diethylenetriamine (0.34 g) were mingled using a magnetic stirrer and heated up to 180 °C for 2 min via microwave application in an *Explorer* microwave oven (CEM, Matthews, USA). The viscous GQD solution was solved in 3 ml ddH<sub>2</sub>O and educt waste were removed by dialyzing 10 ml of GQD solution against 2 l of ddH<sub>2</sub>O for 48 h with one water exchange after 24 h using a 100-500 Da dialysis membrane. Finally, the GQDs were dried and weighed using an A 200S electronic analytical balance (Sartorius, Goettingen, Germany).

### 1.3. Optical characterization of GQDs

#### 1.4. Incubation of GQDs on monoclonal cell lines

MCF-7 cells and MDA-MB-231 cells were cultured in RPMI supplemented with 10 % FBS, 1 % penicillin/streptomycin solution and 25 mM HEPES. MCF-10A cells were cultured in MEM basal medium supplemented with 0.4 % BPE, 0.1 % hEGF, 0.1 % Insulin, 0.1 % hydrocortison, 0.1 % GA-1000 and 100 ng ml<sup>-1</sup> cholera toxin. For MTT assays, 5 000 cells per well were seeded in 96 well plates in 200 µl culture medium. 24 h later, the culture medium was replaced by culture medium containing the appropriate concentration of sterile filtered GQDs. After the particular culture period, the cells were washed with PBS and incubated with 100 µl MTT solution for 3 h. Finally, the MTT solution was removed and 100 µl DMSO were added for 1 h, before the absorbance at 540 nm was measured using an Anthos htII reader. For flow cytometry measurements, 50 000 cells per well were seeded in 12 well plates in 1.2 ml culture medium. 24 h later, the culture medium was replaced by culture medium containing the appropriate concentration of sterile filtered GQDs. After the particular culture period, cells were washed with PBS, detached with 0.5 ml trypsin and resuspended in 100 µl medium. Finally, cells were fixed with 100 100 µl PFA and analysed by flow cytometry. Three independent experiments were carried out for all times and concentrations.

#### 1.5. Flow cytometry analysis of suspended cells

FACS analysis was performed using a *CytoFLEX* flow cytometer (Beckmann Coulter, Brea, USA). For analyzing cell lines and primary cells debris, necrotic cells, clumps and doublets were removed by gating the cells in a forward vs. sideward scatter plot (FSC vs. SSC) and a sideward scatter width vs. sideward scatter height plot (SSC-W vs. SSC-H). For further evaluation the PB450 channel (excitation: 405 nm, detection: 450 nm) representing the applied GQDs' stronger fluorescence channel was used; for completion, the PE channel (excitation: 480 nm, detection: 550 nm) exciting a weaker fluorescence signal in the GQDs was utilized, as well. The analysis was carried out using the Beckmann Coulter *CytExpert* software directly calculating mean fluorescence intensity and standard deviation. All further evaluation was performed in *OriginPro 9*. For every condition at least 1000 events were measured.

#### 1.6. Confocal fluorescence microscopy on living cells

For confocal fluorescence microscopy,  $8 \times 10^4$  cells in 700 µl culture medium per well (notably RPMI without phenol red was used for the imaging experiments) were seeded into an ibidi 4 Well µ-Slide. The cells were cultured in 2 wells without and in 2 wells with GQDs at a concentration of 500 µg ml<sup>-1</sup> over a period of 48 hours. For labeling of specific cell structures 20 µl of the corresponding CellLight RFP reagent were added for the last 24 hours. Afterwards, the cells

were washed with PBS before incubation with NucBlue™ LiveReady Probes™ Reagent for nucleus staining with Hoechst 33342 performed on 1 well with GQDs and 1 well without GQDs. After 10 minutes of incubation at a concentration of 2 drops NucBlue per ml solved in PBS (the remaining two wells not designated for nucleus staining were just incubated with PBS during the same time period), the cells were washed three times with PBS again, 700 µl medium were added and confocal fluorescence microscopy was performed using a Zeiss LSM 710 confocal laser scanning system. Three fluorescence channels were measured, the Hoechst 33342 channel (405 nm excitation, 410 nm - 495 nm emission), the GQD channel (488 nm excitation, 495 nm - 530 nm emission) and the RFP channel (543 nm excitation, 550 nm - 700 nm emission)

#### 1.7. Incubation of GQDs on MMTV-PyMT Primary Cells

Primary MMTV-PyMT<sup>tg/+</sup> tumor cell monolayers were cultivated in cell culture flasks in IMEM containing 5% FBS and 1% penicillin/streptomycin at 37 °C and 5% CO<sub>2</sub> in a humidified atmosphere as described in [2]. For incubation with GQDs  $4 \times 10^4$  cells were distributed in 1.2 µl culture medium each in 12 well plates at day -1. At day 0 the incubation period started with renewing the culture media in all wells using incubation media with GQD concentrations of 200 µg ml<sup>-1</sup> and 500 µg ml<sup>-1</sup> (each sterile filtered) for two wells. After 24 h, 45 h and 48 h (directly before the end of the incubation period) the media were changed using the GQD suspensions in two more wells. The resulting incubation times were 48 h, 24 h, 3 h and 0 h. Following the incubation, the cells were washed once using PBS and resuspended after trypsin treatment in 100 µl PBS/1% FBS for flow cytometry.

#### 1.8. Tissue Collection

Mice livers were removed from C57BL/6 mice, that were purchased from Janvier Labs (Le Genest-Saint-Isle, France) and held in standard cages with free access to food and water under a 12 h light-dark cycle. All animal procedures were approved by the North Rhine-Westphalia State Agency for Nature, Environment and Consumer Protection (case number: 84-02.04.2013.A358) and conform to international guidelines for the care and use of animals. On the day of experimentation a mouse was narcotized by adding 5% Isoflurane to their breathing air and sacrificed by decapitation; the liver lobes were explanted immediately or after perfusing the arterial system with 0.9% NaCl solution, respectively. The organs were washed and stored in ice-cold *liver cutting solution* (see below) until PCLS preparation.

MMTV-PyMT tumors were explanted from transgene MMTV-PyMT<sup>tg/+</sup> mice on a genetic FVB/N background [3] purchased from Jackson Laboratory (Bar Harbor, USA) and housed in a 12 h light-dark circle with access to water and food ad libitum. All animal experiments were approved by the local Ethics Committee for Animal Research (Regierungspresidium Tübingen). On the day of experimentation the mice were euthanized for removal of the solid MMTV-PyMT tumors (see [2] for further experimental documentation). The tumor tissue was transported for 5.5 h on ice in *Custodiol* organ preservation solution (Dr. Franz Koehler Chemie, Bensheim, Germany) prior to preparing the PCMTS.

#### 1.9. Incubation of GQDs on Precision-Cut Tissue Slices

PCTS were cut and cultivated in accordance to the protocol by de Graaf et al. [4] for handling PCLS adding slightly modifications, especially regarding the PCMTS: Cutting of liver tissue was performed in a *liver cutting solution* (10x HBSS containing 1% HEPES, 1% penicillin/streptomycin, 0.0375% NaHCO<sub>3</sub>), whereas for MMTV-PyMT tissue *Custodiol* organ preservation solution was used. The tissue was cut into PCTS of a defined thickness of 200 µm or



300  $\mu\text{m}$  using a *VT1200 S* vibrating blade microtome (Leica, Wetzlar, Germany) and optimized cutting parameters (amplitude: 1.55 mm, velocity: 1  $\text{mm s}^{-1}$ ), which were immediately transferred into ice-cold cutting solution after one organ was completely processed.

PCTS pairs of similar sizes (to perform a negative control in each single experiment) were chosen and transferred into ice-cold pre-oxygenated nutrition medium (DMEM containing 5% FBS, 1% penicillin/streptomycin and 1% 1M HEPES for PCLS and IMEM containing 5% FBS and 1% penicillin/streptomycin for PCMTS, respectively). For restoring the ATP-content a pre-incubation step was performed first: The PCTS were relocated into 6 well plates containing 3 ml pre-warmed pre-oxygenated nutrition medium per well (one PCTS per well) and incubated at 37 °C and 5%  $\text{CO}_2$ . After 1 h to 3 h the tissue slices were displaced into new well plates containing fresh pre-warmed pre-oxygenated nutrition medium using media with a GQD concentration of 500  $\mu\text{g ml}^{-1}$  (sterile filtered) for half of the slices and incubated again for 24 h. Eventually, the last step was repeated once for a total incubation period of 48 h.

Following the incubation, the PCTS were washed for 5 min in PBS for removal of the GQD suspension and fixated in PBS/4% PFA for 1 h at 4 °C. After 4 additional washing steps (in PBS) the slices were stored in PBS/30% Sucrose for up to 14 d at 4 °C until sinking to the well bottoms. Soaking in Sucrose solution is necessary for cryoprotection. At that point storage at –80 °C in *O.C.T. Compound Mounting Medium for Cryotomy* (VWR) was possible.

#### 1.10. Preparation of fine slices and homogenization

For investigating the GQD uptake inside the depth of the PCTS 20  $\mu\text{m}$ , 30  $\mu\text{m}$  or 40  $\mu\text{m}$  fine slices were cut using a *Frigomobil* sliding microtome (Leica). To determine the GQD uptake complete or fine cut PCTS were dissolved in a 1.4 U  $\text{ml}^{-1}$  Dispase II and 0.4 mg  $\text{ml}^{-1}$  Collagenase D solution (in PBS) for 90 min up to 150 min with gentle agitation at 37 °C. In order to record fluorescence spectra the cells were centrifuged and resuspended in PBS, for flow cytometry an additional filter step through a 40  $\mu\text{m}$  cell strainer was performed in between.

#### 1.11. Histologic examination of PCTS

For confocal imaging 20  $\mu\text{m}$  fine slices were cut from cryopreserved PCTS embedded in *O.C.T. Compound Mounting Medium for Cryotomy* using a *CM3050 S* cryostat (Leica) at –50 °C and dried onto *Starfrost* adhesive microscope slides (Knittel, Braunschweig, Germany). For DAPI staining 15  $\mu\text{l}$  (2 drops per ml in PBS) of *NucBlue Fixed Cell ReadyProbes Reagent* (Thermo Fisher Scientific) were applied in between for 10 min and washed out twice using PBS. After coverslips were applied using *Fluoromount-G* mounting medium (SouthernBiotech, Birmingham, USA), the slides were dried in the dark at room temperature for 24 h. Confocal imaging was performed using a *LSM 710* confocal laser scanning microscope (Carl Zeiss, Oberkochen, Germany) evaluating the DAPI channel (405 nm excitation, 410 nm - 495 nm emission) and the GQD channel (488 nm excitation, 495 nm - 630 nm emission).

#### 1.12. GQD uptake characterization into PCTS using fluorescence spectroscopy

Photoluminescence properties of cell suspensions were measured using a *FluoroMax-4* spectrofluorometer (Horiba, Kyoto, Japan) at an excitation wavelength of 360 nm; the R1c/S1c data were imported into *MATLAB R2017a* (MathWorks, Natick, USA). For analysis the signal of the dissolving solution was subtracted from the analyzed probes signal and the zero point was set to the signal's absolute minimum between 500 nm and 600 nm.

For determining the wavelength of maximal emission, the processed signal was smoothed using a *LOESS* regression analysis and the relative maximum between 435 nm and 465 nm was determined. To analyze the overall fluorescence intensity, a numerical integration between 400 nm and 600 nm was performed (using the data set before smoothing). To further standardize these values, the cell concentrations in the analyzed suspensions were measured using a *Moxi Z Mini* automated Cell Counter (ORFLO, Ketchum, USA). All further (statistical) evaluation was performed in *OriginPro 9* (OriginLab, Northampton, USA).

#### *1.13. GQD uptake characterization into PCTS using flow cytometry*

FACS analysis was performed using a *CytoFLEX* flow cytometer (Beckmann Coulter, Brea, USA); for analyzing PCTS, the total recorded signal in the PB450 channel (excitation: 405 nm, detection: 450 nm) representing the applied GQDs' stronger fluorescence channel and, for completion, the PE channel (excitation: 480 nm, detection: 550 nm) exciting a weaker fluorescence signal in the GQDs were used. The analysis was carried out using the Beckmann Coulter *CytExpert* software directly calculating the mean fluorescence intensity. All further evaluation was performed in *OriginPro 9*.

## 2. Additional data

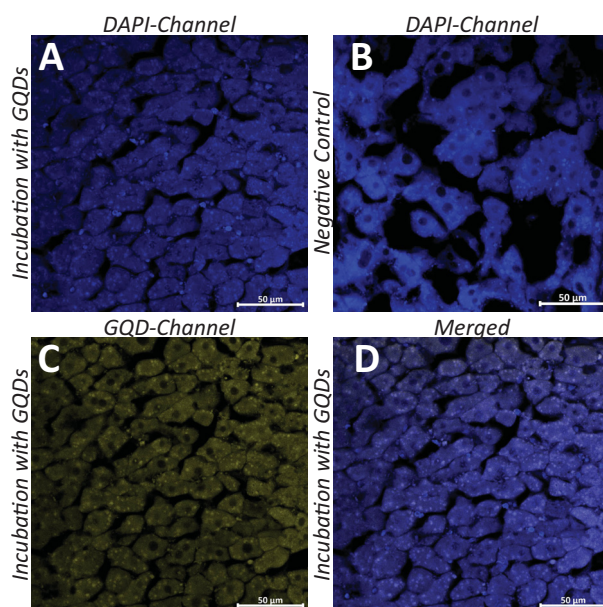


Figure S1: Confocal microscopy images of an incubated PCLS showing the GQDs fluorescence in (A) the DAPI channel, (C) the GQD channel and (D) the merged image of both channels. A control is shown in (B). The hepatocytes' nuclei are omitted from the fluorescence signal. This indicates, that the applied GQDs are at least not taken up into the hepatocyte nuclei, an effect observed before when analyzing breast cancer cell lines and primary cells.



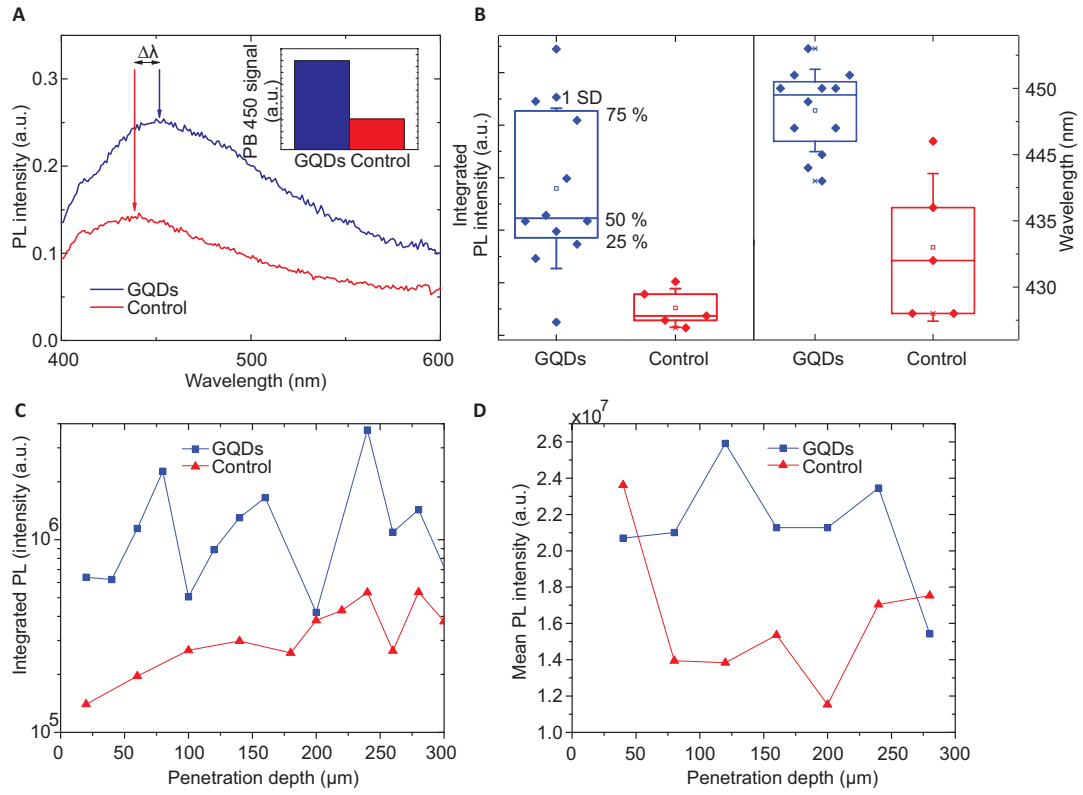


Figure S2: (A) Fluorescence intensity signals of PCLS cultivated with and without GQDs. The PCLS were dissolved *in toto* and measured by fluorescence spectroscopy. The inset shows the mean fluorescence intensities obtained by flow cytometry analysis. (B) Statistical analysis of the standardized integrated fluorescence intensity (left) and the wavelength of maximum fluorescence intensity for GQD incubated and control group dissolved liver fine slices (right). (C) GQD uptake into consecutive layers of PCLS displayed by integrated fluorescence intensities of cell suspensions as measured by fluorescence spectroscopy and (D) mean fluorescence intensity of single cells as measured by flow cytometry.

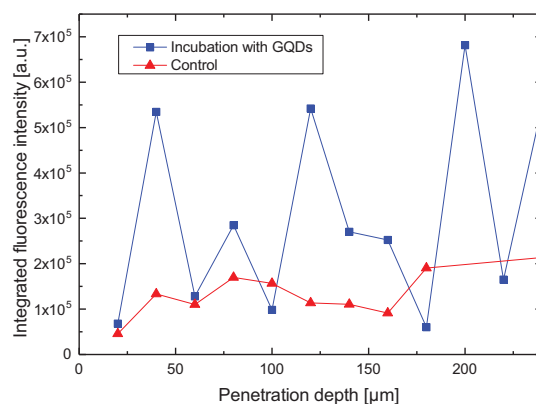


Figure S3: GQD uptake into the depth of MMTV-PyMT tissue displayed by integrated fluorescence intensities of cell suspensions.

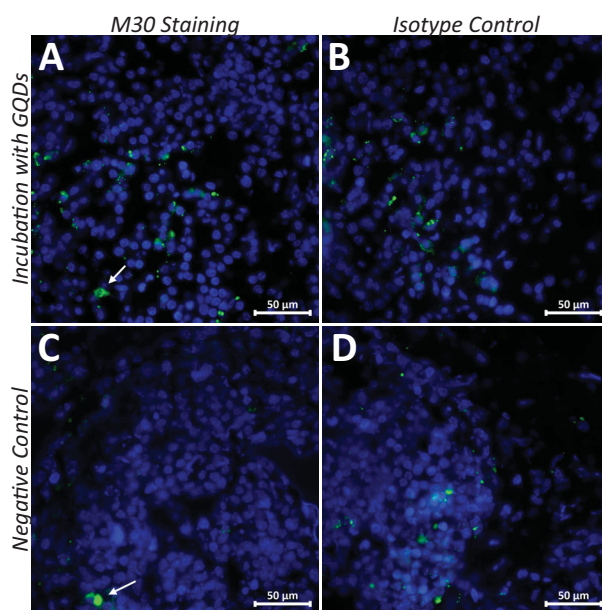


Figure S4: M30 staining and isotype control of MMTV-PyMT tissue slices incubated with GQDs (A and B) and without GQDs (C and D).

## References

- [1] D. Qu, M. Zheng, J. Li, Z. Xie, Z. Sun, Tailoring color emissions from n-doped graphene quantum dots for bioimaging applications, *Light: Science and Appl.* 4 (2015) e364.
- [2] F. A. Steudel, C. J. Mohr, B. Stegen, H. Y. Nguyen, A. Barnert, M. Steinle, S. BeerHammer, P. Koch, W. Lo, W. Schroth, R. Hoppe, H. Brauch, P. Ruth, S. M. Huber, R. Lukowski, Sk4 channels modulate  $ca^{2+}$  signalling and cell cycle progression in murine breast cancer, *Molecular Oncology* 11 (9) (2017) 1172–1188.

- [3] C. T. Guy, R. D. Cardiff, W. J. Muller, Induction of mammary tumors by expression of polyomavirus middle t oncogene: a transgenic mouse model for metastatic disease., *Molecular and Cellular Biology* 12 (3) (1992) 954–961.
- [4] I. A. M. de Graaf, P. Olinga, M. H. de Jager, M. T. Merema, R. de Kanter, E. G. van de Kerkhof, G. M. M. Groothuis, Preparation and incubation of precision-cut liver and intestinal slices for application in drug metabolism and toxicity studies, *Nat. Protocols* 5 (9) (2010) 1540–1551.

---

# **The Low Toxicity of Graphene Quantum Dots is Reflected by Marginal Gene Expression Changes of Primary Human Hematopoietic Stem Cells**

## **Reference**

S. Fasbender, L. Zimmermann, R. P. Cadeddu, M. Luysberg, B. Moll, C. Janiak, T. Heinzl and Rainer Haas, *Scientific Reports* **9**, 1 (2019), Published by Nature Publishing Group.

<https://doi.org/10.1038/s41598-019-48567-6>

## **Copyright statement**

This article is licensed under a Creative Commons Attribution 4.0 International License, which permits use, sharing, adaptation, distribution and reproduction in any medium or format, as long as you give appropriate credit to the original author(s) and the source, provide a link to the Creative Commons license, and indicate if changes were made. The images or other third party material in this article are included in the article's Creative Commons license, unless indicated otherwise in a credit line to the material. If material is not included in the article's Creative Commons license and your intended use is not permitted by statutory regulation or exceeds the permitted use, you will need to obtain permission directly from the copyright holder. To view a copy of this license, visit <http://creativecommons.org/licenses/by/4.0/>.

## **Contributions**

I participated in the planning and the conductance of the experiments and contributed to manuscript writing.

OPEN

# The Low Toxicity of Graphene Quantum Dots is Reflected by Marginal Gene Expression Changes of Primary Human Hematopoietic Stem Cells

Stefan Fasbender<sup>1</sup>, Lisa Zimmermann<sup>1</sup>, Ron-Patrick Cadeddu<sup>2</sup>, Martina Luysberg<sup>3</sup>, Bastian Moll<sup>4</sup>, Christoph Janiak<sup>4</sup>, Thomas Heinzel<sup>1</sup> & Rainer Haas<sup>2</sup>

Graphene quantum dots (GQDs) are a promising next generation nanomaterial with manifold biomedical applications. For real world applications, comprehensive studies on their influence on the functionality of primary human cells are mandatory. Here, we report the effects of GQDs on the transcriptome of CD34<sup>+</sup> hematopoietic stem cells after an incubation time of 36 hours. Of the 20 800 recorded gene expressions, only one, namely the selenoprotein W, 1, is changed by the GQDs in direct comparison to CD34<sup>+</sup> hematopoietic stem cells cultivated without GQDs. Only a meta analysis reveals that the expression of 1171 genes is weakly affected, taking into account the more prominent changes just by the cell culture. Eight corresponding, weakly affected signaling pathways are identified, which include, but are not limited to, the triggering of apoptosis. These results suggest that GQDs with sizes in the range of a few nanometers hardly influence the CD34<sup>+</sup> cells on the transcriptome level after 36 h of incubation, thereby demonstrating their high usability for *in vivo* studies, such as fluorescence labeling or delivery protocols, without strong effects on the functional status of the cells.

A wide variety of nanomaterials has been introduced into our daily life to improve the properties of consumer products like clothes<sup>1</sup>, food<sup>2</sup> and cosmetics<sup>3</sup>. Despite a large body of studies, their potential influence on health is often poorly understood<sup>4,5</sup>. After its discovery in 2004, graphene has gained much attention as a novel two dimensional nanomaterial<sup>6</sup>. Due to its superior mechanical, chemical and electronic properties<sup>7</sup>, many graphene containing consumer products have emerged in the packaging and sports industry<sup>8,9</sup>.

Graphene quantum dots (GQDs) are a nanometer-sized derivative of one or a few layers of graphene. Because of their large surface to mass ratio, they are a fluorescent nanomaterial with a broad spectrum of applications in the field of organic photovoltaic devices, catalysis, sensors and biomedicine<sup>10</sup>. In particular, the field of biomedicine offers many opportunities as GQDs enter the cytoplasm not only of human cell lines, but also of primary human blood cells, without significant effects on cell viability<sup>11–15</sup>. Therefore, GQDs have been used in research related to long term and deep tissue imaging, cancer diagnostics, intracellular sensing and drug delivery<sup>16–21</sup>. As far as the exposure of human cells *in vitro* or *in vivo* to GQDs is concerned, their possible side effects on the functionality of these cells remain a question of ongoing research. For instance, *in vivo* studies show that high doses of GQDs disrupt the progression of embryonic development in zebrafish<sup>22</sup>. In mice, intravenously injected larger graphene nanosheets induced Th2 inflammatory responses<sup>23</sup>. *In vitro* studies using fibroblast cell lines show increased expression of p53, Rad51 and OGG1 proteins, indicating DNA damage caused by GQDs of 40 nm diameter<sup>24</sup>. The toxicity of graphene based nanomaterials thus appears to be mainly related to particle size, surface functional groups, oxygen content, surface charges and impurities, while the formation of reactive oxygen

<sup>1</sup>Condensed Matter Physics Laboratory, Heinrich-Heine-University, D-40204, Düsseldorf, Germany. <sup>2</sup>Department of Haematology, Oncology and Clinical Immunology, Heinrich-Heine-University, D-40204, Düsseldorf, Germany. <sup>3</sup>Ernst Ruska Centre, Jülich Research Centre, D-52425, Jülich, Germany. <sup>4</sup>Institute for Inorganic Chemistry and Structural Chemistry, Heinrich-Heine-University, D-40204, Düsseldorf, Germany. Correspondence and requests for materials should be addressed to T.H. (email: [Thomas.Heinzel@hhu.de](mailto:Thomas.Heinzel@hhu.de)) or R.H. (email: [Haas@med.uni-duesseldorf.de](mailto:Haas@med.uni-duesseldorf.de))

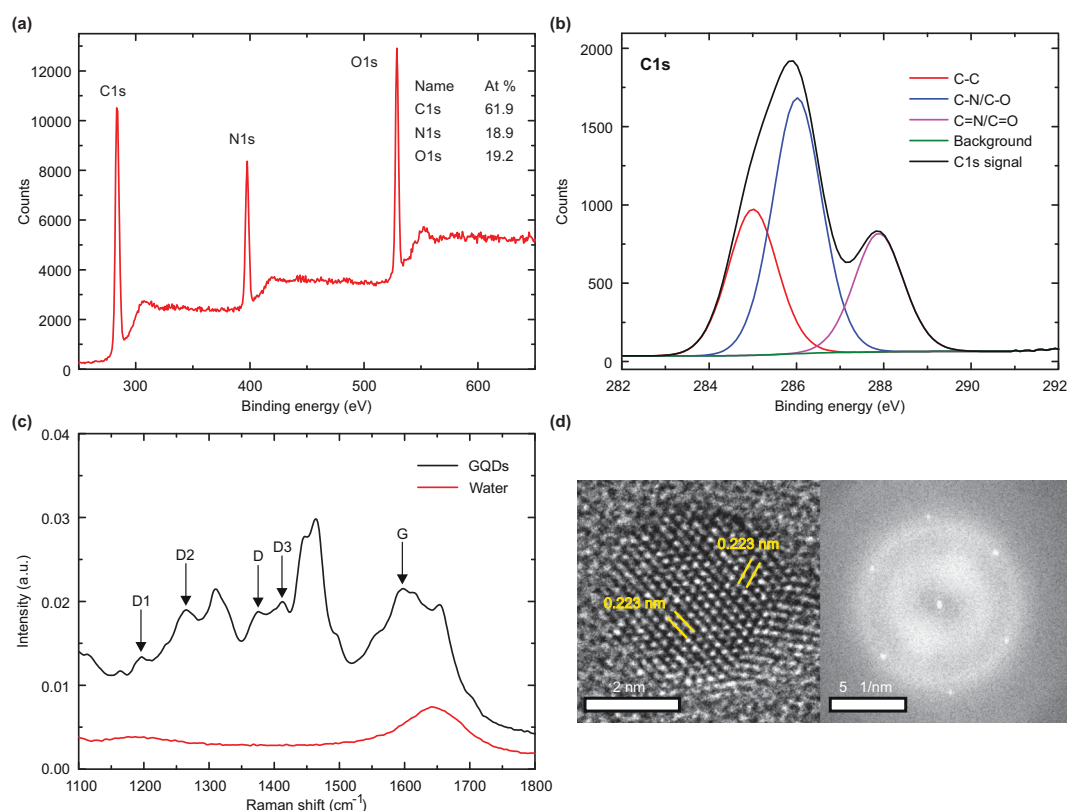


**Figure 1.** (a) Survey XPS spectrum of the GQDs quantifying the amount of C (61.9%), N (18.9%) and O (19.2%). (b) C1s XPS spectrum of the GQDs revealing C-C, C-O and C-N bonds. (c) Raman spectrum of the GQDs dispersed in water (black trace) and of water (red trace). (d) HRTEM image (left) of one GQD and the corresponding Fast Fourier Transform (right).

species (ROS) seems to be the most common underlying mechanism<sup>25</sup>. However, these toxicity studies reported hitherto are no more than a glimpse of the overall, possibly quite complex, responses of the cells to the incubation with GQDs. In particular, nothing is known about the underlying signaling pathways. As has been pointed out recently, a more comprehensive picture requires a gene expression analysis, carried out on primary human cells instead of cell lines<sup>26</sup>.

In the study presented here, we report the cellular gene expression and the attributed signaling pathways after incubation of primary human CD34<sup>+</sup> hematopoietic stem cells (HSCs) with a high concentration (500  $\mu\text{g ml}^{-1}$ ) of GQDs for an exposure time of 36 hours. HSCs are particularly susceptible to any kind of cytotoxic effects such as conventional chemotherapy or radiation. They are composed of the most primitive hematopoietic stem cells as well as the more committed progenitor subset, which is responsible for the lifelong production of mature blood cells.

## Results and Discussion

**Preparation and characterization of the graphene quantum dots.** The GQDs were prepared by pyrolysis of citric acid, following a modified version of the well-established recipe of Qu *et al.*<sup>27</sup> using a well-defined microwave assisted hydrothermal synthesis process. Before their application to the cells, the GQDs underwent a targeted characterization to determine their chemical composition and size as well as their fluorescence properties. They consist of 40% C, 19% N and 8% H (mass fraction) as determined by CHN chemical elemental analysis. The remaining fraction can be assigned to O, as the GQDs consist of no other elements. This was confirmed by X-ray photoelectron spectroscopy (XPS) (Fig. 1(a)). Further analysis of the C1s resonance (see Fig. 1(b)) indicates that C-C bonds amount to 29% of the carbon bonds, while the remaining bonds are approximately equally distributed among C-O and C-N bonds, which is confirmed by the N1s and O1s spectra (Fig. S1). The XPS analysis thus proves that nitrogen compounds, an essential ingredient for the anticipated fluorescence at long wavelengths, have been incorporated into the GQDs.

The Raman spectra of the water-dispersed GQDs (Fig. 1(c)) show some functional groups from citric acid and diethylentriamine (DETA), which is in good agreement with the XPS analysis. Raman signals at 1657, 1411, 1053, 943 and 785  $\text{cm}^{-1}$  match with vibrations of citric acid. Signals at 1463, 1309 and 1091  $\text{cm}^{-1}$  match with diethylentriamine vibrations (see Fig. S2). We can also assign signals at 2946 and 2976  $\text{cm}^{-1}$  to vibrations of citric acid and DETA. Two bands are visible at 1375 and 1596  $\text{cm}^{-1}$  which we assign to the D and G band signals known for graphene quantum dots<sup>28</sup>. Furthermore, there are peaks at 1195, 1264 and 1412  $\text{cm}^{-1}$  labeled D1, D2 and D3, which can be assigned to sp<sup>2</sup>-sp<sup>3</sup> carbon, COOH/C-OH and C=O/C-O edge functional groups, respectively<sup>29</sup>.

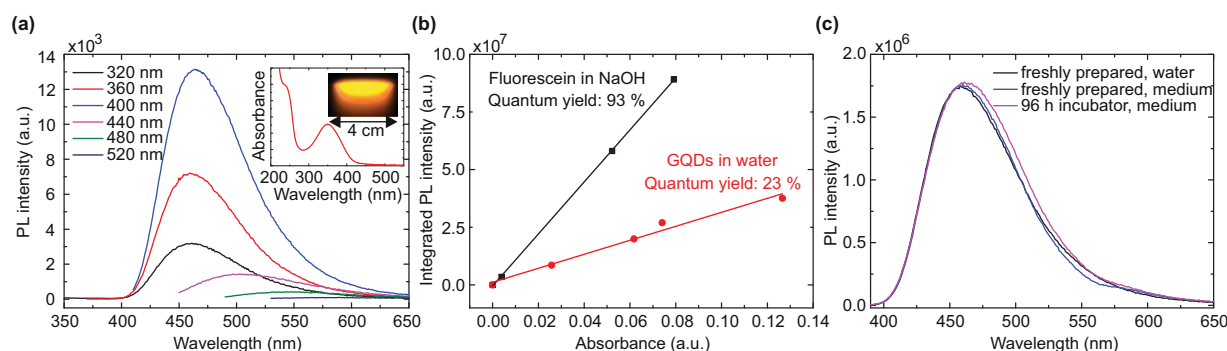


**Figure 2.** (a) Fluorescence spectra of the quantum dots as a function of the excitation wavelength. The corresponding absorbance spectrum including an image of the GQD solution under excitation with blue light is shown in the inset. (b) Integrated PL intensity vs. absorbance of fluorescein and GQDs to determine the GQD quantum yield of 23% at 360 nm excitation. (c) Comparison of the fluorescence spectrum of freshly prepared GQDs and GQDs stored for 96 h in the incubator in a humidified atmosphere at 5% CO<sub>2</sub> and 37 °C dissolved in cell culture medium at 360 nm excitation.

This indicates that the C-C part of the C1s XPS peak is composed of both sp<sup>2</sup> and sp<sup>3</sup> hybridized carbon. A detailed comparison of the Raman spectra of GQDs, DETA, citric acid and water is shown in Fig. S2.

For high resolution transmission electron microscopy (HRTEM) the GQDs were dispersed on an ultrathin amorphous graphite substrate. On a larger scale (see Fig. S3(a)), the GQDs appear as randomly distributed, dark spots. The size histogram indicates an average diameter of 3.3 nm with a full width at half maximum of 0.6 nm (see inset of Fig. S3(a)). Atomic resolution was observed only for a few GQDs, which had an appropriate orientation with respect to the substrate plane. A typical result is shown in the left part of Fig. 1(d), where a hexagonal structure with a lattice constant of 0.223 nm was found, which is 10% smaller than the lattice constant of graphene (0.246 nm). More generally, we observed particles with hexagonal symmetry and lattice constants in the range between 0.21 nm and 0.25 nm, in good agreement with the values published earlier<sup>27,30</sup>. This is also in line with the observation that the lattice constant of graphene decreases as other types of atoms are attached<sup>31</sup>. The fuzzy edge may indicate the presence of defects and/or functional groups, in qualitative agreement with the XPS analysis. The Fast Fourier transform (FFT) in the right part of Fig. 1(d) confirms a crystalline structure with a six-fold symmetry, while the X-ray diffraction (XRD) pattern of the GQDs (Fig. S3(b)) shows a broad peak around 22° that is usually observed for GQDs<sup>28,32,33</sup> and two distinct peaks at 21.9° and 26.2° that can be assigned to elemental carbon and graphite<sup>34</sup>. We also performed topographical measurements with an atomic force microscope (AFM) (see Fig. S4). Particle heights between 1 nm and 2 nm are measured, which is in agreement with results reported earlier for two and three layers of graphene. Based on these findings, we conclude that our GQDs have a disk-like, flat shape, consist mostly of carbon, with equal contents of oxygen and nitrogen and have a predominantly hexagonal crystal structure.

The relevant fluorescence properties of the GQDs are summarized in Fig. 2. As the excitation wavelength is increased from 320 nm to 400 nm, the shape and maximum of the emission spectrum (at a wavelength of 460 nm) remains almost unchanged, while the emission intensity increases by a factor of approximately 4. A further increase of the excitation wavelength causes an abrupt change of the emission spectrum to larger emission wavelengths, accompanied by a marked decrease of the fluorescence intensity. For example, at an excitation wavelength of 480 nm, the maximum of the emission spectrum occurs at 560 nm, thereby showing that the fluorescence mechanisms depend on the excitation wavelength. Qu *et al.*<sup>27</sup> have attributed the excitation that leads to the fluorescence in the blue and belongs to the absorbance peak around 350 nm (inset) to the n-π\* transition of C=O, whereas that one that causes the fluorescence in the yellow was attributed to the n-π\* transition of the N state. In the experiments reported below, we used the emission at larger wavelength, thereby avoiding irradiation of the cells by UV light and remaining compliant with most medical devices using fluorescence detection. The quantum yield of the GQDs at the absorbance maximum of 360 nm was determined to be 23% (Fig. 2(b)). Furthermore, neither the fluorescence spectrum of the GQDs nor its intensity changed significantly over a time period of 96 h when they were dissolved in cell culture medium and stored in the incubator in a humidified atmosphere at 5% CO<sub>2</sub> and 37 °C (Fig. 2(c)).

**Cultivation of CD34<sup>+</sup> cells and GQD uptake.** Using the magnetic cell separation technology for the enrichment of CD34<sup>+</sup> cells from leukapheresis products of healthy donors, we obtained populations with a purity of at least 90% as measured by flow cytometry (Fig. 3(a)). For the cultivation of the stem and progenitor cells, we used Stem SPAN<sup>™</sup> SFEM II medium combined with Stem SPAN<sup>™</sup> CD34<sup>+</sup> Expansion Supplement, a specific medium favoring self-renewal rather than differentiation. As a result, the decrease in the proportion of CD34<sup>+</sup> cells following 36 h of cultivation was marginal with a significant reduction only after 90 h, see Fig. 3(b,c). A broadening of the population regarding size and granularity, see the FSC and SSC data in Fig. 3(c), reflects the distinct alteration of the cells as well. The time-dependent changes observed within the CD34<sup>+</sup> cell populations were identical to those when the cells were cultivated in the presence of GQDs at a concentration of 500 μg ml<sup>-1</sup> as shown in Fig. S5.



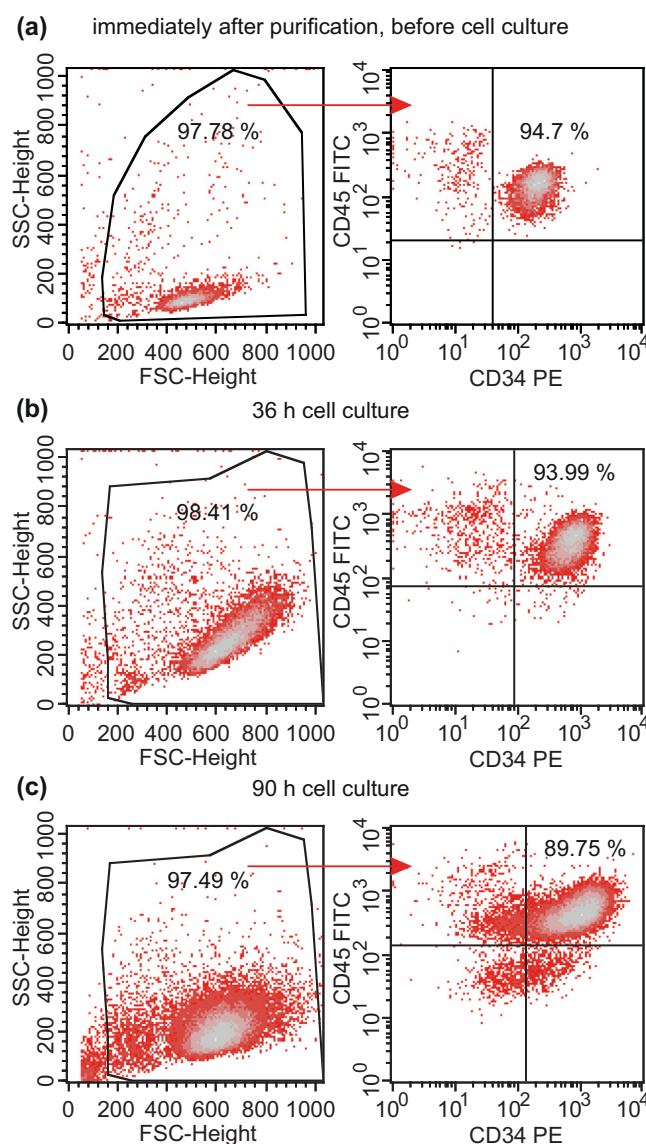


**Figure 3.** Fraction of CD34<sup>+</sup> following selection using anti-CD34 MoAb coated immunomagnetic beads at time point 0 (a), after 36 h (b) and after 90 h of cell culture (c). Viable cells were gated using a forward scatter (FSC) vs side scatter (SSC) plot. The fraction of CD34<sup>+</sup> cells was obtained in a CD34 vs CD45 plot based on all viable cells.

To visualize the uptake of the GQDs into the cells, we performed confocal fluorescence microscopy on living CD34<sup>+</sup> cells, that were stained with Hoechst 33342 for representation of the nuclei. A representative example is given in Fig. 4(a), where the fluorescence images of the cells and the merged bright field images, representing the Hoechst 33342 channel (405 nm excitation, 410–495 nm emission) in blue and the GQD channel (488 nm excitation, 495 nm–630 nm emission) in red, are depicted. The GQDs appear purple as they also emit in the Hoechst 33342 channel. Distinct areas of purple color were observed only in the population cultured in the presence of GQDs. The spatial distribution of the fluorescence intensity implies that the GQDs accumulate in regions near the nucleus. Earlier work suggests that the GQDs are confined to lysosomes<sup>35</sup>. Also, an accumulation of the GQD fluorescence at the Golgi apparatus has been reported recently<sup>36,37</sup>. As a result of the cellular uptake, a time dependent shift of the fluorescence intensity emerging from the cells, as measured by flow cytometry, was observed, with an increase of the median from 8.3 (36 h without GQDs) to 31.3 (36 h with GQDs) and a maximum value of 51.4 following 90 h of incubation with GQDs (Fig. 4(b,c)). Notably, the autofluorescence intensity of the cells cultured without GQDs increased by more than a factor of two during that time, namely from a median value of 8.3 to 17.0. Taking into account the observed changes of the CD34<sup>+</sup> cell population and the decrease of the CD34<sup>+</sup> proportion after 90 h, we opted for a cultivation time of 36 h for the gene expression analysis.

**Gene expression analysis.** In order to assess the effect of GQDs on the transcriptome, we isolated the CD34<sup>+</sup> cells of four healthy donors and took one third of the freshly isolated CD34<sup>+</sup> cells aside to extract the RNA using the RNeasy Mini Kit. The remaining cells were cultivated for 36 hours with and without GQDs at a

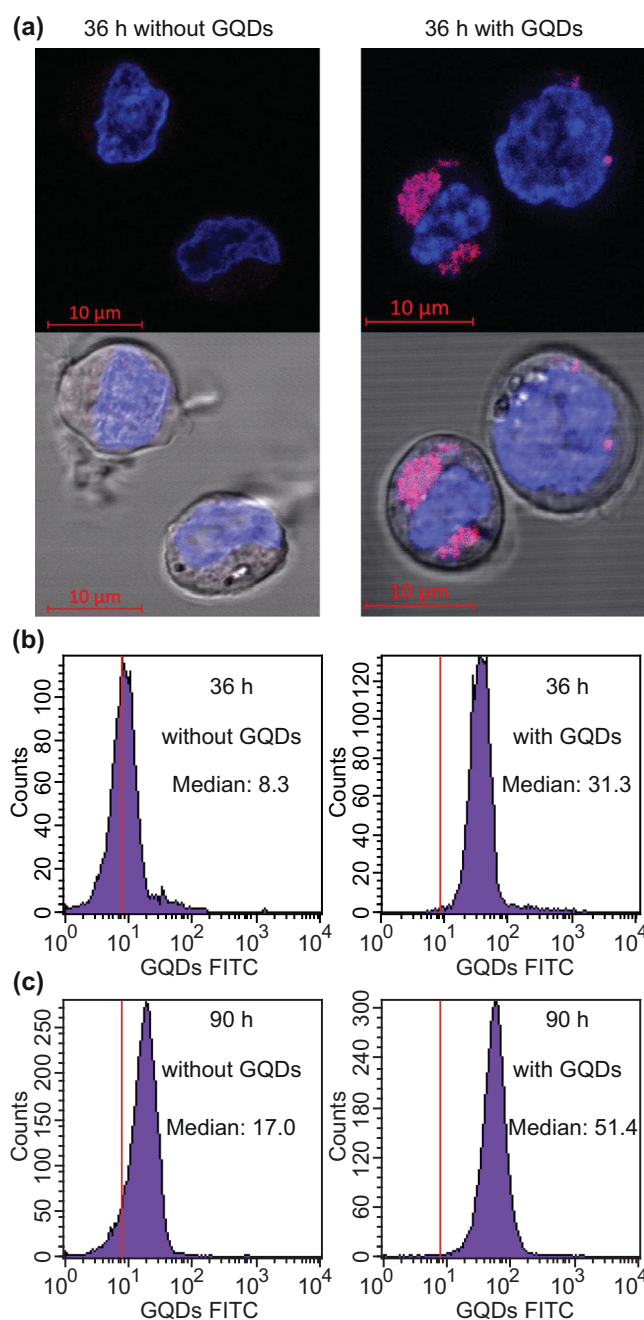


**Figure 4.** (a) Confocal fluorescence microscopy images of living cells cultured for 36 h without GQDs (left) and with GQDs (right) as observed (top row) and merged with the bright field images (bottom row). The stained nuclei are represented in blue while GQDs appear in purple. The fluorescence intensity distributions as determined by flow cytometry after 36 and 90 hours of cultivation are shown in (b,c) respectively. Here, the left parts show the evolution just in the culture medium and the right parts that one in the presence of the GQDs.

concentration of  $500 \mu\text{g ml}^{-1}$ . Independent of the presence of GQDs, we observed a twofold mean increase in the concentration of  $\text{CD}34^+$  cells, demonstrating that the cells underwent one cell cycle on average during the cultivation interval. Afterwards, the RNA of the  $\text{CD}34^+$  cells, cultivated with and without GQDs, was extracted. Using capillary electrophoresis, the RNA integrity of all 12 samples was determined with an average RIN (RNA integrity number) of 9.7, whereby a value of 10.0 implies the highest integrity (see Table S1 for the RIN numbers of all samples). Finally, the RNA was processed for transcriptome-wide gene-level expression profiling on the Clariom<sup>™</sup> S micro array. Using the Transcriptome Analysis Console (TAC) 4.0 software and iPathway guide, we conducted a meta-analysis and compared the measurement results obtained after the  $\text{CD}34^+$  cell cultivation under both conditions, with those observed in  $\text{CD}34^+$  cells before the cells were put into the culture medium, see Fig. 5(a). This kind of comparison strikes us as mandatory, since a comparison restricted to the two culture

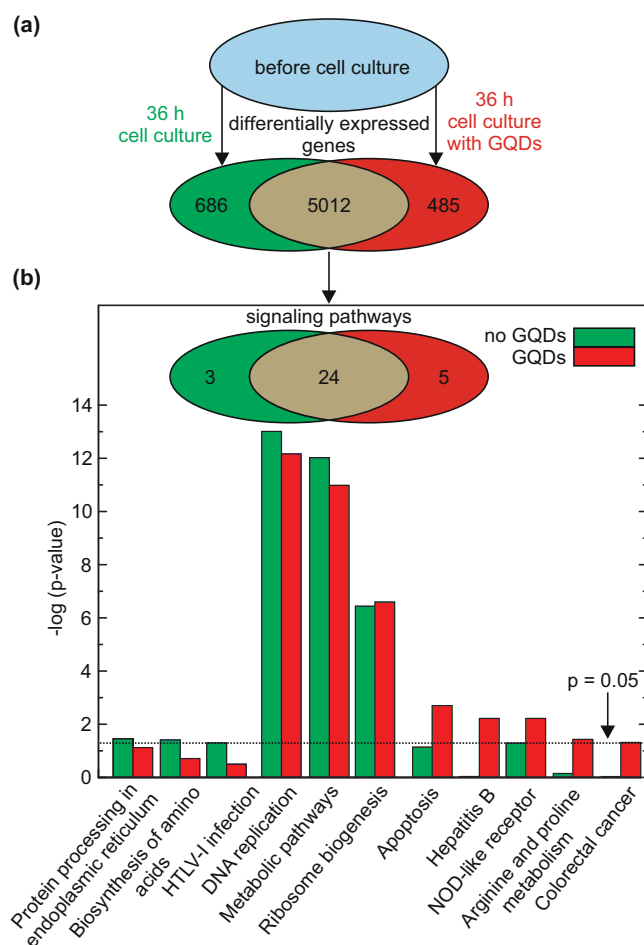


**Figure 5.** Sketch of the design and the result of the gene expression experiment. The transcriptome of the CD34<sup>+</sup> cells was measured before and after exposure of the cells to the two experimental conditions. The modified gene expressions are sorted according to the ratio of their amplification in the presence vs. the absence of the GQDs in the culture. The expression of 5012 genes was changed under both culture conditions, while the expression of 485 genes was only changed in the presence of GQDs and the expression of 686 genes only differed when the CD34<sup>+</sup> cells were cultivated without GQDs. **(b)** Allocation of the changes to 24, 5 and 3 affected signaling pathways, respectively (inset) and the  $-\log p$  - values of the 8 pathways with significant response to the GQDs (main figure). Also shown is the effect on the pathways DNA replication, metabolic and ribosome biogenesis.

conditions directly after the 36 hour cultivation may obscure subtle effects of the GQDs, namely in case of predominant changes related to the cultivation per se. The thresholds for differential expression were (i) an absolute value of the fold change  $>1.5$ , and (ii) a false discovery rate (FDR) - adjusted  $p$ -value  $< 0.05$ , using the Benjamini - Hochberg method<sup>38</sup> to correct for multiple comparisons.

We are not aware of studies regarding the effect of the cell culture on the gene expression of primary human stem cells. Such an effect, however, can be expected since the cells are deprived of their natural environment. Remarkably, the cultivation per se leads to significant changes in the gene expression pattern of 5012 genes, corresponding to 24% of the genes contained within the array. Although the expression of these genes within the CD34<sup>+</sup> cell population has significantly changed following the 36 hour of cultivation under both conditions, the changes induced may differ with regard to their sign as well as their amplitude. Using iPathway guide for a bioinformatic analysis, the changes observed within the transcriptome could be allocated to 24 out of the 320 assignable signaling pathways. For this assessment, we applied the Bonferroni correction to adjust for multiple comparisons. Among the most prominent pathways were those associated with DNA replication and cell metabolism. Albeit interesting in themselves, these effects are not at the focus of the present work and will not be considered in more detail here.

We proceed with the overall assessment of the transcriptome. 485 genes were identified that show significant changes exclusively in the GQD - containing cultures. On the other hand, 686 differentially expressed genes were observed only under culture conditions without GQDs, i.e., these expressions are suppressed by the presence of the GQDs. This corresponds to eight modified signaling pathways. Five of them, namely (1) Apoptosis, (2) Hepatitis B, (3) NOD-like receptor signaling, (4) Arginine and proline metabolism and (5) colorectal cancer,

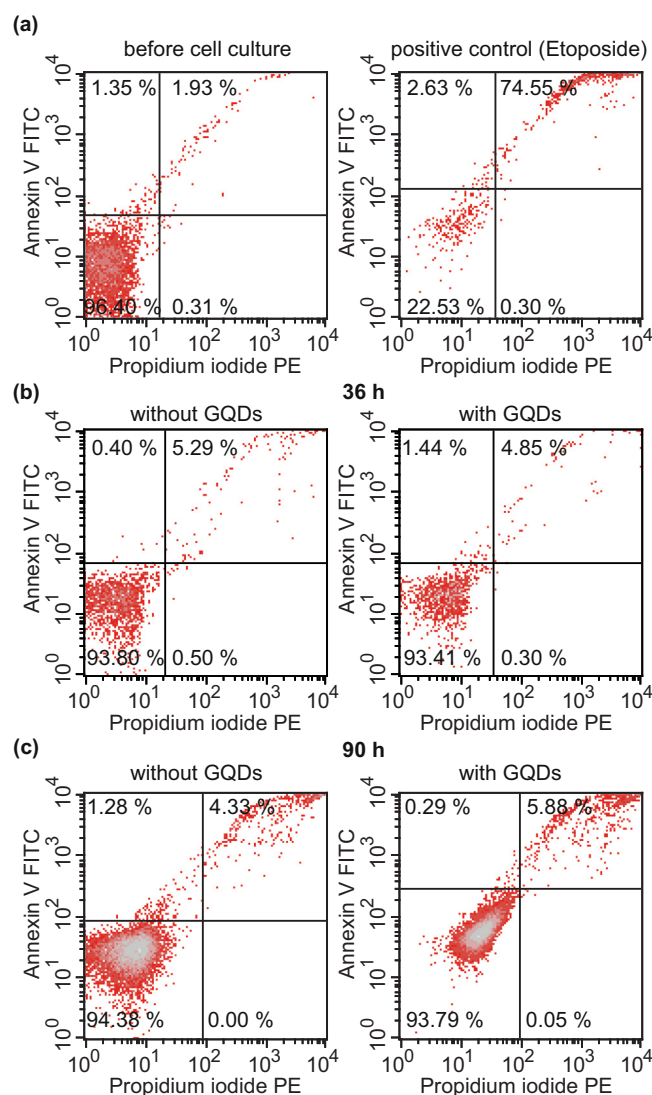


**Figure 6.** Annexin apoptosis assay for (a) untreated CD34<sup>+</sup> cells before cell culture (left) and a positive control using Etoposide as an apoptosis inducing agent (right), (b) CD34<sup>+</sup> cells cultivated for 36 h without (left) and with GQDs (right) and (c) CD34<sup>+</sup> cells cultivated for 90 h without (left) and with GQDs (right). Shown is one representative example out of 3 independent experiments.

showed a change in the presence of the GQDs, while in the remaining three, (6) Protein processing in endoplasmic reticulum, (7) Biosynthesis of amino acids and (8) HTLV-I infection, the changes were suppressed by the GQDs, see Fig. 5(b).

The mere number of affected pathways does not reflect the strength of the GQD related effects. In order to quantify the impact of the GQDs, we determined the negative logarithms of the Bonferroni corrected p-values<sup>39</sup>. We limit our discussion to the eight pathways affected only in one of the two culture conditions, plus the three most prominent pathways affected in both culture conditions. The full set of the 32 pathways is provided in Table S2.

In general, the attribution of the gene expression to the signaling pathways is only qualitative and does not necessarily imply a change of the amplitude of the corresponding cellular processes. Therefore, we selected one of the pathways for an independent, quantitative verification, namely the apoptosis pathway, since it is not only a good measure for cell damage, but also can be tested via the well-established Annexin V/Propidium Iodide assay. As shown in Fig. 6, this pathway got in fact activated in both culture conditions, even though the effect was very small (less than 5%). However, there was no significant difference between the proportions of Annexin expressing CD34<sup>+</sup> cells when the cells were cultivated for 36 h (Fig. 6(b)) in the presence of GQDs compared to those without them. Since it may take longer for the changed gene expression to get translated into apoptosis, we also carried out the assay after 90 h, see Fig. 6(c). Also here, no significant difference between the two culture conditions could be detected. Thus, the significance in the apoptosis pathway is confirmed by the Annexin array, but the p-values difference between the two culture conditions cannot be seen in the direct test.

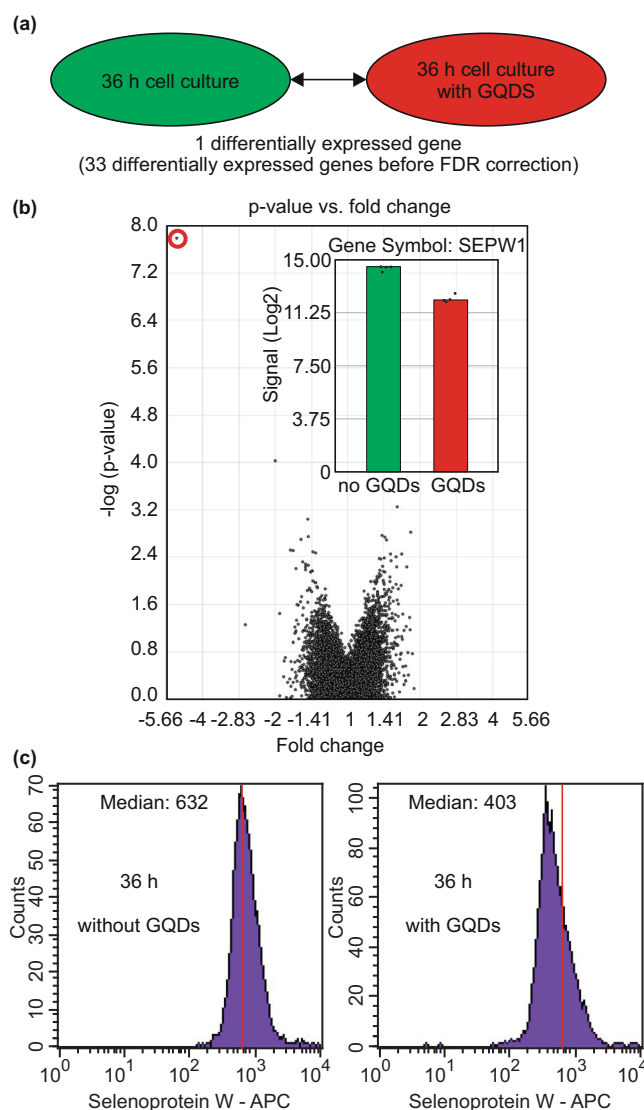


**Figure 7.** (a) Comparison of the transcriptome of CD34<sup>+</sup> cells following cultivation under the two conditions for 36 hours. Only the SEPW1 gene showed a significant differential expression. (b) Volcano plot for all genes (SEPW1 is labeled with a red circle in the upper left corner) and sample signals for the SEPW1 gene (inset). (c) Measurement of the intracellular amount of Selenoprotein W following 36 h of cultivation without GQDs (left) and with GQDs (right).

We proceed by describing the identification of the genes with the highest susceptibility to GQDs and the direct comparison of the CD34<sup>+</sup> cell samples from the two culture conditions. We find 33 genes that meet the criteria required for being regarded as differentially expressed before the FDR correction, namely an absolute value of the fold change larger than 1.5, and a p-value below 0.05, see Table S3 for a comprehensive set of data. 32 of these genes showed only marginal changes with a fold change <2. After the correction using the FDR algorithm, just one gene, namely Selenoprotein W, 1 (SEPW1), showed a significant differential expression according to the criterion given above ( $|\text{fold change}| > 1.5$  and  $\text{FDR} < 0.05$ ).

The SEPW1 gene shows a 5-fold smaller expression level following cultivation in the presence of GQDs as compared to the cultivation in the absence of GQDs. The comparative impact on the expression level of this single gene can be seen in the volcano plot (Fig. 7(a,b)). Since the SEPW1 gene encodes directly the production of the Selenoprotein W, the intracellular amount of this protein after 36 h of cell culture was measured by flow cytometry, using an AF647 conjugated Anti-Selenoprotein W antibody, see Fig. 7(c). A marked decrease of the median fluorescence intensity in the APC channel ( $635 \text{ nm excitation, } 660 \pm 20 \text{ nm emission}$ ) from 632 (without GQDs) to 403 (with GQDs) was observed, thereby verifying the results from the gene expression analysis.

We continue by interpreting these observations in the context of stem cell biology. At the beginning of the incubation experiment, the majority of the CD34<sup>+</sup> cells are in the G1 phase of the cell cycle, while in the bone marrow, significantly more CD34<sup>+</sup>/Ki-67<sup>+</sup> cells are in the S/G2M phase<sup>40</sup>. Being transferred into a liquid culture medium and thereby deprived of their natural microenvironment within the BM niche, they start to proliferate.



This is in line with our observation that following a cultivation period of 36 hours, the cell number doubles approximately, irrespective whether GQDs were present in the medium or not. The expression pattern resembles to some extent that one of CD34<sup>+</sup> cells residing in the bone marrow, in comparison to those circulating in the peripheral blood. For instance, greater cell cycle and DNA synthesis activity of BM-CD34<sup>+</sup> than PB-CD34<sup>+</sup> cells were reflected by the 2- to 5-fold higher expression of nine genes involved in cell cycle progression, eleven genes regulating DNA synthesis and the cell cycle-initiating transcription factor E2F-1<sup>41</sup>.

Among the 5012 common cultivation-related genes, only SEPW1 was significantly modified by the presence of the GQDs, with a strongly reduced expression level. The function of this gene has been shown to be related to the control of cell cycle entry. Hawkes *et al.* identified targets of selenium (Se) in cultured human breast and prostate epithelial cells using gene expression by DNA microarrays<sup>42</sup>. SEPW1 was the only seleno-protein messenger RNA (mRNA) increased by both sodium selenite (specific) and high-Se serum (physiologic). Interestingly, SEPW1 small interfering RNA inhibited G1-phase progression and increased G1-phase gene transcripts, while decreasing S-phase and G2/M-phase gene transcripts. These observations imply cell cycle interruption at the G1/S transition. Along this line of reasoning, our finding could indicate that the cultivation-induced upregulation of SEPW1 is counteracted - similar to the effect of small interfering RNA - by the GQDs with an inhibitory effect on cell cycle progression, i.e., cell division. Still, the effect was not sufficiently strong enough to be translated into a functional effect, as there was no difference in the concentration of CD34<sup>+</sup> cells cultivated in the presence of GQDs or alone. Regarding apoptosis, one report shows that large graphitic flakes with diameters in the range of 300 to 1  $\mu$ m cause apoptosis in red blood cells and in macrophages, most likely through generation of intracellular reactive oxygen species (ROS)<sup>43</sup>, which is in line with earlier studies on skin fibroblasts<sup>44</sup>. GQDs also induced apoptosis and inflammatory reactions in macrophages<sup>45</sup>. In contrast to these reports, we did not detect an increased, GQD - induced apoptosis in the primary human HSCs. Furthermore, none of the other seven modified pathways is readily associated with cellular damage or repair, which speaks against toxicity beyond apoptosis. Interestingly, in some studies the low toxicity appears to be independent of the attached functional groups, as carbon nanodots with various amounts of nitrogen and oxygen do not affect the cell viability in a significant way<sup>28,46</sup>, while in other studies a distinct toxicity of some functional groups is observed<sup>47</sup>.

This small effect of incubated GQDs on the transcriptome of the cells, including triggering of apoptosis, is striking and asks for an explanation. We tentatively interpret this relative inertness by referring to recent reports on the subcellular distribution of GQDs inside cells after incubation. It has emerged that the GQDs are encapsulated in vesicles like lysosomes<sup>35</sup>, which is in tune with the observed accumulation in the periphery of the nucleus (Fig. 3(a)). Thus, it is conceivable that encapsulation not only protects the compartments of a cell from the possible effects of the GQDs but also renders the attached functional units as not very relevant, provided they do not modify the compartmentalization. It should be emphasized that in other publications that report an approximately homogeneous distribution of the GQDs across the cytoplasm, the cells have been fixed, i.e., they are not alive at the time of the imaging. Our confocal fluorescence images rather imply that in living cells, the GQDs accumulate in the periphery of the nucleus, in tune with recent observations<sup>36,37</sup>. Larger GQDs, on the other hand, may be encapsulated to a lesser degree or even damage the cell membrane during incubation. Nevertheless, even though the GQDs appear to be well separated from the cell compartments, GQD - induced drug delivery is achievable, namely regarding applications directly in endosomes or lysosomes, as well as schemes where the drug is released from lysosomes into the nucleus<sup>35</sup>.

The functional relevance of the other differentially expressed genes within the pathways of Arginine and Proline, Colon Cancer, Hepatitis B pathway, protein processing in the endoplasmic reticulum, biosynthesis of amino acids, HTLV I infection and NOD like receptor is, based on the knowledge acquired here, hard to address adequately as they encompass a broad variety of overlapping genes involved in very general cellular processes such as K-RAS, JNK and c-Jun. Such an interpretation would require further, complementary experiments.

## Summary and Conclusions

We examined the *in vitro* effects of small graphene quantum dots (with diameters of approximately 3 nm) on the gene expression of primary human cells, namely blood-derived CD34<sup>+</sup> cells from leukapheresis products of normal donors, after incubation. Surprisingly, of the 20800 genes included in our study, only a single gene is strongly affected, i.e., SEPW1 is downregulated with a fold change of  $-5$ . Even though this downregulation might be related to a slowdown of the cell cycle, this was not reflected in a decreased proliferation. Furthermore, 1170 gene expressions are weakly affected and ascribed to eight signaling pathways. The effect of the GQDs on the transcriptome is markedly weaker than that one of the culture medium, which affects 5012 gene expressions belonging to 24 signaling pathways.

We conclude that our GQDs show only marginal effects on the transcriptome as well as low toxicity. The cells used form a rare hematopoietic stem cell population that is usually residing in the bone marrow, are highly sensitive to environmental disturbances and they may therefore be regarded as a particular sensitive type of cell for studying the effects of GQD exposure. Furthermore, we excluded influences on the results by alterations of the cellular phenotype, since we have concentrated our study on the early stage of cultivation (36 h).

These results are commensurate with recent observations that after incubation, the GQDs are encapsulated by vesicles inside the cell, possibly in relation to the endosomal - lysosomal evolution after uptake of extracellular particles via endocytosis. Possibly, such a compartmentalization protects the cell from possibly toxic effects of the GQDs, irrespective of the functional groups they carry. This situation may be useful for some diagnostic or therapeutic applications, while for others, endosomal release, and the corresponding toxicity studies thereafter, would be required.

## Materials and Methods

**Materials.** Citric acid (ACS reagent,  $\geq 99.5\%$ ), Diethylenetriamine (DETA, 99%), L-Glutamine-Penicillin-Streptomycin solution, Dulbecco's Phosphate Buffered Saline (DPBS), Float-A-Lyzer dialysis devices (100–500 Da), human serum albumin, EDTA, Selenoprotein-AF647 antibodies and sterile filters (200 nm) were obtained from VWR and antibodies against CD45-FITC/CD34-PE, CD34-APC and the FITC Annexin V Apoptosis Detection Kit I were purchased from BD biosciences. Stem SPAN™ SFEM II medium, Stem SPAN™ CD34<sup>+</sup> Expansion Supplement (10x) and Lymphoprep™ solution were bought at STEMCELL™ Technologies and microwave reaction vessels were obtained from CEM GmbH. The CD34 MicroBead Kit UltraPure human, MACS LS columns and 30 pre separation filters were purchased from Miltenyi Biotec and the Fix and Perm Kit was bought from Thermo Fisher Scientific. Separation buffer was prepared freshly by supplementing 500 ml DPBS with 1.5 ml 5% human serum albumin and 1.5 ml 50 mM EDTA.

**Synthesis of graphene quantum dots (GQDs).** Fluorescent GQDs were synthesized using the recipe of Qu *et al.*<sup>27</sup> with slight modifications. 210 mg citric acid and 340 mg DETA were placed into a 10 ml microwave reaction vessel and stirred for 10 min. The mixture was heated to 180 °C under constant stirring in the closed and pressure resistant vessel for 2 min using a CEM Discover Microwave Synthesizer. A viscous, dark orange liquid was obtained and dissolved with 10 ml DI water immediately after the cooldown. The aqueous solution was centrifuged with an Eppendorf MiniSpin® at 13400 rpm for 10 minutes to remove insoluble residual. A Float-A-Lyzer dialysis device (MWCO 100–500 Da) was used to remove citric acid and DETA waste as well as the smallest particles by dialyzing 10 ml of the GQD solution against 2 l of DI water for 48 h with one water exchange after 24 h. The obtained pure GQD solution was dried and weighed with a Sartorius A 200S electronic analytical balance.

**Characterization of GQDs.** Photoluminescence properties were measured using a Horiba FluoroMax®-4 spectrofluorometer, which allows for the correction of inhomogeneities in the instrument and detector response as well as differing lamp intensity, and absorbance spectra were taken with an Agilent Cary 4000 spectrophotometer. Thus, the fluorescence intensities are quantitatively comparable. AFM measurements were performed using the tapping mode of a Veeco 3100 with SiO<sub>2</sub> as substrate. XPS data were measured using a PHI 5000 Versaprobe II XPS microprobe instrument with Au as substrate and TEM images were taken with the Titan G3 50-300 PICO<sup>48</sup> on ultra thin amorphous carbon TEM grids. Raman spectra were obtained on a Bruker MultiRAM-FT Raman spectrometer equipped with a ND:YAG-laser (excitation wavelength 1064 nm). GQDs were measured in water dispersion in a mirrored cuvette with a laser power of 950 mW for 5000 scans with a resolution of 4 cm<sup>-1</sup>. Water reference spectra were obtained using the same settings. Solid-state spectra of citric acid were collected at 75 mW for 2500 scans with a resolution of 4 cm<sup>-1</sup>. The diethylenetriamine reference Raman spectrum was measured in an NMR tube at 400 mW for 2500 scans with a resolution of 4 cm<sup>-1</sup>. PXRD patterns were recorded on a Bruker AXS D2 Phaser using Cu-K $\alpha$ 1/ $\alpha$ 2 radiation with  $\lambda = 1.5418 \text{ \AA}$  at 30 kV. Elemental analyses were conducted with a PerkinElmer CHN 2400 Analyzer.

**Collection of CD34<sup>+</sup> primary human hematopoietic stem cells.** Primary human hematopoietic stem cells were collected from leukapheresis products of in total seven healthy individuals who served as HLA-identical donors for an allogeneic blood stem cell transplantation using the common G-CSF conditioning at a dose of 480  $\mu\text{g}$  per day over a period of 5 days. For isolation of mononuclear cells 1 ml of leukapheresis product was diluted with 5 ml DPBS and layered over 15 ml of Lymphoprep™ solution in a 50 ml conical tube for density gradient centrifugation. The tube was centrifuged at 835 g for 20 min at 20 °C without brake. The interphase was collected and layered again on 15 ml of Lymphoprep™ solution in a 50 ml conical tube followed by a second centrifugation at 835 g for 20 min at 20 °C without brake. To obtain a pellet of mononuclear cells the interphase was collected again and washed with 50 ml DPBS followed by 5 min centrifugation at 300 g. For the lysis of red blood cells the pellet was resuspended in 10 ml ammonium chloride solution (pH = 7.4). After 10 minutes the conical tube was stocked up to 50 ml with separation buffer and centrifuged for 5 min at 300 g. The obtained cell pellet was resuspended in 50 ml separation buffer and centrifuged again for 5 min at 300 g. To isolate the CD34<sup>+</sup> hematopoietic stem cells from other mononuclear cells the pellet was resuspended in 300  $\mu\text{l}$  separation buffer per 10<sup>8</sup> cells and the obtained cell solution was incubated with 100  $\mu\text{l}$  FcR blocking reagent and 100  $\mu\text{l}$  CD34 MicroBeads UltraPure per 10<sup>8</sup> cells respectively. After 30 minutes of incubation time at 4 °C the cells were washed with 50 ml of separation buffer twice (centrifugation for 5 min at 300 g) and resuspended in 3 ml separation buffer. The LS column with the pre-separation filter on top was placed in the magnetic field of a MidiMACS Separator and rinsed with 3 ml separation buffer, before the cell suspension was applied. Afterwards, unlabeled cells were removed by washing the column twice with 5 ml separation buffer and the column was placed on a 15 ml collection tube. Finally, the labeled cells were flushed out immediately with 7 ml separation buffer by pushing the plunger into the column.

**Cell cultivation of CD34<sup>+</sup> primary human hematopoietic stem cells with GQDs.** Using 24 well plates, CD34<sup>+</sup> primary human hematopoietic stem cells were taken in culture immediately after collection. The culture medium contained 90% Stem SPAN™ SFEM II medium and 10% Stem SPAN™ CD34<sup>+</sup> Expansion Supplement (10x) complemented by 1% L-glutamine-penicillin-streptomycin solution. Per well, 500  $\mu\text{l}$  of cell suspension were dispensed at a concentration of  $4 \times 10^5$  cells/ml. For the culture with GQDs, we dissolved GQDs in culture medium at a concentration of 3 mg ml<sup>-1</sup> and the obtained solution was sterile filtered with a 200 nm filter. 100  $\mu\text{l}$  of the sterile GQD solution were added to all GQD culture wells (leading to a final GQD concentration of 500  $\mu\text{g ml}^{-1}$ ) while the controls received 100  $\mu\text{l}$  pure culture medium. The cultivation took place in a Heracell TM 150i incubator in a humidified atmosphere at 5% CO<sub>2</sub> and 37 °C.



**RNA extraction.** Total RNA was extracted using the Qiagen RNeasy Mini Kit. For lysis, the cells were washed twice with PBS and resuspended in 350 µl RLT buffer (including 1% β-mercaptoethanol). The lysate was given into a QIAshredder column (placed in a 2 ml collection tube) and centrifuged for 2 minutes at 13 000 rpm. After centrifugation, 300 µl Ethanol (70%) were added to the collection tube, the solution was mixed by pipetting and then transferred to an RNeasy spin column (placed in a new 2 ml collection tube) for centrifugation at 10 000 rpm for 15 s. The flow-through was discarded and the spin column placed in a new collection tube. To wash the spin column membrane 350 µl RW1 buffer were added, followed by 15 s centrifugation at 10 000 rpm. For DNase digestion, 10 µl DNase were given to 70 µl RDD buffer and placed into the spin column membrane. After 15 minutes of incubation time at room temperature, 350 µl RW1 buffer were added followed by 15 s centrifugation at 10 000 rpm. The flow was discarded and the spin column was placed in a new collection tube, followed by the addition of 500 µl RPE buffer and subsequent centrifugation for 15 s at 10 000 rpm. Discarding the flow again, the spin column was placed in a new collection tube, 500 µl RPE buffer were added and the solution was centrifuged for 2 minutes at 13 000 rpm. Finally, the spin column was placed in a 1.5 ml collection tube, 30 µl RNase free water were added followed by centrifugation for 1 minute at 10 000 rpm. The eluate contains the RNA and was frozen at −80 °C before further processing.

**Gene expression analysis.** RNA quality evaluation and cDNA microarray experiments were performed according to Affymetrix standard protocols by the Genomics and Transcriptomics Lab (GTL) at the Heinrich-Heine-University Düsseldorf on Clariom S<sup>TM</sup> Assays. The generated CEL files were normalized and analyzed using the Transcriptome Analysis Console (TAC) 4.0 software. P-values were calculated using an eBayes corrected ANOVA followed by correction for multiple testing with the Benjamini-Hochberg method (FDR p-value). The thresholds for differential expression were |fold change| > 1.5 and FDR adjusted p-value < 0.05. Significantly impacted pathways were analyzed using Advaita Bio's iPathwayGuide. This software analysis tool implements the Impact Analysis approach that takes into consideration the direction and type of all signals on a pathway, the position, role and type of every gene as described by Draghici<sup>39</sup>. Adjustment for multiple comparisons using the Bonferroni method was implemented during pathway analysis.

**Flow cytometry.** All flow cytometry measurements were performed with a BD FACSCalibur<sup>TM</sup> flow cytometer. For evaluation, debris was removed by gating the living cells in a forward vs. sideward scatter plot (FSC vs. SSC) and for every sample at least 1 000 cellular events were recorded.

**Assessment of CD34<sup>+</sup> purity and GQD uptake.** Cells with and without GQDs were washed twice with PBS (2 ml, 5 min centrifugation at 300 g). In order to assess the amount of CD34<sup>+</sup> cells, 10<sup>5</sup> cells of every condition were incubated with 10 µl CD45-FITC/CD34-PE antibody for 15 minutes at room temperature in the dark. Cells were washed with PBS again and fixed with 200 µl 0.5% formaldehyde solution before flow cytometry analysis. CD34<sup>+</sup> cells were determined out of a CD45 vs CD34 dot plot. To study the uptake of GQDs into the cells, 10<sup>5</sup> of the washed cells with and without GQDs were fixed with 200 µl 0.5% formaldehyde solution. The fluorescence was measured in the FITC (488 nm excitation, 530 ± 30 nm emission) as well as in the PE (488 nm excitation, 575 ± 26 nm emission) channel, as both channels are in the emission range of the GQDs.

**Annexin V apoptosis assay.** Cells were washed twice with cold PBS and incubated with 2.5 µl CD34-APC antibodies for 15 minutes at room temperature in the dark followed by one washing step. Then they were resuspended in 1x Binding Buffer at a concentration of 1 × 10<sup>6</sup> cells/ml before adding 2.5 µl of FITC Annexin V and PI each per 10<sup>5</sup> cells. After vortexing, the cells were incubated for 15 min at room temperature in the dark. Finally, 400 µl 1x Binding Buffer were added and the samples were measured by flow cytometry immediately.

**Measurement of intracellular Selenoprotein W.** For permeabilization of the cells, the Fix and Perm Kit was used. Cells were washed twice with cold PBS and resuspended in 100 µl fixation reagent. After vortexing, the cells were incubated for 15 min at room temperature in the dark before they were washed with PBS again, followed by incubation with 100 µl permeabilization reagent and 1 µl AF647 conjugated Selenoprotein W antibody for 20 minutes at room temperature in the dark. Finally, the cells were washed with PBS, resuspended in 200 µl 0.5% formaldehyde solution and analysed by flow cytometry.

**Ethical statement.** All experiments were performed in compliance with the relevant laws and institutional guidelines and have been approved by the ethical committee of the Heinrich-Heine-University Düsseldorf (study number 2018-50-FmB). All donors have given their informed consent according to the guidelines of the ethical committee specified above.

## Data Availability

The datasets generated during and/or analysed during the current study are available from the corresponding author on reasonable request.

## References

1. Benn, T., Cavanagh, B., Hristovski, K., Posner, J. D. & Westerhoff, P. The release of nanosilver from consumer products used in the home. *J Environ Qual.* **39**, 1875–1882 (2010).
2. Fröhlich, E. & Roblegg, E. Models for oral uptake of nanoparticles in consumer products. *Toxicology* **291**, 10–17 (2012).
3. Weir, A., Westerhoff, P., Fabricius, L., Hristovski, K. & von Goetz, N. Titanium dioxide nanoparticles in food and personal care products. *Environ. Sci. Technol.* **46**, 2242–2250 (2012).
4. Valsami-Jones, E. & Lynch, I. How safe are nanomaterials? *Science* **350**, 388 (2015).
5. Glisovic, S. *et al.* Emerging technologies and safety concerns: A condensed review of environmental life cycle risks in the nano-world. *Int. J. Environ. Sci. Technol.* **14**, 2301–2320 (2017).

6. Novoselov, K. S. *et al.* Electric field effect in atomically thin carbon films. *Science* **306**, 666–669 (2004).
7. Zhu, Y. *et al.* Graphene and graphene oxide: Synthesis, properties, and applications. *Advanced Materials* **22**, 3906–3924 (2010).
8. Segal, M. Learning from silicon. *Nature* **483**, 43 (2012).
9. Park, M. *et al.* Considerations for safe innovation: the case of graphene. *ACS Nano* **11**, 9574 (2017).
10. Shen, J., Zhu, Y., Yang, X. & Li, C. Graphene quantum dots: Emergent nanolights for bioimaging, sensors, catalysis and photovoltaic devices. *Chem. Commun.* **48**, 3686–3699 (2012).
11. Cao, L. *et al.* Carbon dots for multiphoton bioimaging. *J. Am. Chem. Soc.* **129**, 11318 (2007).
12. Liu, C. *et al.* One-step synthesis of surface passivated carbon nanodots by microwave assisted pyrolysis for enhanced multicolor photoluminescence and bioimaging. *J. Mater. Chem.* **21**, 13163 (2011).
13. Zhu, S. *et al.* Strongly green-photoluminescent graphene quantum dots for bioimaging applications. *Chem. Comm.* **47**, 6858 (2011).
14. Shang, W. *et al.* The uptake mechanism and biocompatibility of graphene quantum dots with human neural stem cells. *Nanoscale* **6**, 5799 (2014).
15. Fasbender, S. *et al.* Uptake dynamics of graphene quantum dots into primary human blood cells following *in vitro* exposure. *RSC Adv.* **7**, 12208–12216 (2017).
16. Liu, Q. & Atrens, A. Strong two-photon-induced fluorescence from photostable, biocompatible nitrogen-doped graphene quantum dots for cellular and deep-tissue imaging. *Corrosion Reviews* **31**, 85 (2013).
17. Zhang, M. *et al.* Facile synthesis of water-soluble, highly fluorescent graphene quantum dots as a robust biological label for stem cells. *J. Mat. Chem.* **22**, 7461 (2012).
18. Al-Ogaidi, I. *et al.* Detection of the ovarian cancer biomarker ca-125 using chemiluminescence resonance energy transfer to graphene quantum dots. *Chem. Commun.* **50**, 1344–1346 (2014).
19. Wu, Z. L. *et al.* A general quantitative ph sensor developed with dicyandiamide n-doped high quantum yield graphene quantum dots. *Nanoscale* **6**, 3868 (2014).
20. Sui, X. *et al.* Graphene quantum dots enhance anticancer activity of cisplatin via increasing its cellular and nuclear uptake. *Nanomedicine: Nanotech., Biol. and Med.* **12**, 1997–2006 (2016).
21. Gong, X. *et al.* Phosphorus and nitrogen dual-doped hollow carbon dot as a nanocarrier for doxorubicin delivery and biological imaging. *ACS Appl. Mater. Interfaces* **8**, 11288 (2016).
22. Wang, Z. *et al.* Toxicity of graphene quantum dots in zebrafish embryo. *Biomed. Environ. Sci.* **28**, 341 (2015).
23. Wang, X., Podila, R., Shannahan, J., Rao, A. & Brown, J. Intravenously delivered graphene nanosheets and multiwalled carbon nanotubes induce site-specific th2 inflammatory responses via the il-33/st2 axis. *Int J Nanomedicine* **8**, 1733–1748 (2013).
24. Wang, D., Zhu, L., Chen, J. & Dai, L. Can graphene quantum dots cause dna damage in cells? *Nanoscale* **7**, 9894 (2015).
25. Guo, X. & Mei, N. Assessment of the toxic potential of graphene family nanomaterials. *Journal of Food and Drug Analysis* **22**, 105–115 (2014).
26. Ou, L. *et al.* Toxicity of graphene-family nanoparticles: A general review of the origins and mechanisms. *Particle and Fibre Toxicology* **13**, 57 (2016).
27. Qu, D., Zheng, M., Li, J., Xie, Z. & Sun, Z. Tailoring color emissions from n-doped graphene quantum dots for bioimaging applications. *Light: Science and Appl.* **4**, e364 (2015).
28. Liu, J. *et al.* One-step hydrothermal synthesis of photoluminescent carbon nanodots with selective antibacterial activity against *porphyromonas gingivalis*. *Nanoscale* **9**, 7135–7142 (2017).
29. Rajender, G. & Giri, P. K. Formation mechanism of graphene quantum dots and their edge state conversion probed by photoluminescence and Raman spectroscopy. *J. Mater. Chem. C* **4**, 10852 (2016).
30. Jin, S. H., Kim, D. H., Jun, G. H., Hong, S. H. & Jeon, S. Tuning the photoluminescence of graphene quantum dots through the charge transfer effect of functional groups. *ACS Nano* **7**, 1239 (2013).
31. Elias, D. C. *et al.* Control of graphene's properties by reversible hydrogenation: Evidence for graphane. *Science* **323**, 610 (2009).
32. Sun, Y. *et al.* Large scale preparation of graphene quantum dots from graphite with tunable fluorescence properties. *Phys. Chem. Chem. Phys.* **15**, 9907 (2013).
33. Chaudhary, S. *et al.* Potential prospects for carbon dots as a fluorescence sensing probe for metal ions. *RSC Adv.* **6**, 90526 (2016).
34. da Costa, R. S. *et al.* An Alternative Route to Obtain Carbon Quantum Dots from Photoluminescent Materials in Peat. *Materials* **11**, 1492 (2018).
35. Wang, Q. *et al.* Hollow luminescent carbon dots for drug delivery. *Carbon* **59**, 192–199 (2013).
36. Yuan, M. *et al.* Optically active blue-emitting carbon dots to specifically target the golgi apparatus. *RSC Adv.* **7**, 49931–49936 (2017).
37. Wang, L. *et al.* Industrial production of ultra-stable sulfonated graphene quantum dots for golgi apparatus imaging. *J. Mater. Chem. B* **5**, 5355–5361 (2017).
38. Benjamini, Y. & Hochberg, Y. Controlling the false discovery rate: a practical and powerful approach to multiple testing. *Journal of the Royal Statistical Society. Series B* **57**, 289–300 (1995).
39. Draghici, S. *et al.* A systems biology approach for pathway level analysis. *Genome research* **17**, 1537 (2007).
40. Fruehauf, S., Veldwijk, M. R., Krämer, A., Haas, R. & Zeller, W. J. Delineation of cell cycle state and correlation to adhesion molecule expression of human cd34+ cells from steady-state bone marrow and peripheral blood mobilized following g-csf-supported chemotherapy. *Stem Cells* **16**, 271–279 (1998).
41. Steidl, U. *et al.* Gene expression profiling identifies significant differences between the molecular phenotypes of bone marrow-derived and circulating human cd34+ hematopoietic stem cells. *Blood* **99**, 2037–2044 (2002).
42. Hawkes, W. C., Wang, T. T. Y., Alkan, Z., Richter, B. D. & Dawson, K. Selenoprotein w modulates control of cell cycle entry. *Biological Trace Element Research* **131**, 229–244 (2009).
43. Qu, G., Wang, X., Wang, Z., Liu, S. & Jiang, G. Cytotoxicity of quantum dots and graphene oxide to erythroid cells and macrophages. *Nanoscale Res. Lett.* **8**, 198 (2013).
44. Liao, K. H., Lin, Y. S., Macosko, C. W. & Haynes, C. L. Cytotoxicity of graphene oxide and graphene in human erythrocytes and skin fibroblasts. *ACS Appl. Mat. Interf.* **3**, 2607–2615 (2011).
45. Qin, Y. *et al.* Graphene quantum dots induce apoptosis, autophagy, and inflammatory response via p38 mitogen-activated protein kinase and nuclear factor-kappa b mediated signaling pathways in activated thp-1 macrophages. *Toxicology* **327**, 62 (2015).
46. Liu, J. *et al.* One-step hydrothermal synthesis of nitrogen-doped conjugated carbonized polymer dots with 31% efficient red emission for *in vivo* imaging. *Small* **14**, 1703919 (2018).
47. Xie, Y. *et al.* Cytotoxicity and autophagy induction by graphene quantum dots with different functional groups. *Journal of Environmental Sciences* **77**, 198–209 (2019).
48. Barthel, J., Houben, L. & Tillmann, K. Fei titan g3 50–300 pico. *JLSRF* **1**, 57 (2015).

## Acknowledgements

We acknowledge financial support by the Heinrich Heine University Düsseldorf. The first author acknowledges financial support of his position by the Düsseldorf School of Oncology (DSO). T.H. acknowledges support by the Betz foundation. Support regarding the XPS analysis by A. Besmehn and H. Hartmann (FZ Jülich), as well as access to the confocal microscope at the Center of Advanced imaging (CAi) of HHU Düsseldorf, is gratefully

acknowledged. The authors thank Sabrina Pechtel for help regarding RNA extraction, J.C. Fischer for providing apheresis products and C. A. M. Seidel for access to the Horiba FluoroMax<sup>®</sup>-4 spectrofluorometer and the Agilent Cary 4000 spectrophotometer.

### Author Contributions

R.H., T.H. and S.F. conceived the ideas, S.F., L.Z. and R.P.C. designed and performed the experiments, M.L. provided the HRTEM images of the GQDs, B.M. and C.J. acquired and analysed the Raman spectra, S.F., L.Z. and R.P.C. analysed the data and T.H., R.H. and S.F. wrote the paper.

### Additional Information

**Supplementary information** accompanies this paper at <https://doi.org/10.1038/s41598-019-48567-6>.

**Competing Interests:** The authors declare no competing interests.

**Publisher's note:** Springer Nature remains neutral with regard to jurisdictional claims in published maps and institutional affiliations.



**Open Access** This article is licensed under a Creative Commons Attribution 4.0 International License, which permits use, sharing, adaptation, distribution and reproduction in any medium or format, as long as you give appropriate credit to the original author(s) and the source, provide a link to the Creative Commons license, and indicate if changes were made. The images or other third party material in this article are included in the article's Creative Commons license, unless indicated otherwise in a credit line to the material. If material is not included in the article's Creative Commons license and your intended use is not permitted by statutory regulation or exceeds the permitted use, you will need to obtain permission directly from the copyright holder. To view a copy of this license, visit <http://creativecommons.org/licenses/by/4.0/>.

© The Author(s) 2019

# Supporting information for: The Low Toxicity of Graphene Quantum Dots is Reflected by Marginal Gene Expression Changes of Primary Human Hematopoietic Stem Cells

S. Fasbender,<sup>†</sup> L. Zimmermann,<sup>†</sup> R.-P. Cadeddu,<sup>‡</sup> M. Luysberg,<sup>¶</sup> B. Moll,<sup>§</sup> C.  
Janiak,<sup>§</sup> T. Heinzl,<sup>\*,†</sup> and R. Haas<sup>\*,‡</sup>

<sup>†</sup>*Condensed Matter Physics Laboratory, Heinrich-Heine-University, D-40204 Düsseldorf,  
Germany*

<sup>‡</sup>*Department of Haematology, Oncology and Clinical Immunology,  
Heinrich-Heine-University, D-40204 Düsseldorf, Germany*

<sup>¶</sup>*Ernst Ruska-Centre, Jülich Research Centre, 52425 Jülich, Germany*

<sup>§</sup>*Institute for Inorganic Chemistry and Structural Chemistry, Heinrich-Heine-University,  
D-40204 Düsseldorf, Germany*

E-mail: thomas.heinzl@hhu.de; Haas@med.uni-duesseldorf.de

The supporting information provides further data regarding the characterization of the graphene quantum dots, the cell experiments and the gene expression analysis.

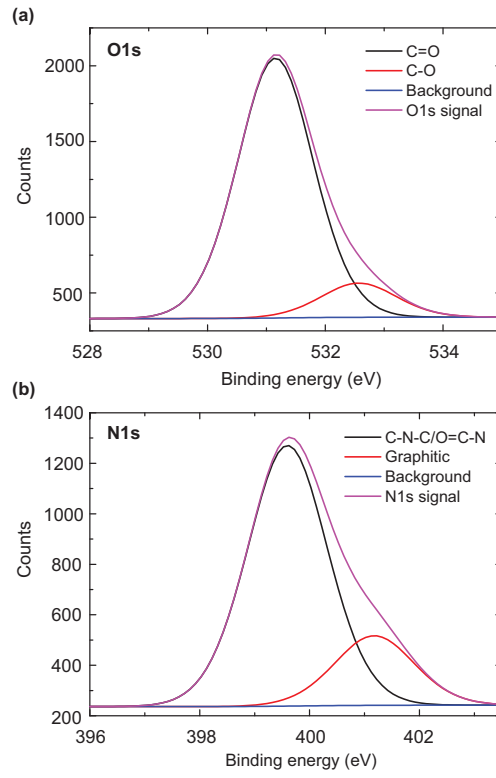


Figure S1: Fine structures of the XPS measurements at our GQDs corresponding to the (a) O1s resonance and (b) N1s resonance.

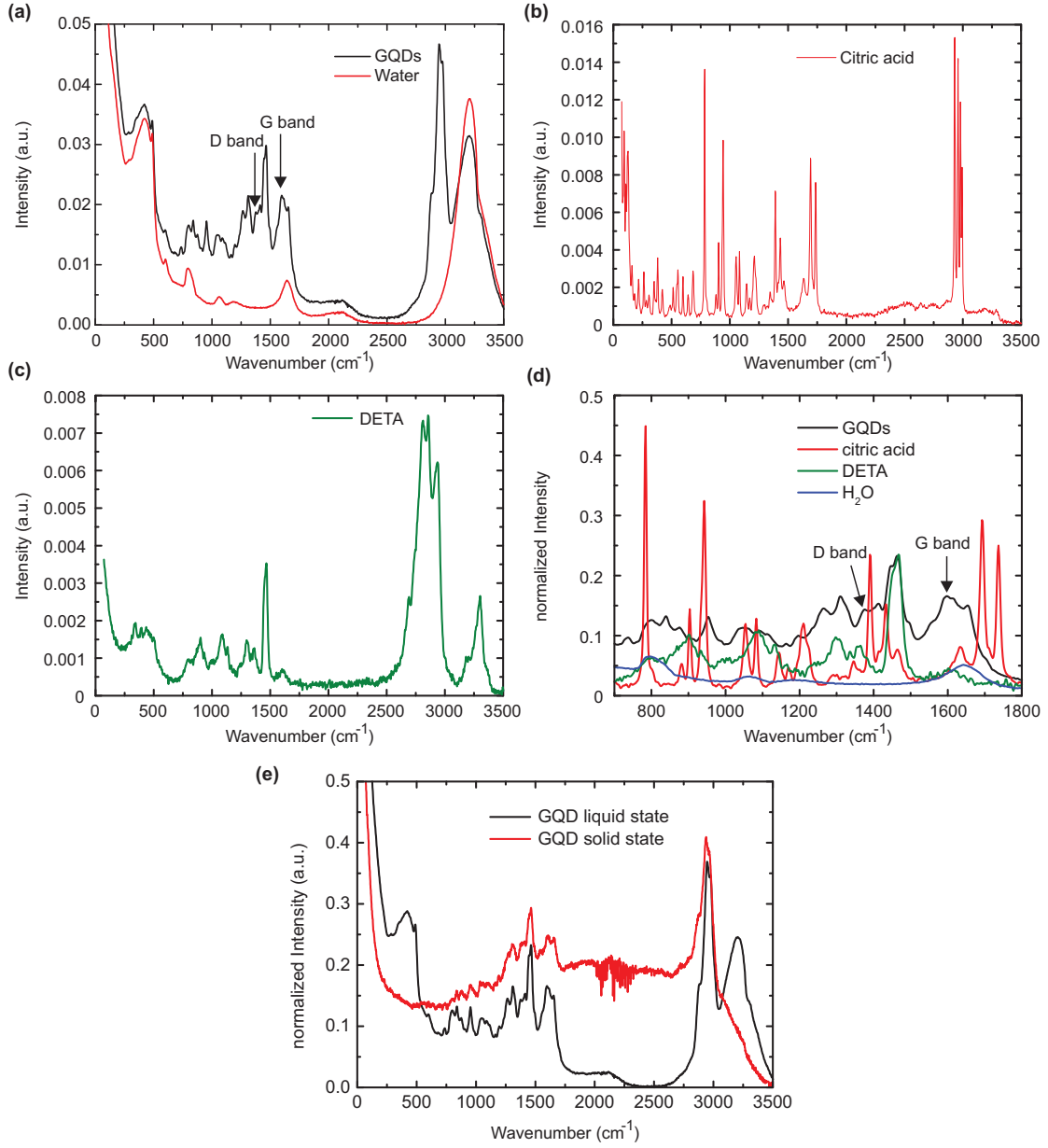


Figure S2: Raman spectra of (a) GQDs and water, (b) citric acid, (c) diethylenetriamine (DETA), (d) a comparison of the spectra of GQDs, citric acid, DETA and water in the selected, relevant region from 700-1800  $\text{cm}^{-1}$  and (e) a comparison of the spectra of dried GQDs and water-dispersed GQDs. Raman signals of the GQDs at 1657, 1411, 1053, 943 and 785  $\text{cm}^{-1}$  match with vibrations of citric acid. Signals at 1463, 1309 and 1091  $\text{cm}^{-1}$  match with diethylenetriamine vibrations. We can also assign signals at 2946 and 2976  $\text{cm}^{-1}$  to vibrations of citric acid and DETA. Two small bands are visible at 1375 and 1596  $\text{cm}^{-1}$  which we assign to the D and G band signals known for graphene quantum dots.



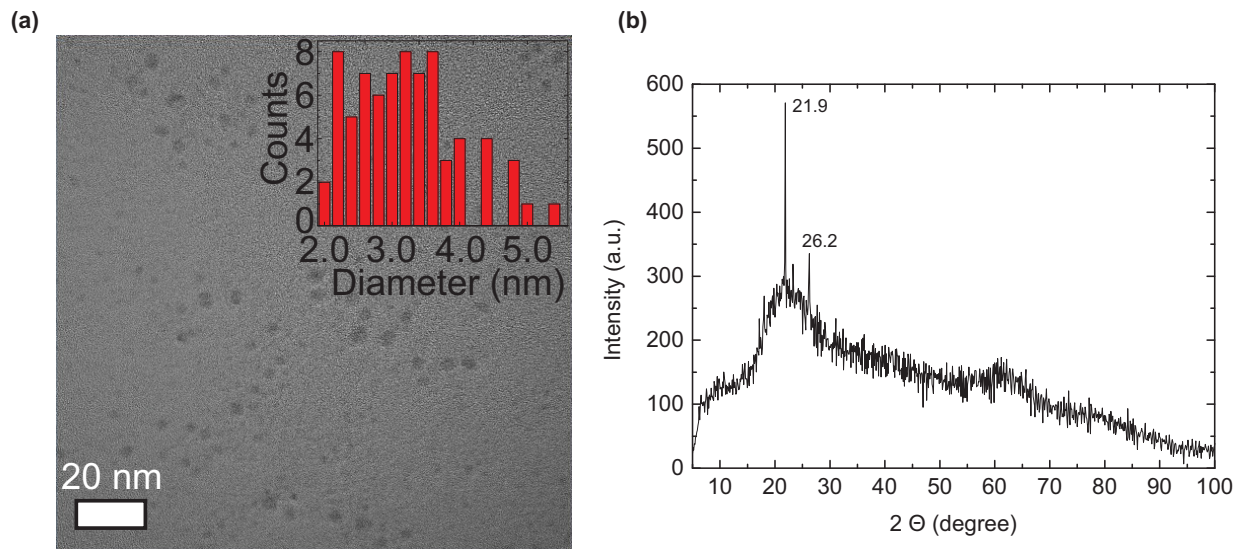


Figure S3: (a) TEM image of the GQDs and the corresponding size histogram (inset) and (b) XRD pattern of the GQDs.

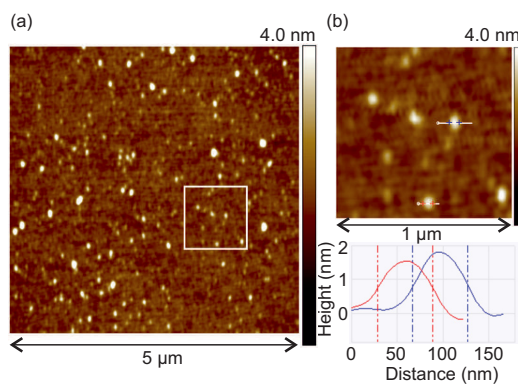


Figure S4: The GQDs deposited on SiO<sub>2</sub> as seen by an atomic force microscope on a larger scale (a) and a zoom with the height profiles of two GQDs (b). The height between 1 nm and 2 nm indicates up to three graphene layers.

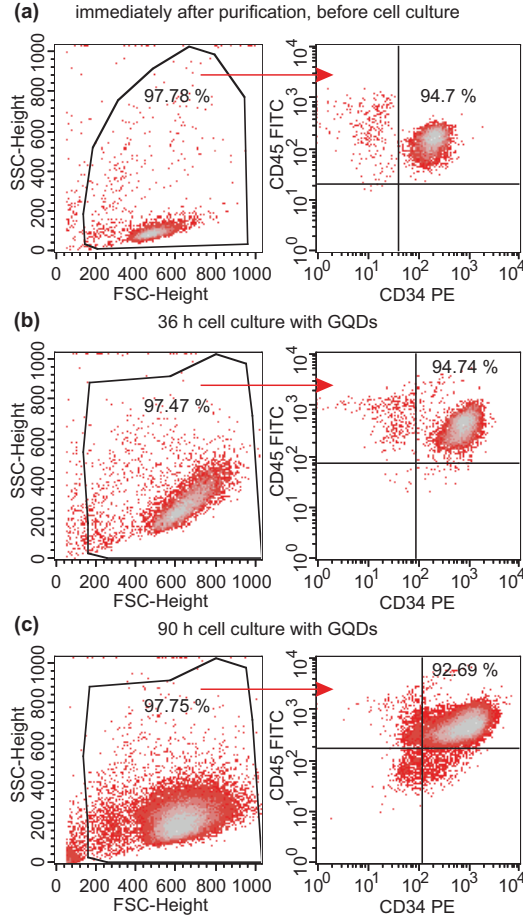


Figure S5: Fraction of  $CD34^{+}$  following selection using anti- $CD34$  MoAb coated immunomagnetic beads at time point 0 (a), after 36 h (b) and after 90 h of cell culture with GQDs (c). Viable cells were gated using a forward scatter (FSC) vs side scatter (SSC) plot. The fraction of  $CD34^{+}$  cells was obtained in a  $CD34$  vs  $CD45$  plot based on all viable cells.

Table S1: RIN numbers and RNA concentraion

Donor	Condition	RNA concentration (ng/ $\mu$ l)	RIN number
1	before cell culture	3.4	9.7
	36 h cell culture	11.5	10.0
	36 h cell culture with GQDs	8.7	10.0
2	before cell culture	7.7	8.8
	36 h cell culture	19.6	10.0
	36 h cell culture with GQDs	9.1	9.9
3	before cell culture	6.8	8.4
	36 h cell culture	17.7	10.0
	36 h cell culture with GQDs	14.9	10.0
4	before cell culture	3.4	9.7
	36 h cell culture	15.6	10.0
	36 h cell culture with GQDs	11.1	10.0

Table S2: Signaling pathways belonging to Figure 4

Pathway name	Bonferroni p-value (36 h with GQDs vs. before cell culture)	Bonferroni p-value (36 h without GQDs vs. before cell culture)
DNA replication	6.83E-13	9.81E-14
Metabolic pathways	1.04E-11	9.42E-13
Ribosome biogenesis in eukaryotes	2.49E-07	3.56E-07
Oxidative phosphorylation	2.32E-05	6.10E-06
Cell cycle	3.52E-05	6.74E-05
Proteasome	3.56E-05	2.43E-05
Fanconi anemia pathway	1.42E-04	1.24E-04
Epstein-Barr virus infection	3.54E-04	4.60E-04
Parkinson's disease	3.94E-04	2.26E-04
Alzheimer's disease	4.81E-04	5.43E-04
Spliceosome	5.77E-04	3.85E-03
Aminoacyl-tRNA biosynthesis	8.03E-04	5.81E-04
Mismatch repair	1.57E-03	4.30E-04
Huntington's disease	1.60E-03	1.55E-03
MicroRNAs in cancer	1.60E-03	2.14E-05
Apoptosis	1.92E-03	7.17E-02
Non-alcoholic fatty liver disease (NAFLD)	1.93E-03	2.01E-02
Nucleotide excision repair	3.00E-03	2.35E-03
Pyrimidine metabolism	3.26E-03	8.65E-04
Homologous recombination	3.59E-03	3.56E-03
RNA transport	3.76E-03	2.67E-03
Hepatitis B	5.72E-03	9.24E-01
NOD-like receptor signaling pathway	6.10E-03	5.12E-02
Citrate cycle (TCA cycle)	1.11E-02	2.47E-02
Cellular senescence	1.72E-02	2.39E-02
Viral carcinogenesis	2.76E-02	4.37E-03
Arginine and proline metabolism	3.67E-02	7.04E-01
Colorectal cancer	4.78E-02	1.00E+00
Purine metabolism	4.80E-02	6.97E-04
Protein processing in endoplasmic reticulum	7.48E-02	3.45E-02
Biosynthesis of amino acids	1.96E-01	3.94E-02
HTLV-I infection	3.14E-01	4.97E-02

Table S3: Gene expression changes belonging to Figure 6

Gene symbol	Fold change	p-value	FDR p-value	Description
SEPW1	-5.14	1.64E-08	4.00E-04	selenoprotein W, 1
FRMD3	-2	9.46E-05	0.9998	FERM domain containing 3
TYRO3	-1.92	0.0357	0.9998	TYRO3 protein tyrosine kinase
LRRCC1	-1.73	0.003	0.9998	Entrez Gene ID(s) 85444
CELF4	-1.68	0.0031	0.9998	CUGBP, Elav-like family member 4
CD53	-1.63	0.0472	0.9998	Memczak2013 ALT_ACCEPTOR,
GNG3	-1.63	0.0256	0.9998	guanine nucleotide binding protein (G protein), gamma 3
KIF2C	-1.6	0.0258	0.9998	kinesin family member 2C
LINC01140	-1.57	0.0229	0.9998	long intergenic non-protein coding RNA 1140
PLEKHA8	-1.56	0.002	0.9998	pleckstrin homology domain containing, family A member 8
ZNF780A	-1.56	0.0187	0.9998	zinc finger protein 780A
NUDT2	-1.54	0.0383	0.9998	nudix hydrolase 2
GAS1	-1.54	0.0048	0.9998	growth arrest-specific 1
KRTAP21-1	-1.53	0.0289	0.9998	keratin associated protein 21-1
AC018462.2;	1.5	0.0035	0.9998	Salzman2013 ANTISENSE, coding
GPR135	1.52	0.0152	0.9998	G protein-coupled receptor 135
ZNF345	1.52	0.0435	0.9998	zinc finger protein 345
HMBS	1.53	0.0422	0.9998	hydroxymethylbilane synthase
ZBED8	1.53	0.0356	0.9998	zinc finger, BED-type containing 8
NBEAL1	1.54	0.0132	0.9998	neurobeachin like 1
LOC100133315;	1.54	0.0222	0.9998	transient receptor potential cation channel subfamily C, member 2-like
RP11-849H4.2				
ZNF582	1.58	0.0378	0.9998	zinc finger protein 582
TNXA	1.59	0.004	0.9998	tenascin XA (pseudogene)
ARAP2	1.59	0.0115	0.9998	ArfGAP with RhoGAP domain
SMC1B	1.59	0.0059	0.9998	structural maintenance of chromosomes 1B
BBS5	1.61	0.0215	0.9998	Bardet-Biedl syndrome 5
ASIC2	1.61	6.00E-04	0.9998	acid sensing ion channel 2
SLC26A11	1.62	0.0246	0.9998	solute carrier family 26 (anion exchanger)
RAI14	1.63	0.0401	0.9998	Entrez Gene ID(s) 26064
KRTAP2-4	1.67	0.012	0.9998	keratin associated protein 2-4
DGKD	1.68	0.0035	0.9998	diacylglycerol kinase, delta 130kDa
BBOF1	1.76	0.0059	0.9998	basal body orientation factor 1
ST8SIA4	1.8	0.0422	0.9998	ST8 alpha-N-acetyl-neuraminide alpha-2,8-sialyltransferase 4

## 4 Conclusions and Outlook

Within this thesis, we studied several aspects of the interaction of GQDs with human cells. The main findings of the presented publications will be briefly summarized here and suggestions for future research will be made.

As a starting point, the uptake dynamics of GQDs into primary human leukocytes and CD34<sup>+</sup> hematopoietic stem cells was studied. A nearly linear time- and concentration dependent uptake was found for all cell types studied. The mean uptake by granulocytes and monocytes is 3.6 and 6.7 times greater compared to lymphocytes. Within the lymphocyte subsets NK cells and B cells incorporate more than twice as much GQDs as compared to T helper and cytotoxic T cells. The uptake of GQDs into CD34<sup>+</sup> hematopoietic stem cells is comparable to the uptake into B and NK cells. The observed differential uptake can not be explained by variations in cell size alone. The results suggest a better incorporation ability of cells capable of phagocytosis but the reason for the differential uptake into the lymphocyte subsets remains unclear. Over a time frame of 36 h the effect of the GQDs on viability of the cells is rather low with a measured viability of 90 % at the highest concentration.

The uptake studies were extended to different breast cancer models. Estrogen receptor positive, progesterone receptor positive, HER2 negative MCF-7 cells show a three times higher uptake compared to triple negative MDA-MB-231 cells as well as MCF-10A cells as a model for non-tumorigenic mammary epithelial cells. Again, the differential uptake can not be explained by cell size alone. Localization of the GQDs via confocal fluorescence microscopy reveals that the GQDs accumulate near the nucleus inside the endolysosomal system, suggesting an uptake via endocytosis. Uptake studies into the closer-to-reality system of murine *ex vivo* precision-cut mammary tumor slices demonstrate a constant uptake into the depth of the tissue without an increase of apoptotic or necrotic cells.

To gain insight into the effects of the GQDs on the cellular function we examined the effect of GQDs on the transcriptome of primary human CD34<sup>+</sup> stem cells by recording the gene expression changes of 20 800 genes. Only one, namely the selenoprotein W, 1 shows a differential expression, to be specific, a downregulation by 80 %. This finding is confirmed by measurements of the intracellular amount



---

of the corresponding protein, the selenoprotein W, which is decreased in cells incubated with GQDs. A meta analysis, that takes into account the more prominent changes just by cell culture reveals 1171 weakly affected genes, that correspond to the following eight pathways: Apoptosis, Arginine and Proline, Colon Cancer, Hepatitis B pathway, protein processing in the endoplasmic reticulum, biosynthesis of amino acids, HTLV I infection and NOD like receptor pathway. The annexin apoptosis assay could not confirm enhanced apoptosis within the GQD-incubated cell population, which underlines that the effects revealed by the meta analysis are weak effects.

In conclusion, further studies are necessary to understand the differential uptake into different cell types. Size and phagocytosis capability seem to be two factors. More factors could include the endocytosis rate of the cell as well as the interaction of GQDs with the glycocalyx of the cells, which might trigger the incorporation of the GQDs. A possible experiment could study the correlation between the expression of extracellular sugars like sialic acid, hyaluronic acid and fucose and the uptake of GQDs.

At a first glance, the pronounced and differential uptake into some tumor cells as well as the uptake into the depth of tumor tissue combined with very low effects on cellular function and cell viability seems to be promising for the usage of GQDs as core of a drug delivery system. However, the incorporation of the GQDs into the endolysosomal system might explain the low toxicity, as the encapsulation in lysosomes possibly protects the cell from potentially toxic effects of the GQDs. In many cases the application as a drug delivery system will require targeting of the nucleus or the cytoplasm. Therefore, endosomal escape would be desirable, which could be achieved by using the proton sponge effect. This may indeed lead to more pronounced effects on the cellular functions.

# Bibliography

- [1] S. Fasbender, S. Allani, C. Wimmenauer, R. Cadeddu, K. Raba, J. Fischer, B. Bulat, M. Luysberg, C. Seidel, T. Heinzl, and R. Haas, *RSC Adv.* **7**, 12208 (2017).
- [2] D. Kersting, S. Fasbender, R. Pilch, J. Kurth, A. Franken, M. Ludescher, J. Naskou, A. Hallenberger, C. von Gall, C. J. Mohr, et al., *Nanotechnology* **30**, 395101 (2019).
- [3] S. Fasbender, L. Zimmermann, R.-P. Cadeddu, M. Luysberg, B. Moll, C. Janiak, T. Heinzl, and R. Haas, *Scientific Reports* **9**, 1 (2019).
- [4] T. Benn, B. Cavanagh, K. Hristovski, J. D. Posner, and P. Westerhoff, *J Environ Qual.* **39**, 1875 (2010).
- [5] E. Fröhlich and E. Roblegg, *Toxicology* **291**, 10 (2012).
- [6] A. Weir, P. Westerhoff, L. Fabricius, K. Hristovski, and N. von Goetz, *Environ. Sci. Technol.* **46**, 2242 (2012).
- [7] J. Lancet, G. L. Uy, J. Cortes, L. F. Newell, T. L. Lin, E. Ritchie, R. Stuart, S. Strickland, D. Hogge, S. R. Solomon, et al., *Biology of Blood and Marrow Transplantation* **23**, S38 (2017).
- [8] K. S. Novoselov, A. K. Geim, S. V. Morozov, D. Jiang, Y. Zhang, S. V. Dubonos, I. V. Grigorieva, and A. A. Firsov, *Science* **306**, 666 (2004).
- [9] A. Hirsch, *Angewandte Chemie International Edition* **54**, 9132 (2015).
- [10] M. Segal, *Nature* **483**, 43 (2012).
- [11] M. Park, E. Bleeker, W. Brand, F. Cassee, M. van Elk, I. Gosens, W. de Jong, J. Meesters, W. Peijnenburg, J. Quik, R. Vandebruel, and A. Sips, *ACS Nano* **11**, 9574 (2017).

- 
- [12] T. J. Booth, P. Blake, R. R. Nair, D. Jiang, E. W. Hill, U. Bangert, A. Bleloch, M. Gass, K. S. Novoselov, M. I. Katsnelson, and A. K. Geim, *Nano Letters* **8**, 2442 (2008), PMID: 18593201.
- [13] Z. Dong, C. Jiang, H. Cheng, Y. Zhao, G. Shi, L. Jiang, and L. Qu, *Advanced Materials* **24**, 1856 (2012).
- [14] Y. Zhu, S. Murali, W. Cai, X. Li, J. W. Suk, J. R. Potts, and R. S. Ruoff, *Advanced Materials* **22**, 3906 (2010).
- [15] K. Bolotin, K. Sikes, Z. Jiang, M. Klima, G. Fudenberg, J. Hone, P. Kim, and H. Stormer, *Solid State Communications* **146**, 351 (2008).
- [16] S. V. Morozov, K. S. Novoselov, M. I. Katsnelson, F. Schedin, D. C. Elias, J. A. Jaszczak, and A. K. Geim, *Phys. Rev. Lett.* **100**, 016602 (2008).
- [17] W. Chen, G. Lv, W. Hu, D. Li, S. Chen, and Z. Dai, *Nanotechnology Reviews* **7**, 157 (2018).
- [18] S. Zhu, Y. Song, J. Wang, H. Wan, Y. Zhang, Y. Ning, and B. Yang, *Nano Today* **13**, 10 (2017).
- [19] X. T. Zheng, A. Ananthanarayanan, K. Q. Luo, and P. Chen, *Small* **11**, 1620 (2015).
- [20] F. Yuan, T. Yuan, L. Sui, Z. Wang, Z. Xi, Y. Li, X. Li, L. Fan, Z. Tan, A. Chen, M. Jin, and S. Yang, *Nature Communications* **9**, 2249 (2018).
- [21] S. H. Lee, D. Y. Kim, J. Lee, S. B. Lee, H. Han, Y. Y. Kim, S. C. Mun, S. H. Im, T.-H. Kim, and O. O. Park, *Nano letters* **19**, 5437 (2019).
- [22] S. Kim, S. W. Hwang, M.-K. Kim, D. Y. Shin, D. H. Shin, C. O. Kim, S. B. Yang, J. H. Park, E. Hwang, S.-H. Choi, et al., *ACS nano* **6**, 8203 (2012).
- [23] J. Shen, Y. Zhu, X. Yang, and C. Li, *Chem. Commun.* **48**, 3686 (2012).
- [24] X. Sui, C. Luo, C. Wang, F. Zhang, J. Zhang, and S. Guo, *Nanomedicine: Nanotech., Biol. and Med.* **12**, 1997 (2016).
- [25] X. Gong, Q. Zhang, Y. Gao, S. Shuang, M. M. F. Choi, and C. Dong, *ACS Appl. Mater. Interfaces* **8**, 11288 (2016).

- [26] I. Al-Ogaidi, H. Gou, Z. Aguilar, S. Guo, A. Melconian, A. Al-Kazaz, F. Meng, and N. Wu, *Chem. Commun.* **50**, 1344 (2014).
- [27] Z. L. Wu, M. X. Gao, T. T. Wang, X. Y. Wan, L. L. Zheng, and C. Z. Huang, *Nanoscale* **6**, 3868 (2014).
- [28] Q. Liu, B. Guo, Z. Rao, B. Zhang, and J. R. Gong, *Nano letters* **13**, 2436 (2013).
- [29] M. Zhang, L. Bai, W. Shang, W. Xie, H. Ma, Y. Fu, D. Fang, H. Sun, L. Fan, M. Han, C. Liub, and S. Yang, *J. Mat. Chem.* **22**, 7461 (2012).
- [30] L. Cao, X. Wang, M. J. Meziani, F. Lu, H. Wang, P. G. Luo, Y. Lin, B. A. Harruff, L. M. Veca, D. Murray, S. Xie, and Y. Sun, *J. Am. Chem. Soc.* **129**, 11318 (2007).
- [31] C. Liu, P. Zhang, F. Tian, W. Li, F. Li, and W. Liu, *J. Mater. Chem.* **21**, 13163 (2011).
- [32] S. Zhu, J. Zhang, C. Qiao, S. Tang, Y. Li, W. Yuan, B. Li, L. Tian, F. Liu, H. Gao, H. Wei, H. Zhang, H. Sun, and B. Yang, *Chem. Comm.* **47**, 6858 (2011).
- [33] W. Shang, X. Zhang, M. Zhang, Z. Fang, Y. Sun, M. Han, and L. Fan, *Nanoscale* **6**, 5799 (2014).
- [34] Z. Wang, R. Zhou, D. Jiang, J. E. Song, Q. Xu, J. Si, Y. P. Chen, X. Zhou, L. Gan, J. Z. Li, H. Zhang, and B. Liu, *Biomed. Environ. Sci.* **28**, 341 (2015).
- [35] X. Wang, R. Podila, J. Shannahan, A. Rao, and J. Brown, *Int J Nanomedicine* **8**, 1733 (2013).
- [36] D. Wang, L. Zhu, J. Chen, and L. Dai, *Nanoscale* **7**, 9894 (2015).
- [37] X. Guo and N. Mei, *Journal of Food and Drug Analysis* **22**, 105 (2014).
- [38] N. D. Mermin and H. Wagner, *Physical Review Letters* **17**, 1133 (1966).
- [39] D. R. Cooper, B. D Anjou, N. Ghattamaneni, B. Harack, M. Hilke, A. Horth, N. Majlis, M. Massicotte, L. Vandsburger, E. Whiteway, et al., *ISRN Condensed Matter Physics* **2012** (2012).

- 
- [40] P. R. Wallace, Phys. Rev. **71**, 622 (1947).
- [41] J. Kotakoski, C. Brand, Y. Lilach, O. Cheshnovsky, C. Mangler, M. Arndt, and J. C. Meyer, Nano Letters **15**, 5944 (2015).
- [42] A. F. Young and P. Kim, Nature Physics **5**, 222 (2009).
- [43] A. C. Neto, F. Guinea, N. M. Peres, K. S. Novoselov, and A. K. Geim, Reviews of modern physics **81**, 109 (2009).
- [44] S. Schnez, K. Ensslin, M. Sigrist, and T. Ihn, Physical Review B **78**, 195427 (2008).
- [45] S. Tamandani, G. Darvish, and R. Faez, Applied Physics A **122**, 37 (2016).
- [46] Z. Zhang, K. Chang, and F. Peeters, Physical review B **77**, 235411 (2008).
- [47] M. Zarenia, A. Chaves, G. Farias, and F. Peeters, Physical Review B **84**, 245403 (2011).
- [48] J. Feng, H. Dong, L. Yu, and L. Dong, Journal of Materials Chemistry C **5**, 5984 (2017).
- [49] G. Eda, Y.-Y. Lin, C. Mattevi, H. Yamaguchi, H.-A. Chen, I.-S. Chen, C.-W. Chen, and M. Chhowalla, Advanced materials **22**, 505 (2010).
- [50] C. Wimmenauer, J. Scheller, S. Fasbender, and T. Heinzel, Superlattices and Microstructures , 106171 (2019).
- [51] K. A. Ritter and J. W. Lyding, Nature materials **8**, 235 (2009).
- [52] T. Zhang, S. Wu, R. Yang, and G. Zhang, Frontiers of Physics **12**, 127206 (2017).
- [53] Y. Li, H. Shu, X. Niu, and J. Wang, The Journal of Physical Chemistry C **119**, 24950 (2015).
- [54] S. H. Jin, D. H. Kim, G. H. Jun, S. H. Hong, and S. Jeon, ACS Nano **7**, 1239 (2013).
- [55] S. Zhu, Y. Song, X. Zhao, J. Shao, J. Zhang, and B. Yang, Nano research **8**, 355 (2015).

- [56] D. Qu, M. Zheng, J. Li, Z. Xie, and Z. Sun, *Light: Science and Appl.* **4**, e364 (2015).
- [57] S. K. Cushing, M. Li, F. Huang, and N. Wu, *ACS nano* **8**, 1002 (2013).
- [58] G. Liu, K. Zhang, K. Ma, A. Care, M. R. Hutchinson, and E. M. Goldys, *Nanoscale* **9**, 4934 (2017).
- [59] H.-M. Meng, D. Zhao, N. Li, and J. Chang, *Analyst* **143**, 4967 (2018).
- [60] A. Al-Nahain, S. Y. Lee, I. In, K. D. Lee, and S. Y. Park, *International journal of pharmaceutics* **450**, 208 (2013).
- [61] Y. Kato, S. Ozawa, C. Miyamoto, Y. Maehata, A. Suzuki, T. Maeda, and Y. Baba, *Cancer cell international* **13**, 89 (2013).
- [62] Abdullah-Al-Nahain, J.-E. Lee, I. In, H. Lee, K. D. Lee, J. H. Jeong, and S. Y. Park, *Molecular Pharmaceutics* **10**, 3736 (2013), PMID: 24007260.
- [63] D. Iannazzo, A. Pistone, M. Salamò, S. Galvagno, R. Romeo, S. V. Giofrè, C. Branca, G. Visalli, and A. Di Pietro, *International journal of pharmaceutics* **518**, 185 (2017).
- [64] R. Weissleder, *Nature Biotechnology* **19**, 316 (2001).
- [65] J. Qian, D. Wang, F.-H. Cai, W. Xi, L. Peng, Z.-F. Zhu, H. He, M.-L. Hu, and S. He, *Angewandte Chemie International Edition* **51**, 10570 (2012).
- [66] K. Kaushansky, *New England Journal of Medicine* **354**, 2034 (2006).
- [67] M. Michl, *Basics Hämatologie*, Urban & Fischer Verlag/Elsevier GmbH, 2016.
- [68] P. R. Wheater, H. G. Burkitt, V. G. Daniels, et al., *Functional histology. A text and colour atlas.*, Churchill Livingstone, 23 Ravelston Terrace, Edinburgh, EH4 3TL., 1979.
- [69] M. J. Hickey and P. Kubes, *Nature reviews immunology* **9**, 364 (2009).
- [70] R. I. Handin, S. E. Lux, and T. P. Stossel, *Blood: principles and practice of hematology*, volume 1, Lippincott Williams & Wilkins, 2003.



- 
- [71] F. K. Swirski, M. Nahrendorf, M. Etzrodt, M. Wildgruber, V. Cortez-Retamozo, P. Panizzi, J.-L. Figueiredo, R. H. Kohler, A. Chudnovskiy, P. Waterman, et al., *Science* **325**, 612 (2009).
- [72] L. Ziegler-Heitbrock, P. Ancuta, S. Crowe, M. Dalod, V. Grau, D. N. Hart, P. J. Leenen, Y.-J. Liu, G. MacPherson, G. J. Randolph, et al., *Blood* **116**, e74 (2010).
- [73] S. H. Kaufmann, *Basiswissen Immunologie*, Springer-Verlag, 2013.
- [74] S. L. Nutt, P. D. Hodgkin, D. M. Tarlinton, and L. M. Corcoran, *Nature Reviews Immunology* **15**, 160 (2015).
- [75] E. Vivier, D. H. Raulet, A. Moretta, M. A. Caligiuri, L. Zitvogel, L. L. Lanier, W. M. Yokoyama, and S. Ugolini, *science* **331**, 44 (2011).
- [76] L. E. Sidney, M. J. Branch, S. E. Dunphy, H. S. Dua, and A. Hopkinson, *Stem cells* **32**, 1380 (2014).
- [77] V. Mikhailova, O. Ovchinnikova, M. Zainulina, D. Sokolov, and S. Selkov, *Bulletin of experimental biology and medicine* **157**, 751 (2014).
- [78] R. Scheuermann and E. Racila, *Leukemia & lymphoma* **18**, 385 (1995).
- [79] H. D. Soule, J. Vazquez, A. Long, S. Albert, and M. Brennan, *JNCI: Journal of the National Cancer Institute* **51**, 1409 (1973).
- [80] A. V. Lee, S. Oesterreich, and N. E. Davidson, *JNCI: Journal of the National Cancer Institute* **107** (2015), djv073.
- [81] Ş. Comaa, A. M. Cimpean, and M. Raica, *Anticancer research* **35**, 3147 (2015).
- [82] E. E. Sweeney, R. E. McDaniel, P. Y. Maximov, P. Fan, and V. C. Jordan, *Hormone molecular biology and clinical investigation* **9**, 143 (2012).
- [83] R. Cailleau, M. Olive, and Q. V. Cruciger, *In vitro* **14**, 911 (1978).
- [84] K. J. Chavez, S. V. Garimella, and S. Lipkowitz, *Breast disease* **32**, 35 (2010).

- [85] M. Lacroix and G. Leclercq, Breast cancer research and treatment **83**, 249 (2004).
- [86] J. Simmons, B. Hildreth III, W. Supsavhad, S. Elshafae, B. Hassan, W. Dirksen, R. E. Toribio, and T. J. Rosol, Veterinary pathology **52**, 827 (2015).
- [87] H. D. Soule, T. M. Maloney, S. R. Wolman, W. D. Peterson, R. Brenz, C. M. McGrath, J. Russo, R. J. Pauley, R. F. Jones, and S. Brooks, Cancer research **50**, 6075 (1990).
- [88] Y. Qu, B. Han, Y. Yu, W. Yao, S. Bose, B. Y. Karlan, A. E. Giuliano, and X. Cui, PloS one **10** (2015).
- [89] D. L. Holliday, M. A. Moss, S. Pollock, S. Lane, A. M. Shaaban, R. Millican-Slater, C. Nash, A. M. Hanby, and V. Speirs, Journal of clinical pathology **66**, 253 (2013).
- [90] S. E. Burdall, A. M. Hanby, M. R. Lansdown, and V. Speirs, Breast cancer research **5**, 89 (2003).
- [91] I. A. De Graaf, P. Olinga, M. H. De Jager, M. T. Merema, R. De Kanter, E. G. Van De Kerkhof, and G. M. Groothuis, Nature protocols **5**, 1540 (2010).
- [92] C. T. Guy, R. Cardiff, and W. J. Muller, Molecular and cellular biology **12**, 954 (1992).
- [93] E. Y. Lin, J. G. Jones, P. Li, L. Zhu, K. D. Whitney, W. J. Muller, and J. W. Pollard, The American journal of pathology **163**, 2113 (2003).
- [94] X. Tong, Q. Wei, X. Zhan, G. Zhang, and S. Sun, Catalysts **7**, 1 (2017).
- [95] T.-F. Yeh, C.-Y. Teng, S.-J. Chen, and H. Teng, Advanced materials **26**, 3297 (2014).
- [96] Y. Liu, B. Gao, Z. Qiao, Y. Hu, W. Zheng, L. Zhang, Y. Zhou, G. Ji, and G. Yang, Chemistry of Materials **27**, 4319 (2015).
- [97] D. Pan, J. Zhang, Z. Li, and M. Wu, Advanced materials **22**, 734 (2010).
- [98] D. B. Shinde and V. K. Pillai, Chemistry—A European Journal **18**, 12522 (2012).

- 
- [99] S. Zhuo, M. Shao, and S.-T. Lee, *ACS nano* **6**, 1059 (2012).
- [100] M. Shehab, S. Ebrahim, and M. Soliman, *Journal of Luminescence* **184**, 110 (2017).
- [101] C. Zhang, Y. Cui, L. Song, X. Liu, and Z. Hu, *Talanta* **150**, 54 (2016).
- [102] L. Segal and F. Eggerton, *Applied Spectroscopy* **15**, 148 (1961).
- [103] J. R. Lakowicz, *Principles of fluorescence spectroscopy*, Springer Science & Business Media, 2013.
- [104] K. Siegbahn and K. Edvarson, *Nuclear Physics* **1**, 137 (1956).
- [105] N. Alov, *Journal of Analytical Chemistry* **60** (2005).
- [106] A. Einstein, *Annalen der physik* **322**, 132 (1905).
- [107] K. Siegbahn, *Alpha-, beta-and gamma-ray spectroscopy*, Elsevier, 2012.
- [108] Wikipedia, the free encyclopedia, *X-ray photoelectron spectroscopy*, [https://en.wikipedia.org/wiki/X-ray\\_photoelectron\\_spectroscopy](https://en.wikipedia.org/wiki/X-ray_photoelectron_spectroscopy), n.d. Web 19.02.2020.
- [109] L. Lambert and T. Mulvey, *Advances in imaging and electron physics* **95**, 3 (1996).
- [110] Wikipedia, the free encyclopedia, *Transmission electron microscopy*, [https://en.wikipedia.org/wiki/Transmission\\_electron\\_microscopy](https://en.wikipedia.org/wiki/Transmission_electron_microscopy), n.d. Web 22.02.2020.
- [111] R. F. Egerton et al., *Physical principles of electron microscopy*, volume 56, Springer, 2005.
- [112] C. Kisielowski, B. Freitag, M. Bischoff, H. Van Lin, S. Lazar, G. Knippels, P. Tiemeijer, M. van der Stam, S. von Harrach, M. Stekelenburg, et al., *Microscopy and Microanalysis* **14**, 469 (2008).
- [113] C. B. Carter and D. B. Williams, *Transmission Electron Microscopy: A Textbook for Materials Science. Diffraction. II*, volume 1, Springer Science & Business Media, 1996.

- [114] J. Barthel, L. Houben, and K. Tillmann, *JLSRF* **1**, 57 (2015).
- [115] E. Smith and G. Dent, *Modern Raman spectroscopy: a practical approach*, John Wiley & Sons, 2019.
- [116] A. Smekal, *Naturwissenschaften* **11**, 873 (1923).
- [117] C. V. Raman and K. S. Krishnan, *Nature* **121**, 501 (1928).
- [118] P. Graves and D. Gardiner, Springer (1989).
- [119] R. Singh and F. Riess, *Current Science* **75**, 965 (1998).
- [120] A. Downes and A. Elfick, *Sensors* **10**, 1871 (2010).
- [121] W. Dittrich and W. Gohde, Flow-through chamber for photometers to measure and count particles in a dispersion medium, 1973, US Patent 3,761,187.
- [122] G. Radcliff and M. J. Jaroszeski, in *Flow Cytometry Protocols*, Springer, 1998, pp. 1–24.
- [123] M. Shuler, R. Aris, and H. Tsuchiya, *Appl. Environ. Microbiol.* **24**, 384 (1972).
- [124] A. N. Tiaden, A. Kessler, and H. Hilbi, in *Legionella*, Springer, 2013, pp. 233–249.
- [125] M. Kerker, *Cytometry: The Journal of the International Society for Analytical Cytology* **4**, 1 (1983).
- [126] S. H. Olejniczak, C. C. Stewart, K. Donohue, and M. S. Czuczman, *Immunological investigations* **35**, 93 (2006).
- [127] J. Pawley, *Handbook of biological confocal microscopy*, Springer Science & Business Media, 2010.
- [128] H. Goldmann, *Ophthalmologica* **98**, 257 (1939).
- [129] M. Minsky, *Scanning* **10**, 128 (1988).
- [130] P. Davidovits and M. D. Egger, *Nature* **223**, 831 (1969).

- [131] Y. Li, W. A. Dick, and O. H. Tuovinen, *Biology and fertility of soils* **39**, 301 (2004).
- [132] C. Luis, Y. Castaño-Guerrero, R. Soares, G. Sales, and R. Fernandes, *Methods and protocols* **2**, 29 (2019).
- [133] J. C. Stockert, R. W. Horobin, L. L. Colombo, and A. Blázquez-Castro, *Acta histochemica* **120**, 159 (2018).
- [134] M. C. Alley, D. A. Scudiero, A. Monks, M. L. Hursey, M. J. Czerwinski, D. L. Fine, B. J. Abbott, J. G. Mayo, R. H. Shoemaker, and M. R. Boyd, *Cancer research* **48**, 589 (1988).
- [135] D. A. Scudiero, R. H. Shoemaker, K. D. Paull, A. Monks, S. Tierney, T. H. Nofziger, M. J. Currens, D. Seniff, and M. R. Boyd, *Cancer research* **48**, 4827 (1988).
- [136] J. S. Reis-Filho and L. Pusztai, *The Lancet* **378**, 1812 (2011).
- [137] J. Khan, L. H. Saal, M. L. Bittner, Y. Chen, J. M. Trent, and P. S. Meltzer, *ELECTROPHORESIS: An International Journal* **20**, 223 (1999).
- [138] J. Cooper-Knock, J. Kirby, L. Ferraiuolo, P. R. Heath, M. Rattray, and P. J. Shaw, *Nature Reviews Neurology* **8**, 518 (2012).
- [139] S. Steiner and N. L. Anderson, *Toxicology letters* **112**, 467 (2000).
- [140] R. L. Stears, T. Martinsky, and M. Schena, *Nature medicine* **9**, 140 (2003).
- [141] S. A. Bustin, *Journal of molecular endocrinology* **25**, 169 (2000).

# Danksagung

Die Zeit meiner Doktorarbeit war eine tolle Zeit und viele Menschen haben dazu und zum Gelingen dieser Arbeit beigetragen.

An erster Stelle möchte ich meinem Doktorvater Prof. Dr. Thomas Heinzel ganz herzlich danken. Lieber Thomas, ich hätte wahrscheinlich nie eine Doktorarbeit angefangen, wenn du mir nicht - an einem Samstag, während ich Messungen für unser Hall-Magnetometrie-Paper gemacht habe - dieses wirklich spannende Medizinphysik-Projekt angeboten hättest. Und ich habe es zu keinem Zeitpunkt bereut. Du hast immer eine offene Tür und ein offenes Ohr um Probleme zu diskutieren und Lösungen zu finden. Danke, dass ich so viele Jahre - eigentlich durchgehend seit meiner Bachelorarbeit - mit dir zusammen forschen durfte!

Als nächstes danke ich meinem Mentor und dem Zweitgutachter dieser Arbeit, Prof. Dr. Rainer Haas. Lieber Herr Haas, es war mir immer eine große Freude mit Ihnen die medizinisch-physikalische Forschung zu diskutieren und Ihr Enthusiasmus ist begeisternd und ansteckend. Ohne Ihre Unterstützung wäre einiges in dieser Doktorarbeit nicht möglich gewesen. Danke für diese wirklich produktive und tolle Zusammenarbeit!

Dem gesamten Team aus der Klinik für Hämatologie, Onkologie und klinische Immunologie danke ich für die tolle Zusammenarbeit. Danke Patrick, dass ich von dir die Grundlagen der Zellkultur und Durchflusszytometrie lernen durfte und für viele Diskussionen und Hilfen zu unseren Experimenten. Danke, dass wir so viel bei euch im Labor arbeiten durften und immer hilfreiche Tipps bekommen haben! Patrick, Irmgard, Nicole, Saskia, Simon, Sabrina, Anke - ich war immer gern bei euch und hoffe, wir Physiker haben euren normalen Arbeitsablauf nicht so sehr gestört.

Dem gesamten Team aus der Forschungsgruppe der Frauenklinik um Prof. Dr. Tanja Fehm und Prof. Dr. Hans Neubauer danke ich ebenfalls herzlichst für die tolle Zusammenarbeit. Hans, Dieter, André, Johanna, Marina, Doro - eure Kommentare, Kritiken, und Anregungen waren immer hilfreich. Danke, dass wir bei euch im Labor arbeiten durften und für die Betreuung von Rabea und Jenny. Herzlicher Dank gebührt außerdem Prof. Dr. Claus A. M. Seidel, Dr. Ralf Kühnemuth und Bekir Bulat vom Institut für molekulare physikalische Chemie,



dafür, dass wir so viel Unterstützung bei der Fluoreszenzspektroskopie erhalten haben und die Geräte so oft nutzen durften.

Ganz herzlich bedanke ich mich weiterhin beim Team um Prof. Dr. Laura Hartmann vom Institut für makromolekulare Chemie. Laura, Sebastian, Stephen, Serap, Miriam - ohne euch hätten wir die Funktionalisierung der GQDs wohl nicht geschafft und ich glaube es sind sehr interessante Projekte (die noch nicht Teil dieser Arbeit sind) aus unseren Diskussionen entstanden. Danke außerdem, dass wir eure Mikrowelle und die Gefriertrocknung benutzen durften!

Herzlicher Dank geht an Prof. Dr. Charlotte von Gall und Angelika Hallenberger vom Institut für Anatomie II für die vielen Hilfen bei den Gewebeschnitten.

Bedanken möchte ich mich bei Dr. med. Johannes Fischer und Dr. Thorsten Trapp vom Institut für Transplantationsdiagnostik und dem gesamten Team der Apherese für die Bereitstellung der Apheresate. Ein herzliches Dankeschön geht außerdem an Katharina für die Durchführung der Durchflusszytometrie.

Dankeschön Prof. Dr. Christoph Janiak und Bastian Moll vom Institut für anorganische Chemie für die Aufnahme der Raman-Spektroskopie und die Röntgenstrukturanalyse.

Danke Dr. Martina Luysberg vom Ernst Ruska-Centrum am Forschungszentrum Jülich für die Aufnahme der TEM-Bilder und danke Dr. Astrid Besmehn und Dr. Heinrich Hartmann vom ZEA-3 am Forschungszentrum Jülich für die Röntgenphotoelektronenspektroskopie.

Danke Prof. Dr. Robert Lukowski und Corinna J. Mohr vom Institut für Pharmazie der Universität Tübingen, dass ihr uns die Gewebeschnitte bereitgestellt habt.

Danke Prof. Dr. Irene Esposito und Sandra Jaschinski vom Institut für Pathologie für die pathologische Beurteilung der Gewebeschnitte.

Danke Prof. Dr. Karl Köhrer und dem Team vom Genomics and Transcriptomics Laboratory für die Beratung zu den und die Durchführung der Microarray-Analysen.

Danke an das Team vom Center for Advanced Imaging für die Bereitstellung der konfokalen Fluoreszenzmikroskope und für die Einweisung an diesen.

Sehr wichtig ist mir der Dank an die Düsseldorf School of Oncology, ohne die diese Doktorarbeit mit den sehr produktiven Kooperationen zwischen Physik und Medizin wahrscheinlich nicht entstanden wäre. Danke für die finanzielle Unterstützung und für das DSO-Netzwerk, das sehr hilfreich für diese Doktorarbeit war. Spezieller Dank geht an Dr. Cornelia Höner, Prof. Dr. Sebastian Wesselborg

und Prof. Dr. Wolfgang A. Schulz für die Organisation und Durchführung des Ausbildungsprogramms.

Vieles in dieser Danksagung habe ich in der "wir"-Form geschrieben. In den meisten Fällen habe ich nicht alleine gearbeitet, sondern zusammen mit Studentinnen und Studenten, deren Abschlussarbeiten ich betreuen durfte. Sonja, Christian, Lisa, Sibel, David, Steffi, Cathrin, Saskia, Jenny, Rabea, Maren, Alexandra, Daniel - es war für mich eine große Freude mit so vielen tollen Studentinnen und Studenten zusammenzuarbeiten. Ohne euch und eure exzellente Mitarbeit wäre diese Doktorarbeit eine ganz andere und schlechtere gewesen. Ihr habt große Teile zu diesem Projekt beigetragen und dafür bin ich euch sehr dankbar. Ich habe viel von euch und mit euch gelernt und hoffe euch ging es genauso. Danke auch an die vielen Studenten, die ich in Praktika und Übungsgruppen betreuen durfte, es hat mir unglaublich viel Freude bereitet und ich habe viel gelernt.

Jakob, Svenja, Laurin, Beate, Christian, Karo, Mihai - danke für die wunderbare Arbeitsatmosphäre am Institut. Wilfried, Uwe, Harald, danke für die technische Unterstützung bei den Experimenten. Danke Bianka, für so viel Freundlichkeit und das Erledigen dieser vielen kleinen und großen administrativen Dinge. Danke Rita, Christian und Jakob für das Korrekturlesen dieser Arbeit. Lisa und Jakob, es war äußerst angenehm so eine lange Zeit mit euch ein Büro zu teilen. Ich denke gern daran zurück. Julie und Christian, mit euch war es genauso angenehm :-). Sonja, die Betreuung deiner Masterarbeit habe ich übernommen, als ich selbst gerade erst mit dem Projekt angefangen hatte - es war super, gemeinsam mit dir dieses Projekt aufzubauen, danke für deinen wertvollen Input. Christian, wenig später kam deine Bachelorarbeit dazu, dann die Masterarbeit und nun bist du mein Nachfolger - danke für wirklich viele wichtige Beiträge.

Zu guter Letzt danke ich meinen Eltern Angelika und Walter und meiner Freundin Rita, die mich so viele Jahre begleitet und unterstützt haben.